Nanogap MEM Resonators on SOI

THÈSE N^{O} 4484 (2009)

PRÉSENTÉE LE 31 AOÛT 2009

À LA FACULTE SCIENCES ET TECHNIQUES DE L'INGÉNIEUR
LABORATOIRE DES DISPOSITIFS NANOÉLECTRONIQUES
PROGRAMME DOCTORAL EN MICROSYSTÈMES ET MICROÉLECTRONIQUE

ÉCOLE POLYTECHNIQUE FÉDÉRALE DE LAUSANNE

POUR L'OBTENTION DU GRADE DE DOCTEUR ÈS SCIENCES

PAR

Nicoleta-Diana CIRESSAN

acceptée sur proposition du jury:

Prof. M. Gijs, président du jury
Prof. M. A. Ionescu, Dr M. Mazza, directeurs de thèse
Prof. R. Plana, rapporteur
Prof. H. Shea, rapporteur
Dr J. Van Beek, rapporteur

ÉCOLE POLYTECHNIQUE
FÉDÉRALE DE LAUSANNE

Suisse
2009

To my beloved parents

Acknowledgments

I would like to take the opportunity to express my gratitude to all the people who helped me accomplish this work, through advice, collaborations and support; without their assistance, finalizing my thesis would have been more difficult, if not impossible.

I would therefore like to express special thanks in the first place to Prof. Adrian M. Ionescu, whose guidance and encouraging support has always managed to put me back on track, even during the most difficult times when I was losing sight of the light at the end of the tunnel, and to Dr. Marco Mazza, for co-supervising my work and for teaching me how to become an independent researcher.

To the PhD committee members, the president Prof. Martin Gijs and the reviewers Ir. Joost van Beek from NXP, The Netherlands, Prof. Robert Plana from LAAS-CNRS, France and Prof. Herbert Shea from EPFL, for their expertise and useful suggestions.

My thanks go also to all the NanoTIMER European project partners for their collaboration and many interesting discussions we had during the years.

A large and probably most challenging part of my work has been carried out at EPFL's CMI cleanrooms, where I learnt the truth behind the famous quote by Jan L.A. Van de Snepscheut: "*In theory, there is no difference between theory and practice. But, in practice, there is*". This being said, I am grateful to Dr. Philippe Flückiger and all his team for the proficient technical guidance which helped me find solutions to the numerous practical problems I overcame in my cleanroom work. Special thanks to Dr. Cyrille Hibert for help and advice concerning etching issues and to Dr. Kevin Lister for offering his friendly support whenever I needed it most.

I would like as well to thank my former and current NANOLAB colleagues, especially to Daniel Grogg who continued the work on resonators, to Dr. Julien Boucart for motivating discussions on finite element modeling, to Dr. Dimitrios Tsamados for helping me with the device characterization and to Dr. Suat Ayöz for assistance on oscillator circuits. Kathy Boucart, thank you for your support and friendship. Finally, my appreciation goes to Joseph Guzzardi, Roland Jacques, and the secretaries Isabelle Buzzi, Karin Bellardinelli-Borcard and Marie Halm whose efficiency and availability made all the difference.

Dr. Veronica Savu, thank you for the assistance on stencil lithography and deposition.

Last but not least, none of this would have been possible without the support of my dear husband, Cristian, who provided me with an example of professional competence and motivation and that of my friends from EPFL who understood and shared my PhD student's joys and sorrows. Many thanks to the Romanian student community from Lausanne to whom I could always turn for a feeling of "home" and to my "virtual" friends (particularly Andreea, Luiza and Miruna).

Contents

Abstract

Version abrégée

1. Introduction, State-of-the-Art and Challenges for MEM resonators..... 1
1.1. MEMS Technology..... 2
1.1.1 What are MEMS?..... 2
1.1.2. MEMS and Electronics Integration..... 6
1.2. MEM Resonator Architectures..... 7
1.2.1. Electrostatic MEM Resonators 8
1.2.2. Piezoelectric Resonators..... 11
1.2.2.1 Piezoelectric-MEM Contour Mode Resonators..... 11
1.2.2.2 Bulk Acoustic Wave Resonators..... 12
1.2.3. Hybrid Resonators with Intrinsic Gain..... 14
1.2.3.1. Hybrid MEM - CMOS Resonators..... 14
1.2.3.2. Hybrid MEM - Piezoresistive Resonators..... 16
1.3. Open Challenges on Electrostatic MEM Resonators..... 17
1.4. Summary and Motivation of the Work..... 19
1.6. Bibliography..... 20

2. MEM Resonator Modeling, Design and Simulation..... 27
2.1. Modeling of Bulk-Mode Resonators..... 28
2.1.1. Mechanical Model in Linear Conditions..... 28
2.1.2. Small Signal Electrical Equivalent Circuit..... 30
2.1.3. Nonlinear Effects in MEM Resonators..... 31
2.1.4. Quality Factor and Loss Mechanisms in MEM Resonators..... 33
2.2. Resonator Designs..... 35
2.2.1. Longitudinal Beam Resonators..... 35
2.2.2. Fragmented-Membrane Bulk Lateral Resonators..... 36
2.3. Resonator Design Optimizations..... 38
2.3.1. Frequency Roll-Off..... 38
2.3.2. Energy Transfer to Other Vibration Modes..... 39
2.3.3. Anchor Loss Reduction..... 40
2.3.3.1. Tether Length Optimization..... 40
2.3.3.2. Tether Shape Optimization..... 42
2.4. Summary..... 43
2.5. Bibliography..... 44

3. Nanogap MEM Resonator Technology..... 47

3.1. Motional Resistance Reduction: Role of Gap Scaling and Silicon Film Thickness....48
3.2. Silicon-Based Lateral Nano-Gap Fabrication Methods....50
3.3. Lateral Spacer Technique....55
3.4. Process Flow....56
3.5. Hard Mask Formation and CMP Optimization....58
3.6. Nano-Gap Etch....59
3.6.1. Continuous vs. Bosch-like process....60
3.6.2. Notching Effect....61
3.6.3. Skirting Effect....62
3.7. Metallization, Final Release and Critical Point Drying....63
3.8. Resonator Fabrication on 6.25μm SOI....64
3.9. Summary....67
3.10. Bibliography....68

4. Characterization and Analysis....71
4.1. Measurement Setup....72
4.2. Micro-Gap vs. Nano-Gap Resonators....73
4.3. Nanogap Resonator Typical Responses in Vacuum, at Room Temperature....75
4.3.1. Longitudinal Beam Resonators....75
4.3.2. Fragmented Membrane Resonators....76
4.4. Small Signal Equivalent Circuit Extraction in Linear Conditions....78
4.4.1. Lumped Element Extraction Procedure....78
4.4.2. Extracted Fragmented Membrane Resonator Parameters....81
4.5. Ambient Pressure Influence on Fragmented Membrane BLR Performance....81
4.6. DC Bias Influence on Fragmented Membrane Resonator Performance....82
4.7. Nonlinear Effects....84
4.7.1. Simple Longitudinal Beam Resonator....84
4.7.2. Fragmented Membrane Resonator....85
4.8. Temperature Influence on Fragmented Membrane Resonator....87
4.9. Summary....91
4.10. Bibliography....93

5. MEM resonator applications....95
5.1. Oscillators....96
5.1.1. Oscillator Phase Noise....98
5.1.2. Oscillator Topologies....100
5.1.1. Pierce Oscillator Simulation using a Fragmented Membrane BLR....103
5.2. Filters....106
5.3. Mass Sensing....110
5.4. Summary....116
5.5. Bibliography....117

6. Conclusions and perspectives..... 121
6.1. Major Achievements in this Work.....122
6.2. Perspectives..... 123

APPENDIX A. Run-Card for a Typical “Thin”-Film SOI Wafer (1.5μm).....125

APPENDIX B. Run-Card for a Typical “Thick”-Film SOI Wafer (6.25μm)..... 127

APPENDIX C. Curriculum Vitae.....129

Abstract

Today's consumer electronics based on a large variety of time-keeping and frequency reference applications is based on quartz-crystal oscillators, because of their excellent performances in terms of quality factor, thermal and frequency stability. However, macroscopic size and CMOS incompatibility of quartz-crystal resonators draw a major limit on the miniaturization of wireless communication applications. For this reason, silicon microelectromechanical (MEM) resonators are considered promising candidates to replace quartz-oscillators in VLSI communication systems, due to their compactness, design flexibility and CMOS process compatibility.

This work reports on the design, fabrication and characterization of MEM bulk lateral resonators with resonance frequencies in the order of tens of MHz. The need of stable, low cost and high yield processes for fabricating devices with extremely narrow (sub 100nm) transduction gaps is a main research driver, together with the requirements of improved designs which include high quality factors and appropriate power handling.

We are investigating two major designs: (1) longitudinal beam resonators and (2) novel fragmented-membrane resonators that respond to both high quality factor (Q) and low motional resistance (R_m) requirements. We propose several design optimizations for solving some of the issues which currently affect the MEM resonator performance, like the frequency stability and Q enhancement through energy loss minimization.

An original fabrication process is presented, which enables the manufacturing of SOI-based, fully monocrystalline devices with 100nm transduction gaps and aspect ratios as high as [60:1], without the need of advanced lithography techniques. We successfully validate the fabrication process on two different SOI substrates, with silicon film thicknesses of 1.5μm and 6.25μm. This thickness range combined to the doping level corresponds to partially depleted SOI, which can be a substrate of choice for the fabrication of future integrated hybrid MEMS-CMOS integrated circuits for communication applications.

The fabricated structures are successfully characterized, demonstrating excellent resonator performance at room temperature. Q's as high as 235'000 and R_m's as low as 59kΩ have been extracted in vacuum. Atmospheric pressure frequency response measurements of the fragmented membrane resonators show Q's of 3'600. This value is among the best reported to date, opening the possibility for atmospheric pressure applications such as mass-detection for gas sensing applications with detection done without a special package, just by direct exposure of the resonator to the environment.

A novel study on temperature dependence (between 80K and 320K) of the fragmented membrane resonators is presented and discussed. Significant Q increase and R_m reduction are experimentally observed at cryogenic temperatures.

The bulk mode resonators developed and discussed in this thesis can successfully be integrated in oscillator circuits, as we demonstrate by simulating a Pierce topology based on the calibrated equivalent circuit model of a 24.48MHz fragmented membrane BLR. Our oscillator shows very good phase-noise performance of -142dBc/Hz at 1kHz offset from the carrier and the noise floor at -144dBc/Hz, which nearly meets the GSM specifications.

Keywords: MEM resonator, electrostatic MEMS, BLR, nanogap, SOI technology, high-Q, low motional resistance, MEM-based oscillator, mass detection

Version Abrégée

La plupart des circuits électroniques de type référence de temps et fréquence sont aujourd'hui basés sur des oscillateurs à quartz qui possèdent des excellents facteurs de qualité (Q) et une très bonne stabilité en fréquence. Par contre, l'incompatibilité des cristaux de quartz avec la technologie CMOS, ainsi que leur taille, sont des obstacles contre la miniaturisation, qui est une nécessité pour les applications sans fil. Ceci est donc une raison importante pour que les résonateurs micro-électro-mécaniques (MEM) soient considérés comme des candidats pour le replacement des cristaux de quartz. Les arguments en faveur de MEMS sont leur flexibilité de design, la taille réduite et la compatibilité avec la technologie CMOS.

Ce travail de thèse concerne la conception, la fabrication et la caractérisation des résonateurs MEM en silicium monocristallin en mode de volume, avec des fréquences de résonance dans l'ordre des quelques dizaines des MHz. Le besoin de procèdes de fabrication fiables et à bas prix pour obtenir des écarts (*gap*) très fins (sous 100nm) entre le résonateur et ses électrodes est une des motivations de ce travail. Un autre but est l'amélioration du facteur de qualité ainsi que l'obtention des meilleures performances en terme de puissances applicables sur le résonateur sans le forcer en mode non-linéaire.

Nous avons examiné deux catégories de designs : (1) un résonateur longitudinal et (2) un résonateur à membrane fragmentée qui répond à la fois aux besoins d'un très bon facteur de qualité (Q) et une basse résistance motionnelle (R_m). Plusieurs améliorations du design sont proposées et validées par simulation et expérimentation.

Un procédé de fabrication original est proposé et validé pour fabriquer des résonateurs micro-électro-mécaniques en silicium monocristallin à partir des plaques SOI, avec des écarts de 100nm avec un rapport entre leur profondeur et la largeur allant jusqu'à [60 : 1], sans avoir besoin des techniques de lithographie avancés. Le procédé de fabrication a été validé sur deux épaisseurs de couche de silicium, de 1.5μm et 6.26μm.

Les structures fabriquées ont été caractérisées avec succès à température ambiante et démontrent des excellents facteurs de qualité allant jusqu'à 235'000, et des valeurs de R_m de 59kΩ, mesurés en vide. Les mesures à pression atmosphérique des résonateurs à membrane fragmentée ont démontré un facteur de qualité de 3'600. Cette valeur est parmi les meilleures obtenues à cette date, permettant d'aborder des futures autres applications à pression atmosphérique comme, par exemple, la détection de masse pour des applications de capteurs de gaz, par exposition directe à l'environnement.

La dépendance en température (entre 80K et 320K) du résonateur à membrane fragmentée est aussi étudiée et discutée dans le manuscrit. Une importante augmentation du facteur de qualité ainsi qu'une réduction de la résistance motionnelle, sont observées et expliquées par une théorie adéquate à températures cryogéniques.

Les résonateurs en mode de volume proposés pourraient être intégrés dans des circuits oscillateurs pour des applications GSM. Ceci est démontré par la simulation de la topologie d'un oscillateur Pierce basée sur un résonateur à membrane fragmentée, qui fonctionne à 24.48MHz, ayant les caractéristiques de nos résonateurs fabriqués. L'oscillateur MEM présente un très bon bruit de phase, de -142dBc/Hz à 1kHz de offset de fréquence qui s'approche des performances requises par des applications GSM.

Mots-clés : résonateur MEM, résonateur électrostatique, mode de volume, technologie SOI, nanogap

Chapter 1

Introduction, State-of-the-Art and Challenges for MEM resonators

This first chapter gives a general introduction to the thesis work. After introducing the micro-electro-mechanical-systems (MEMS) concept, an overview is presented of the current MEMS technology, including a discussion on the MEMS-IC integration approaches presently used.
Then, a more in-depth presentation is given of the main MEM resonator architectures: electrostatic, piezoelectric and hybrid with intrinsic gain. In the frequency domain between 10's of KHz up to few GHz, the electrostatic MEM resonators are most interesting, due to their excellent performance, and to promised compactness, design flexibility, power saving and CMOS process compatibility.
Finally, the main open challenges to electrostatic MEM resonators are discussed, which motivate the work presented in the following chapters of this thesis. The need of stable, low cost and high yield processes for fabricating devices with extremely narrow (sub 100nm) transduction gaps is a main technology driver, together with the requirements of improved designs which can provide higher quality factors and power handling.

1.1. MEMS Technology

"*Imagine a machine so small that it is imperceptible to the human eye. Imagine working machines no bigger than a grain of pollen. Imagine thousands of these machines batch fabricated on a single piece of silicon, for just a few pennies each. Imagine a world where gravity and inertia are no longer important, but atomic forces and surface science dominate. Imagine a silicon chip with thousands of microscopic mirrors working in unison, enabling the all optical network and removing the bottlenecks from the global telecommunications infrastructure. You are now entering the microdomain, a world occupied by an explosive technology known as MEMS. A world of challenge and opportunity, where traditional engineering concepts are turned upside down, and the realm of the "possible" is totally redefined.*" [1.1]

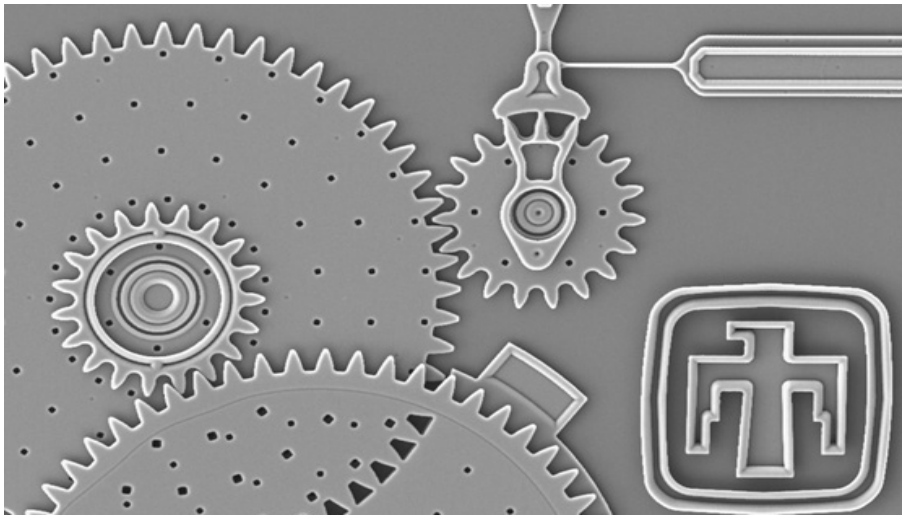

Figure 1.1. Top view of gear reduction unit from Sandia Labs [1.2]

1.1.1 What are MEMS?

MEMS acronym stands for **M**icro-**E**lectro-**M**echanical **S**ystems, micrometer-sized or smaller devices and systems which operate mainly via mechanical or electromechanical means, with applications in a large variety of domains. Key MEMS characteristics which drive the technology development include miniaturization, thus increased complexity through higher integration density, the possible co-integration with electronics, great precision mass fabrication, energy savings and higher speed due to higher operating frequencies and lower thermal constants.

The main branches of MEMS technology are:

- *Microfluidics* (Lab-on-a-chip, or micro total analysis systems - μTAS) for biological and chemical analysis [1.3], processing and sensing applications,

offer the advantages of portability, reduced amount of samples and reagents thus reduced cost, and enable parallel and combinatorial analysis.

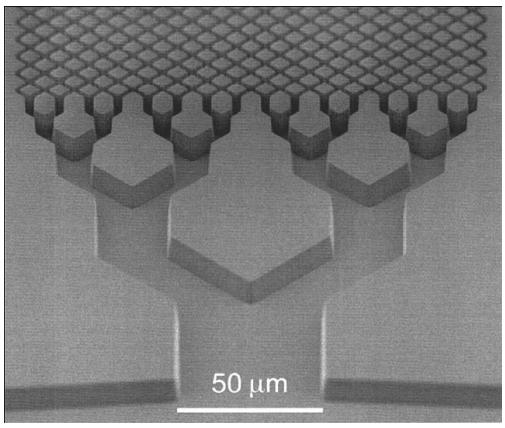

Figure 1.2. SEM of structure designed for microchip chromatography, showing channel layout at the beginning of the column. All features have been etched by RIE to a depth of 10 μm [1.3]

- *Optical MEMS* (MOEMS) incorporate components such as binary lenses, diffraction gratings, tunable optical mirrors, interferometric filters and phase modulators for applications including digital light projection, color displays, tunable filters, gas spectrum analyzers and network routers [1.4].

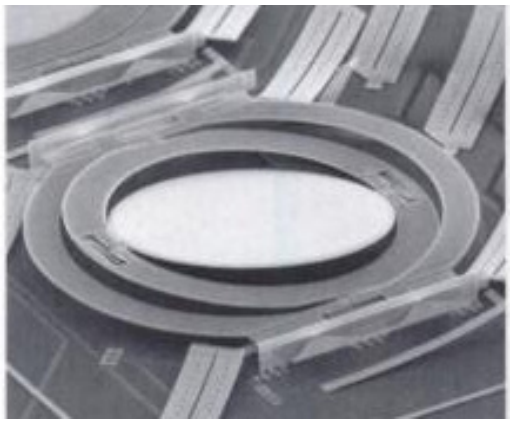

Figure 1.3. SEM of surface-micromachined two axis scanner from Lucent Technologies [1.4]

- *Radio frequency (RF) MEMS* count switches, passives (capacitors, varactors and inductors), resonators and transmission lines and antennas, which, through their performance enhancements and cost reductions, address the severe and often conflicting requirements for modern commercial and military communication, navigation, data link and avionics environments. [1.5]

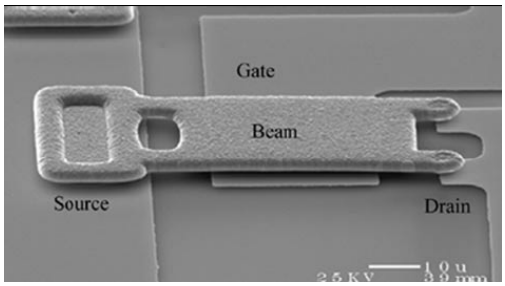

Figure 1.4. SEM micrograph of a Northeastern University MEMS switch [1.5]

- *BioMEMS* encompass the development and use of MEMS for bio-medical applications, including implants (retina, pacemakers, stents), sensors (blood pressure, analytes, pH measurement etc.), micromachined silicon immunoisolation capsules and drug delivery systems (microreservoirs and injection needles). Even though there are still some issues which need to be solved, like material biocompatibility or the bio-fouling, MEMS are extremely promising for the bio-medical domain, due to their extremely small sizes (therefore low invasiveness), the ability to control their physical and chemical properties on micrometer-scale and very precise temporal control of their operation. [1.6]

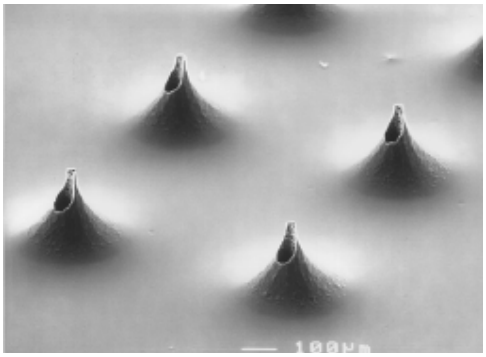

Figure 1.5. Array of pointed hollow out-of-plane silicon needles with height of 200 μm and channel diameter of 40μm [1.7]

- *Energy scavenging MEMS* like wireless sensor nodes, where the MEM devices can harvest power from the environment (RF waves, solar / ambient light, fluid flow, temperature or pressure gradient, vibrations, human power) to increase the energy efficiency of the system, and by eliminating the batteries, to enable smaller sizes, reduced maintenance and lower ecological impact [1.8].

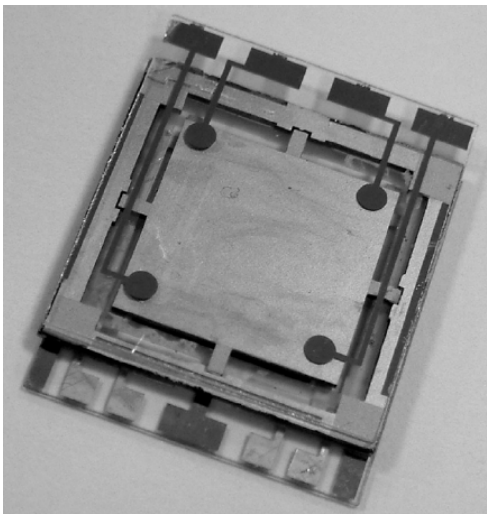

Figure 1.6. MEMS micropower electrostatic generator prototype [1.9]

Most fabrication steps of MEMS devices are derived from standard IC processing, and can be classified into (1) bulk micromachining [1.10]: high aspect ratio devices are defined by selectively etching into a substrate, usually monocrystalline silicon, using anisotropic or isotropic, wet or dry etch solutions and etch stops as shown in Figure 1.7.a and (2) surface micromachining [1.11]: structures are built from layers sequentially deposited onto a substrate, which are then patterned and selectively etched (Figure 1.7.b). To those two main methods add up wafer bonding and some more exotic methods like LIGA (X-ray lithography, electroplating, and molding) and 3D microfabrication.

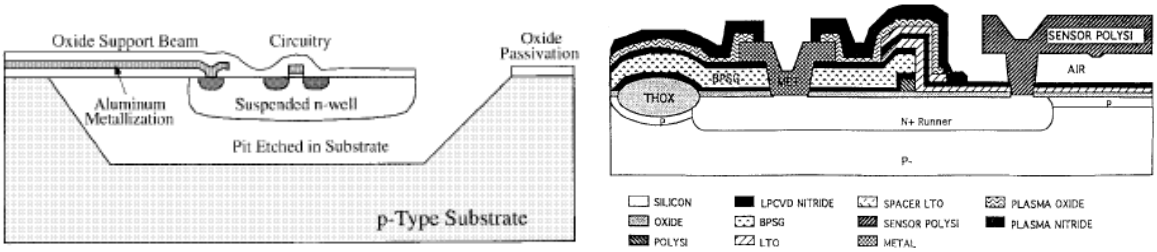

(a) (b)

Figure 1.7. (a) Cross section of a suspended silicon n-well realized using electrochemically modulated TMAH etching of a CMOS integrated circuit, illustrating the bulk micromachining process [1.10] and (b) Cross-section of the Analog Devices BiMEMS integrated MEMS technology, which exemplifies a typical surface micromachining process [1.11]

MEMS are typically silicon based, mostly due to its excellent mechanical and electrical properties and to the easy availability of mature process technologies that had been developed within the microelectronics industry. Other materials like metals (Al, Au, Cr, Cu, Pd, Pt, Ti, W, etc.), compound semiconductors (SiC, SiGe, GaAs), SiO_2, diamond, and polymers (e.g. SU8) are also used as structural materials, for applications where silicon is less suitable due to harsh environments (direct exposure to environment, high

temperatures, wide temperature swings or high shocks) or sometimes simply due to unnecessary higher cost.

1.1.2. MEMS and Electronics Integration

Currently, most MEMS-based products use hybrid “system in package” approaches, in which the MEMS devices and the electronics are fabricated separately. This modular multichip implementation needs less development time than the monolithic one, uses lower number of masks and allows independent optimization of the MEMS and the IC. Conversely, cofabricated MEMS - IC systems benefit from enhanced performance (reduced noise, crosstalk and parasitics from interconnects), smaller size (reduced chip pinout, smaller package) and potentially lower cost.

Several cofabrication approaches have been proposed and validated, as described below:

- *MEMS first* – The monocrystalline MEMS structure fabrication process is first completed, usually using bulk micromachining, prior to the CMOS and metallization stack. Typically, the MEMS are buried and sealed and the wafer surface is planarized for CMOS module. The main advantages of this approach come from the larger flexibility in choosing materials and fabrication steps (especially thermal budgets) which would otherwise damage the electronics. Examples of successfully demonstrated MEMS-first devices are pressure sensors [1.12], neural probes [1.13], accelerometers and gyroscopes [1.14-15].

- *Mixed MEMS - CMOS cofabrication* – In this approach, the CMOS process is interrupted for supplementary surface micromachining steps, usually polysilicon deposition, annealing and patterning. Since these steps are executed before the metallization, temperatures as high as 900°C can be used (usually not higher due to the risk of affecting the CMOS doping profiles). Commercial products using the CMOS MEMS approach, like pressure sensors [1.16] and accelerometers [1.17] have been demonstrated.

- *MEMS last* – Two different fabrication strategies can be set apart: (1) surface micromachined MEMS are fabricated on top of the circuitry, through deposition and patterning of layers, without touching the CMOS part and (2) microstructures are fabricated within the metal-dielectric stacks that are deposited during standard CMOS processing, by creating openings in the stack and using timed silicon wet etches to release them. The MEMS last approach drastically lowers the thermal budget, but offers great modularity, compactness and minimal parasitics, thus low power losses and better sensitivity. The first strategy results in MEMS CMOS integrated devices like

digital micromirrors [1.18] or RF MEMS resonators [1.19], while an application example using the second one are infrared detectors [1.20]

1.2. MEM Resonator Architectures

Today's consumer electronics based on a large variety of time-keeping and frequency reference applications is centered on quartz-crystal oscillators, because of their excellent performances in terms of quality factor, thermal and frequency stability. However, macroscopic size and CMOS integration incompatibility of quartz-crystal resonators draw a major limit on the miniaturization of wireless communication applications. Other drawbacks include their sensitivity to heat, shock and vibration. For these reasons, MEM resonators are considered promising candidates to replace quartz-oscillators in VLSI communication systems, which could greatly benefit from their compactness, design flexibility, power saving and CMOS process compatibility.

The earliest microresonator has been proposed by H.C. Nathanson in his experimental work dating as early as 1965 [1.21]. The original design, a resonant gate transistor (RGT), is shown in Figure 1.8, and was built at first from a metal rod (W, Au) and in later version, from metal (Al) layer [1.22], on silicon substrate.

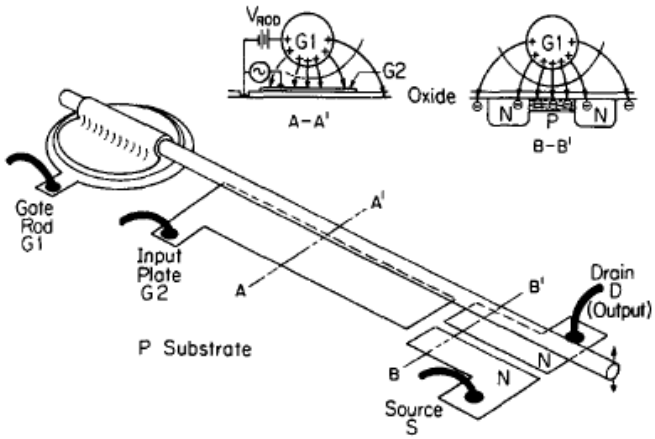

Figure 1.8. Original RGT schematic: The resonant cantilever rod G1 is insulated from the silicon substrate by 500nm SiO_2 layer and is polarized with the positive voltage V_{ROD}. Input AC voltages applied to the insulated electrode G_2 serve to attract and repel the rod, causing it to move in a direction perpendicular to the semiconductor surface (section A-A'). Motion of the free end of the rod (section B-B') is detected by field effect modulation of the conductivity of an n-type surface inversion layer between two n-type source-drain contacts [1.21]

RGTs promised great size reductions and substantial cost savings, but in reality advances were done at a very slow pace, and required vast research efforts, due to difficulties like adhesion, operational wear or related to the need of hermetic packaging.

Recent advances in microfabrication technology have finally made MEM resonators more practical, opening real perspectives for commercial applications. Today there is a great diversity of resonators, suitable for applications from medium frequency up to ultra high frequency.

This thesis focuses on electrostatic MEM resonators, functioning at MHz frequency. Initial targeted applications were reference oscillators for GSM mobile phones (26MHz) and satellite-based or earth-based satellite oscillators for satellite communication (40MHz).

Other important resonator classes are piezoelectric resonators and resonators with hybrid detection, which will also be discussed further on.

1.2.1. Electrostatic MEM Resonators

Applications in the range of 10's of kHz up to few GHz could greatly benefit from the advantages promised by electrostatic MEM resonators. This class of devices is composed of mechanically resonating parts, capacitively operated and detected. Their functioning relies on the same principles as macro-scale resonators such as guitar strings or tuning forks: when the frequency of the forcing term matches the system's natural frequency of vibration, the structures will resonate (they will absorb more energy which will cause motion with higher amplitude than at any other frequency). By scaling the resonant structure down to micrometer dimensions, the resonance frequency, which can be calculated as $\omega_{res} = 2\pi f_{res} = \sqrt{k/m}$ (where *k* is the resonator spring constant, and *m* represents its mass), is increased due to stiffness rise and mass decrease. Frequencies up to 1.5GHz have been demonstrated [1.23]. An important measure of the resonator performance is given by its quality factor, *Q*, which quantifies the ratio between the maximum stored energy and the dissipated energy per oscillation cycle. Maximization of the quality factor insures lower motional resistance, better filtering, sensitivity and improved overall efficiency of the device.

Electrostatic MEM resonators use several resonant modes:

- *Flexural mode resonators*: Beam resonators which vibrate in bending modes, the same way as guitar strings, are one main type of flexural devices. Figure 1.9 shows the schematic of an in-plane clamped-clamped (CC) flexural beam resonator. Different clamping approaches are possible and have been tested: cantilever beams [1.24], CC beams [1.25-26] and free-free beams [1.27]. Another class of flexural resonators is represented by tuning forks, which vibrate in the same mode as the macroscopic object [1.28].

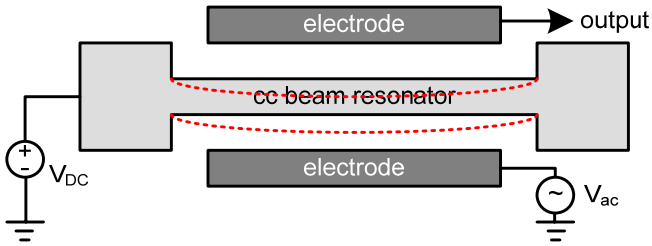

Figure 1.9. Schematic of a doubly clamped beam flexural resonator. The dotted line in red indicates the targeted mode shape for this resonator

Flexural devices have high motion amplitudes (up to a third of the actuation gap width), usually operate at frequencies in the 10kHz ÷ 100MHz domain and have quality factors limited to around 10'000. To achieve higher frequencies, very small dimensions should be used in the order of few microns or less, which have a negative impact on the device manufacturability and power handling.

- *Bulk mode resonators*: As the flexural mode devices exhibit resonance frequencies and quality factors which are not suitable for GSM and satellite communication specifications, a particular focus has been recently placed on bulk-mode MEM resonators which are much stiffer structures, and thus may be operated at higher frequencies, up to 1.5GHz [1.23]. They can also achieve much higher quality factors compared to flexural modes. In addition, the quality factor of bulk-mode resonators is less sensitive to air pressure [1.29], resulting in lower vacuum requirements for the package and hence, in a lower cost technology.

  A large variety of bulk-mode MEM resonator designs has been investigated, which offer extremely high quality factors and frequencies. Figure 1.10 shows the schematic of a square resonator resonating in a Lamé mode [1.30]. Other designs include: longitudinal beam resonators [1.31], square resonators vibrating in an extensional mode [1.32], disk [1.23] and ring bulk resonators [1.33].

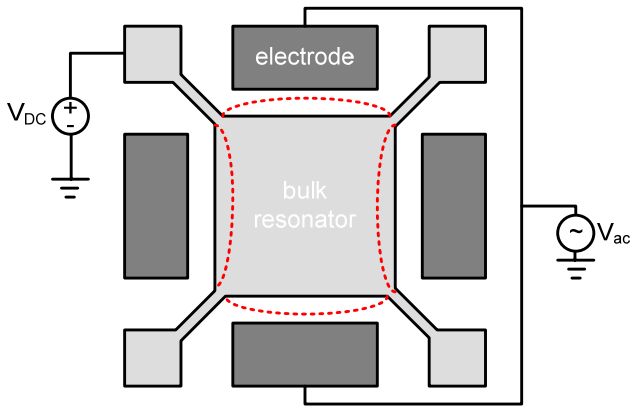

Figure 1.10. Schematic of a square Lamé-mode bulk resonator

Figure 1.11 presents a comparison of the quality factor with respect to the resonance frequency for different silicon flexural and bulk-mode resonator designs published in the literature. As already mentioned, flexural devices usually operate at frequencies below 100MHz, and have quality factors limited to 10'000, while bulk-mode resonators have been demonstrated up to 1.5GHz [1.23], and their quality factors can exceed one million [1.30].

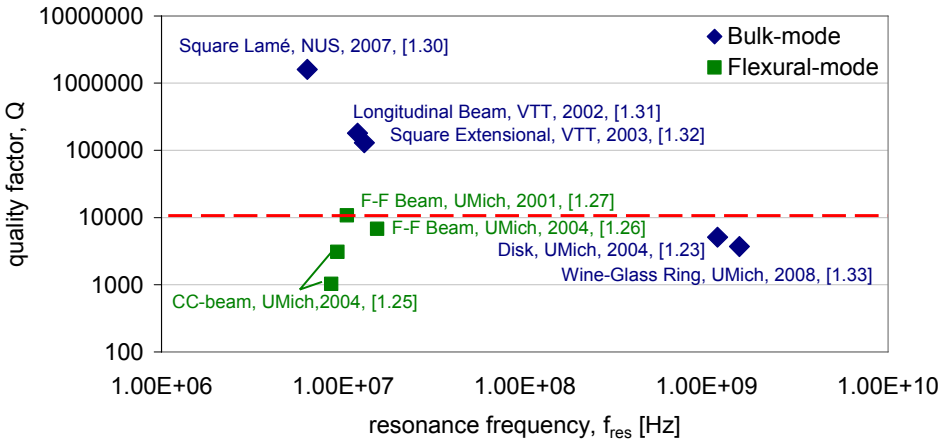

Figure 1.11. Review of quality factors vs. frequency for several flexural and bulk-mode resonators.

Thick SOI bulk MEM resonators with extremely high quality factors have been reported. However, thick SOI[1] is not a very appropriate substrate for SOI ICs where partially depleted or totally depleted MOSFETs are based on much thinner silicon layers (from 1μm down to tens of nm).

Thin-film resonators are however limited in terms of quality factor since it mirrors the stored mechanical energy, which is proportional to their (small) volume. For this reason, thin film resonator optimized design (optimization of losses) becomes a major issue in order to find a good trade-off between miniaturization, performances and partially depleted SOI CMOS technology. Another challenge of electrostatic MEM resonators is the reduction of their motional resistance in the order of tens of kΩs or less, to meet oscillator design requirements, this being translated into the technological challenge of fabricating actuation gaps of less than 100nm.

[1] The term thick SOI is employed here for silicon film thicknesses larger than 10μm

1.2.2. Piezoelectric Resonators

1.2.2.1 Piezoelectric-MEM Contour Mode Resonators

An interesting approach in decreasing the resonator motional resistances joins the MEM resonator operation principle with the piezoelectric properties exhibited by some materials such as aluminum nitride (AlN). The resulting device is called a contour-mode resonator and is composed of a suspended piezoelectric resonant structure sandwiched between two metal electrodes functioning in the same frequency range as the electrostatic MEM resonators, as shown in Figure 1.12 [1.34]. By applying an electric field on the electrodes, the structure tends to vibrate laterally, and thus it can be excited to resonate at frequencies set by its in-plane dimensions.

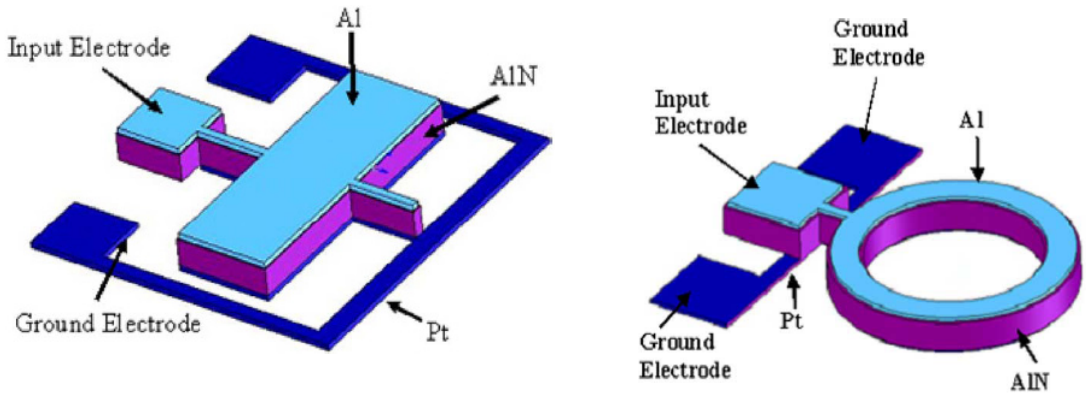

(a) (b)

Figure 1.12. Schematic representation of one-port AlN contour-mode rectangular plate resonator [1.35] and (b) Schematic view of a one-port circular ring AlN resonator to be excited in a radial-extensional contour mode shape [1.36]

Different resonator designs have been tested, like rectangular plates (Figure 1.12.a) [1.35] and rings (Figure 1.12.b) [1.36], for frequencies between 10MHz and 450MHz. For higher frequencies, up to 2.5GHz, higher-order contour modes of the rectangular geometry can be used, which employ alternating polarity electrodes to excite the desired mode [1.37]. Very low motional resistances ranging from 25Ω to 700Ω and quality factors as high as 4'300 have been demonstrated in air.

Both one port and two port configurations are possible, each having advantages and disadvantages which need to be weighed depending on the targeted application: for example, the 2-port configuration offers electrical isolation of the input and output terminals which facilitates the transduction of the resonators at higher frequencies, but is potentially subject to the excitation of spurious unwanted modes.

1.2.2.2 Bulk Acoustic Wave Resonators

For higher frequencies in the order of 1GHz up to 15GHz needed in modern wireless communication equipments, bulk acoustic wave (BAW) piezoelectric resonators exhibit very interesting performances: high quality factors compared to the LC tanks, low power consumption and great compactness, which make them very interesting options for portable applications. They also have lower frequency drift with the temperature [1.38] and better power handling [1.39] than classical surface acoustic wave (SAW) resonators, and they have lower cost, due to manufacturing processes which only use standard IC technology. BAW resonator technology uses materials and thermal budgets which are compatible with MEMS last cointegration approach [1.40], thus allowing even further performance enhancement and size reduction. Applications for BAW resonators count passive filters [1.41], voltage controlled oscillators (VCO) [1.42] and low noise amplifiers (LNA) [1.43].

BAW resonators are mainly composed of a piezoelectric film, sandwiched between metal electrodes and acoustically isolated from the substrate (Figure 1.13). Typical piezoelectric materials used for BAW resonators are aluminum nitride and zinc oxide, due to the preferred wave propagation towards the axis perpendicular to the film. Less frequently, lead zirconate titanate (PZT) may be used. Due to the piezoelectric effect, when an electric field is applied between the electrodes, the film is mechanically deformed generating bulk acoustic waves which propagate and reflect into the structure.

An energy loss mechanism which limits the resonator's quality factor results from the fact that a fraction of the generated waves are moving laterally, parallel to the electrodes and excite spurious modes. Furthermore, part of the energy dissipates into the substrate; thus, for maximum quality factor, the acoustic isolation should be made as effective as possible.

Two different approaches to BAW resonators are distinguishable:

- *Thin film bulk acoustic wave (FBAR) resonators*: This BAW resonator configuration uses a suspended metal-piezo-metal stack which is acoustically isolated from the substrate by an air gap (Figure 1.13).

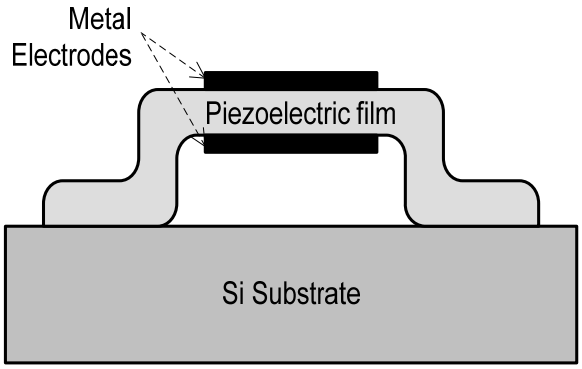

Figure 1.13. Schematic of a thin film bulk acoustic wave resonator

The freestanding membrane can be fabricated either (1) by etching a cavity into the silicon substrate which is then backfilled with a sacrificial material, on top of which the bottom electrode, the piezoelectric layer and the top electrode are deposited, patterned and finally released by etching of the sacrificial layer [1.44] or (2) by depositing and patterning a sacrificial layer with tapered edges, on top of which is formed the FBAR [1.45]. The main fabrication difficulty comes from the need of low-stress membranes, which imposes restrictions on the material choice.

- *Solidly mounted resonators (SMR)*: In a second approach, the piezoelectric film is fixed on the substrate from which it is acoustically isolated by a Bragg reflector (BR) made of quarter wavelength layers with alternating high and low acoustic impedance (typically SiO_2 and W). An SMR schematic is presented in Figure 1.14.

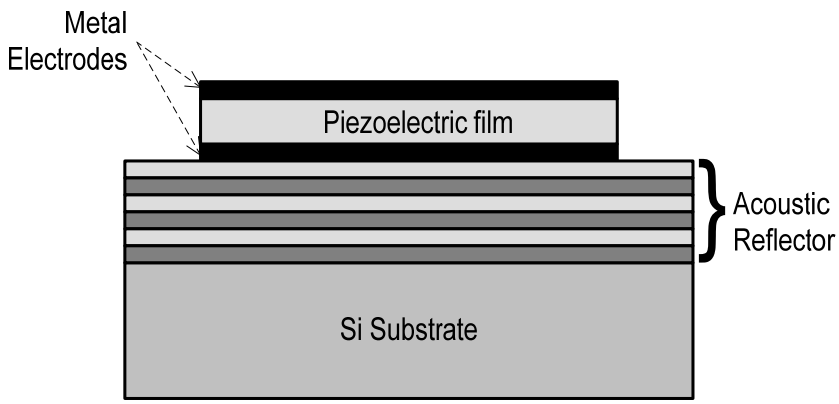

Figure 1.14. Schematic of a solidly mounted resonator

From a fabrication point of view, SMR manufacturing doesn't need to concern about the stress in the layers, but their drawback comes from the fact that in addition to the loss mechanisms which are common to FBARS, SMRs can experience losses caused by the BR material selection, the incomplete

suppression of the energy lost through the back of the BR stack, or the resistive losses from interconnects which suffer from design restrictions from parasitic coupling to the BR stack [1.46].

1.2.3. Hybrid Resonators with Intrinsic Gain

At frequencies above few tens of MHz, MEM resonators become very stiff and their size decreases to few micrometers or even to submicron scales. Consequently, the resonator displacement becomes too small for efficient capacitive detection, and new electrical detection schemes become necessary. The same applies for resonators fabricated on thin films and to nanowire resonators, which have very small coupling due to the small resonator-to-electrode overlap. Two very interesting approaches to this problem are represented by (1) hybrid MEM – CMOS resonators, composed by movable parts together with the solid state device part which is involved in the detection and (2) hybrid MEM – piezoresistive resonators, composed by electrostatically actuated resonators whose motion is detected using the piezoresistive properties of silicon. By crossing the MEMS operation with CMOS or piezoresistive detection, the output signal levels are largely increased and the motional resistance of the resonator can be further reduced.

1.2.3.1. Hybrid MEM - CMOS Resonators

Two different types of hybrid MEM - CMOS resonators have been reported:

- *The resonant suspended gate field effect transistor (RSG-FET)*: Based on the same principle as the RGT [1.22], the RSG-FET is composed of a metallic suspended beam actuated by an electrode and used as mobile gate for an underlying MOSFET structure [1.47]. Thus, the vibrating gate modulates the inversion charge in the MOS channel, which is detected through the output drain current. Figure 1.15 shows the RSG-FET schematic. The mobile gate can vibrate either vertically (Figure 1.15.a), or in-plane [1.48], as shown in Figure 1.15.b.

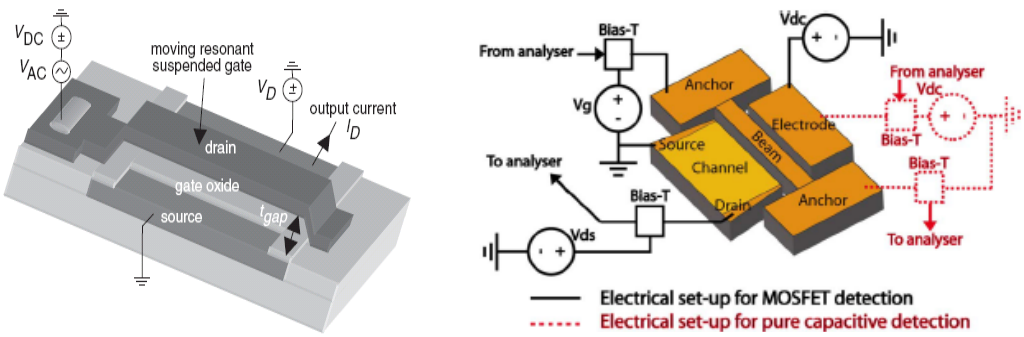

(a) (b)

Figure 1.15. Schematic of the resonant clamped-clamped beam RSG-MOSFET (a) with vertically vibrating gate [1.47] and (b) with in-plane vibrating gate [1.48]

The plot in Figure 1.16 shows an improvement in signal detection by +4.3dB compared to the capacitive detection, due to the intrinsic MOSFET gain for the in-plane device. The beam has nanometer-scale sizes of length. L=10μm, width, w=165nm, thickness, t=400nm, and actuation gap g=120nm and vibrates at 14.3MHz.

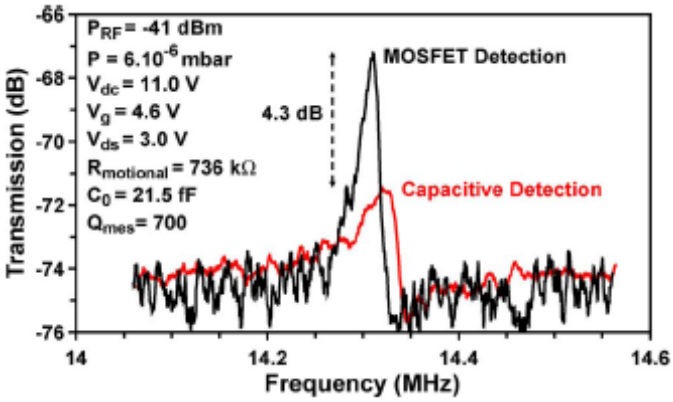

Figure 1.16. Capacitive- and MOSFET-detection comparison on the dynamic response of the in-plane RSG-FET [1.48]

- *The vibrating body field effect transistor (VB-FET)*: A second approach to MOSFET detection is represented by a moving MOSFET body with fixed gate (or multiple fixed gates). Figure 1.17 presents two possible resonator architectures: an in-plane flexural mode beam (Figure 1.17.a) and a square bulk mode resonator (Figure 1.17.b) [1.49]. Both resonators have lateral actuation nano-gap widths below 200nm, fabricated using an extension of the process developed during this thesis.

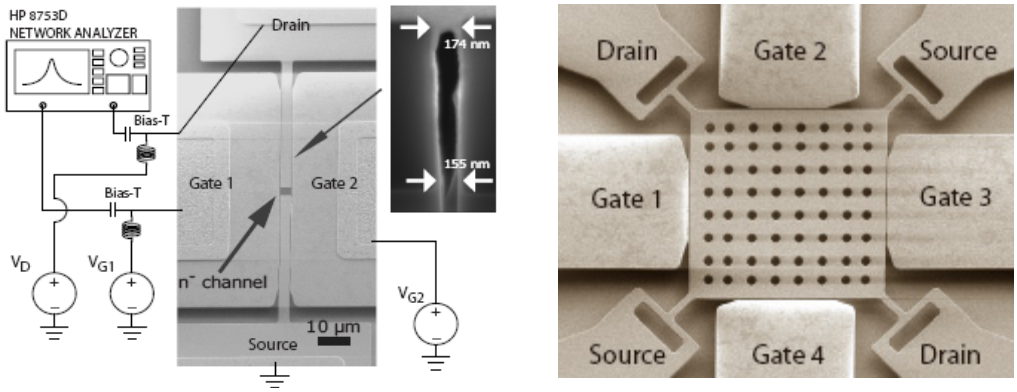

(a) (b)

Figure 1.17. (a) Measurement setup and top view SEM image of a flexural double-gate VB-FET resonator: the signal is applied on Gate 1, Gate 2 is biased with a DC voltage and the output signal is measured on the Drain. Inset: cross section of the sub-180nm gap between gate electrodes and vibrating body and (b) top view SEM image of a bulk mode VB-FET resonator with four independent lateral channels and gates [1.49]

Figure 1.18 demonstrates the VB-FET operation enhancement compared to classical 2-port capacitive detection (bottom-right). By using MOSFET detection, the output signal level is improved by more than +30dB using a single gate actuation and by almost +40dB with the double gate actuation. Very low motional resistances of 330Ω and 31Ω are achieved with VB-FET.

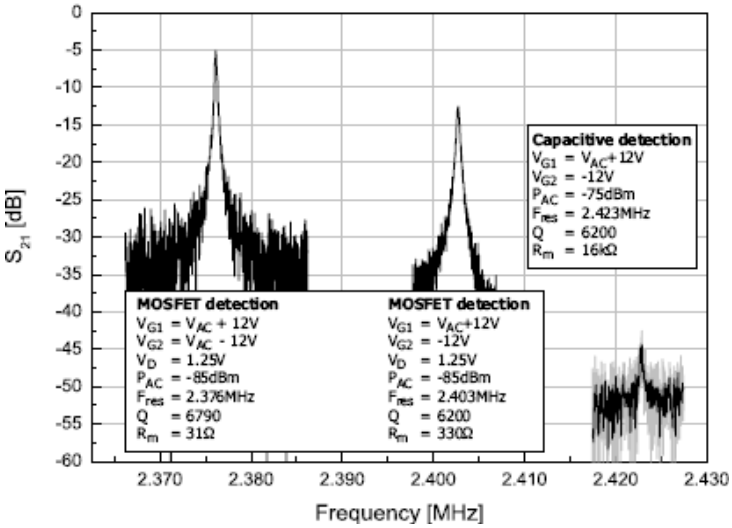

Figure 1.18. Spectra of three different measurement setups: from right to left, 2-port capacitive detection, MOSFET detection using single gate actuation and MOSFET detection using double gate [1.49]

1.2.3.2. Hybrid MEM - Piezoresistive Resonators

Similarly to the resonant gate transistors, the piezoresistive MEM resonators are capable of signal amplification, thus are efficient solutions for high frequency operation where, as the motional amplitudes decrease, classical capacitive detection become insufficient. In contrast to the transistor behavior, in this approach mechanical strains in the resonator are used to modulate the conductivity of silicon [1.50].

Figure 1.19 presents a schematic view of the hybrid MEM-piezoresistive resonator layout.

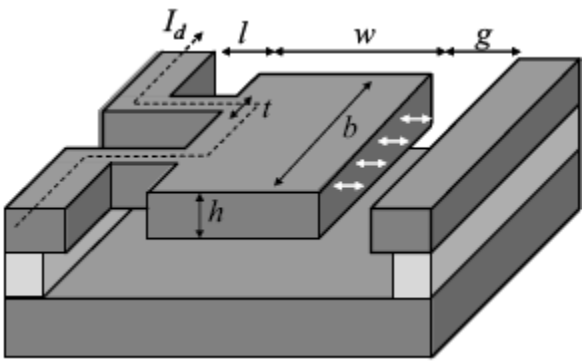

Figure 1.19. View of the MEM-piezoresistive resonator layout [1.50]

The resonator is mechanically excited by an electrostatic force using a “gate” voltage that is applied over an air gap. At resonance, the structure motion induces a mechanical strain in the arms, which is detected by measuring a change in resistivity due to piezoresistive effect.

In order to obtain signal amplification, the voltage gain at resonance should exceed unity. This can be obtained by several means:

- increasing the bias voltage and current,
- orienting the resonator arms with respect to the Si crystal lattice in such a way that the piezoresistive coefficient is maximized,
- increasing the quality factor of the structure,
- increasing the stress through resonator geometry optimization (small gaps and large width ratio between resonator and arms).

1.3. Open Challenges on Electrostatic MEM Resonators

Despite major achievements in the field of MEM resonators, there still remains a number of important challenges which need to be addressed before the technology can be considered completely established.

From the resonator technology and design point of view, stable, low cost and high yield processes for fabricating devices with extremely narrow (sub 100nm) transduction gaps are vital to achieve acceptably low impedance levels. In order to fully benefit from the performance, size and cost improvements promised by MEM resonators, IC-integration should be proven. Also, enhanced designs for better power handling capability and higher Q (through loss reduction) are necessary.

Other major challenges are related to application specifications, like the temperature stability and the packaging.

- *Temperature stability*: While quartz crystals provide excellent frequency stability with temperature (below 1 ppm/°C depending on the crystal cut), typical MEM resonators only offer temperature drifts in the order of -30 ppm/°C [1.51], due to their temperature dependent spring constant which results in a decreasing resonant frequency with increasing temperature. Current temperature compensation methods for MEM resonators are complicated, not very efficient and may adversely affect the long-term stability of the device. Among these techniques we count the electronic compensation through voltage tuning or frequency synthesis [1.52], or the passive compensation through addition to the structure of a different material with opposed thermal coefficient [1.53-55]. Thus, the subject still needs further research and implementation of novel solutions.

- *Packaging*: Currently, the MEM resonator packaging technology is a primary limitation in using the devices for commercial applications. MEM resonators are fragile structures, which need to be protected by very clean, enclosed environments from any contaminant which would degrade their short- or long-term performance. Most resonators would greatly benefit from a vacuum packaging which ensures low damping, thus high quality factors. Additionally, the package should not degrade the MEMS performance through addition of parasitic capacitances or stress-induced stiffness changes. Last but not least, the packaging should meet all those requirements while still keeping a low price. Three approaches for realizing the encapsulation are currently in use: wafer-to-wafer bonding (well established, but requires bond-pad access, low topography and high process temperatures) [1.56], die-to-wafer bonding (better in terms of temperature requirements) [1.57] and thin film embedding of the devices (most compact, versatile, more wafers can be processed in parallel, but laborious) [1.58-59]. Figure 1.20 presents the SEM cross section of a capped resonator using epitaxial silicon encapsulation layer [1.59]. In this approach, the devices are protected during capping by sacrificial SiO_2 film, which is removed in the end of the process by vapor HF through venting holes etched in the encapsulation layer. Finally, the holes are sealed in high vacuum atmosphere, by oxide deposition, ensuring a protected, low-damping environment for the resonators.

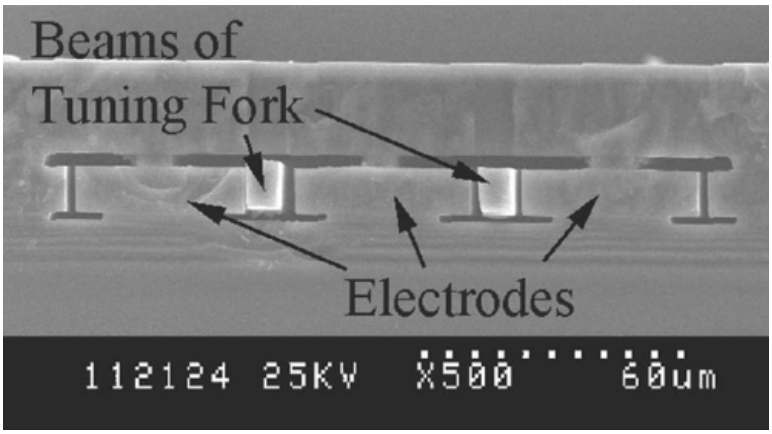

Figure 1.20. SEM cross section through MEM resonators embedded in silicon encapsulation layer. [1.59].

1.4. Summary and Motivation of the Work

In this introductory chapter, we have presented a brief MEMS technology overview including the main branches of the field with examples, and a discussion about the different IC integration approaches and challenges. A description of MEM resonator architectures was then provided, with focus on the most important categories: the electrostatic MEM resonators, the piezoelectric and the hybrid resonators with intrinsic gain. For each group, several main types of resonators have been identified and discussed. Finally, the last section discusses the main electrostatic MEM resonator open challenges still remaining to be addressed in the future, from a technology and design point of view, and application-wise.

This thesis work started in 2004, from the need of finding solutions to some of the current MEM resonator issues:

- A design was researched, which provides high quality factor operation, with low motional resistance and operating at low DC bias levels, and optimization work has been carried out

- A robust process flow was developed for fabricating resonator devices with deep submicron (~100nm) and high aspect ratio transduction gaps without the need of advanced lithography, which is scalable on thin and thick SOI layers

- Device characterization was successfully performed in order to demonstrate resonator operation, and also to investigate key issues like nonlinear behavior and performance in a wide temperature range.

1.6. Bibliography

[1.1] http://www.memx.com/

[1.2] http://mems.sandia.gov/

[1.3] E. Verpoorte and N. F. De Rooij, “Microfluidics meets MEMS”, Proceedings of the IEEE, volume 91, issue 6, 2003, pp. 930- 953

[1.4] M. C. Wu and P. R. Patterson, “Free Space Optical MEMS” in “MEMS: A Practical Guide to Design, Analysis, and Applications”, J. G. Korvink and O. Paul, Eds. Norwich, NY: William Andrew, 2005, pp. 345–402.

[1.5] J.J. Yao, "RF MEMS from a device perspective", Journal of Micromechanics and Microengineering, volume 10, 2000, pp. R9–R38

[1.6] A.C.R. Grayson, R.S. Shawgo, A.M. Johnson, N.T. Flynn, Y. Li, M.J. Cima, and R. Langer, “A BioMEMS review: MEMS technology for physiologically integrated devices”, Proceedings of the IEEE, volume 92, issue 1, 2004, pp. 6-21

[1.7] B. Stoeber and D. Liepmann, “Arrays of Hollow Out-of-Plane Microneedles for Drug Delivery”, Journal of Microelectromechanical Systems, volume 14, no. 3, June 2005, pp. 472-479

[1.8] J.A. Paradiso and T. Starner, “Energy Scavenging for Mobile and Wireless Electronics”, IEEE Pervasive Computing, volume 4, issue 1, 2005, pp. 18- 27

[1.9] B.H. Stark, P.D. Mitcheson, P. Miao, T.C. Green, E.M. Yeatman, and A.S. Holmes, “Converter Circuit Design, Semiconductor Device Selection and Analysis of Parasitics for Micropower Electrostatic Generators”, IEEE Transactions on Power Electronics, volume 21, no. 1, 2006, pp. 27-37

[1.10] G.T.A. Kovacs, N.I. Maluf, and K.E. Petersen, “Bulk Micromachining of Silicon”, Proceedings of the IEEE, volume 86, no. 8, 1998, pp. 1536-1551

[1.11] J.M. Bustillo, R.T. Howe, and R.S. Muller, "Surface micromachining for micro-electro-mechanical systems", Proceedings of the IEEE, volume 86, no. 8, 1998, pp.1552-1574

[1.12] C. S. Sander, J.W. Knutti, and J.D. Meindl, “A monolithic capacitive pressure sensor with pulse-period output”, IEEE Transactions on Electron Devices, volume ED-27, 1980, pp. 927–930

[1.13] K. Najafi, K.D. Wise, and T. Mochizuki, “A high-yield IC-compatible multichannel recording array”, IEEE Transactions on Electron Devices, volume ED-32, 1985, pp. 1206–1211

[1.14] J. Smith, S. Montague, J.J. Sniegowski, and P.J. McWorther, "Embedded micromechanical devices for the monolithic integration of MEMS with CMOS", Proceedings of the International Electron Devices Meeting (IEDM '95), 1995, pp. 609-612

[1.15] S. Lewis, S. Alie, T. Brosnihan, C. Core, T. Core, R. Howe, J. Geen, D. Hollocher, M.I Judy, J. Memishian, K. Nunan, R. Paine, S. Sherman, B. Tsang, and B. Wachtmann, “Integrated Sensor and Electronics Processing for >10A8 “IMEMS” Inertial Measurement Unit Components”, Proceedings of the International Electron Devices Meeting (IEDM ’03), 2003, pp. 949-952

[1.16] C. Hierold, “Intelligent CMOS sensors”, Proceedings of the Thirteenth IEEE International Conference on Micro Electro Mechanical Systems (MEMS ’00), 2000, pp. 1-6

[1.17] K.H.-L. Chau, S.R. Lewis, Y. Zhao, R.T. Howe, S.E Bart, and R.G. Marcheselli, “An integrated force-balanced capacitive accelerometer for low-g applications”, The 8th International Conference on Solid-state Sensors and Actuators (Transducers '95) and Eurosensors IX, 1995, volume 1, pp. 593-596

[1.18] L. J. Hornbeck, “Digital light processing and MEMS: An overview”, Proceedings IEEE/LEOS 1996 Summer Topical Meetings, 1996, pp. 7-8

[1.19] H. Takeuchi, E. Quevy, S.A. Bhave, Tsu-Jae King, and R.T. Howe, “Ge-blade damascene process for post-CMOS integration of nano-mechanical resonators”, IEEE Electron Device Letters, volume 25, 2004, pp. 529–531

[1.20] Z. Olgun, O. Akar, H. Kulah, and T. Akin, “An integrated thermopile structure with high responsivity using any standard CMOS process”, Sensors and Actuators A, volume 66, no. 1–3, 1998, pp. 218–224

[1.21] H. C. Nathanson and R. A. Wickstrom, “A Resonant-Gate Silicon Surface Transistor with High-Q band-Pass Properties”, Applied Physics Letters, volume 7, issue 4, 1965, pp. 84-86

[1.22] H. C. Nathanson, W.E. Newell, R.A. Wickstrom, and J.R.Davis Jr., “The Resonant Gate Transistor”, IEEE Transactions on Electron Devices, volume ED-14, no. 3, 1967, pp. 117-133

[1.23] J. Wang, Z. Ren, and C.T.-C. Nguyen, "1.156-GHz Self-Aligned Vibrating Micromechanical Disk Resonator", IEEE Transactions on Ultrasonics, Ferroelectrics, and Frequency Control, volume 51, no. 12, 2004, pp. 1607-1628

[1.24] Z.J. Davis, “Design, fabrication and testing of a novel MEMS resonator for mass sensing applications”, Microelectronic Engineering Journal, volume 84, 2007, pp. 1601-1605

[1.25] Y.-W. Lin, S. Lee, S.-S. Li, Y. Xie, Z. Ren, and C.T.-C. Nguyen, "Series-Resonant VHF Micromechanical Resonator Reference Oscillators", IEEE Journal of Solid-State Circuits, volume 39, no. 12, 2004, pp. 2477-2491

[1.26] S. Lee and C. T.-C. Nguyen, "Mechanically-Coupled Micromechanical Resonator Arrays for Improved Phase Noise", IEEE Ultrasonics, Ferroelectrics, and Frequency Control Joint 50th Anniversary Conference, 2004, pp. 144-150

[1.27] W.-T. Hsu, J.R. Clark, and C.T.-C. Nguyen, “Q-Optimized Lateral Free-Free Beam Micromechanical Resonators”, 11th International Conference on Solid-State Sensors & Actuators (Transducers’01), 2001, pp. 1110-1113.

[1.28] J. Yan, A.A. Seshia, K.L. Phan, P.G. Steeneken, and J.T.M. van Beek, “Narrow Bandwidth Single-Resonator MEMS Tuning Fork Filter”, IEEE International Frequency Control Symposium, 2007, pp. 1366-1369

[1.29] C.T.-C. Nguyen, “Vibrating RF MEMS for Low Power Communications”, Proceedings of MRS, volume 741, 2002, pp. J12.1.1-J2.1.12

[1.30] L. Khine, M. Palaniapan, and W.-K. Wong, "6MHz Bulk-Mode Resonator with Q Values Exceeding One Million", The 15th International Conference on Solid-State Sensors, Actuators and Microsystems (Transducers '07), 2007, pp. 2445-2448

[1.31] T. Mattila, J. Kiihamäki, T. Lamminmäki, O. Jaakkola, P. Rantakari, A. Oja, H. Seppä, H. Kattelus and I. Tittonen, "A 12MHz Micromechanical Bulk Acoustic Mode Oscillator", Sensors and Actuators A, volume 101, 2002, pp. 1-9

[1.32] V. Kaajakari, T. Mattila, A. Oja, J. Kiihamaki, H. Kattelus, M. Koskenvuori, P. Rantakari, I. Tittonen, and H. Seppa, "Square-Extensional Mode Single-Crystal Silicon Micromechanical RF-Resonator", The 11th International Conference on Solid-State Sensors, Actuators and Microsystems (Transducers '03), 2003, pp. 951-954

[1.33] Y. Xie, S.-S. Li, Y.-W. Lin, Z. Ren, and C.T.-C. Nguyen, "1.52-GHz Micromechanical Extensional Wine-Glass Mode Ring Resonators", IEEE Transactions

on Ultrasonics, Ferroelectrics, and Frequency Control, volume 55, no. 4, 2008, pp. 890-907

[1.34] G. Piazza, “One and two port piezoelectric higher order contour-mode MEMS resonators for mechanical signal processing”, Solid-State Electronics, volume 51, 2007, pp. 1596–1608

[1.35] G. Piazza, P.J. Stephanou, and A. P. Pisano, "Piezoelectric Aluminum Nitride Vibrating Contour-Mode MEMS Resonators", Journal of Microelectromechanical Systems, volume 15, 2006, pp. 1406-1418

[1.36] G. Piazza, P.J. Stephanou, J.M. Porter, M.B.J. Wijesundara, and A.P. Pisano, Low motional resistance ring-shaped contour-mode aluminum nitride piezoelectric micromechanical resonators for UHF applications", Proceedings of the 19th IEEE International Conference on Micro Electro Mechanical Systems (MEMS ‘06), 2006, pp. 20-23

[1.37] P. J. Stephanou and A. P. Pisano, "GHz Contour Extensional Mode Aluminum Nitride MEMS Resonators," IEEE Ultrasonics Symposium, 2006, pp. 2401-2404

[1.38] E. Schmidhammer, H. Heinze, M. Woelky, M. Schmiedgen, G. Henn, R. Braun, and T. Metzger, “BAW Components for PCS-CDMA Applications”, IEEE Ultrasonics Symposium 2005, volume 1, pp. 89-92

[1.39] D. Penunuri and K.M. Lakin, “RF filter design using LTCC and thin film BAW technology”, IEEE Ultrasonics Symposium 2001, volume 1, pp. 273-278

[1.40] P. Ancey, “Above IC RF MEMS and BAW filters: fact or fiction?”, Bipolar/BiCMOS Circuits and Technology Meeting, 2006, pp. 1-5

[1.41] S.H. Kim, J.-H. Kim, H.-D. Park, and G. Yoon, “AlN-Based Film Bulk Acoustic Resonator Devices With W/SiO_2 Multilayers Reflector for RF Bandpass Filter Application” Journal of Vacuum Science & Technology B, volume 19, issue 4, 2001, pp. 1164-1168

[1.42] S.S. Rai, “A 600 μW BAW-Tuned Quadrature VCO Using Source Degenerated Coupling”, IEEE Journal of Solid-State Circuits, volume 43, no. 1, 2008, pp. 300-305

[1.43] P. Guillot, “A 2GHz 65nm CMOS digitally-tuned BAW oscillator”, Proceedings of IEEE International Conference on Electronics, Circuits and Systems, ICECS 2008, pp. 722-725

[1.44] M.K. Small, “A De-Coupled Stacked Bulk Acoustic Resonator (DSBAR) Filter With 2 dB Bandwidth > 4%”, IEEE Ultrasonics Symposium, 2007, pp. 604-607

[1.45] S. Taniguchi, “An Air-Gap Type FBAR Filter Fabricated Using a Thin Sacrificed Layer on a Flat Substrate”, IEEE Ultrasonics Symposium, 2007, pp. 600-603

[1.46] R. Ruby, “Review and Comparison of Bulk Acoustic Wave FBAR, SMR Technology”, IEEE Ultrasonics Symposium, 2007, pp.1029-1040

[1.47] N. Abelé, V. Pott, K. Boucart, F. Casset, K. Segueni, P. Ancey and A.M. Ionescu, “Comparison of RSG-MOSFET and capacitive MEMS resonator detection”, IEEE Electronics Letters, volume 41, no. 5, 2005, pp. 242-244

[1.48] C. Durand, F. Casset, P. Renaux, N. Abelé, B. Legrand, D. Renaud, E. Ollier, P. Ancey, A. M. Ionescu, and L. Buchaillot, "In-plane silicon-on-nothing nanometer-scale resonant suspended gate MOSFET for In-IC integration perspectives", IEEE Electron Device Letters, volume 29, issue 5, 2009, pp. 494-496

[1.49] D. Grogg, M. Mazza, D. Tsamados, and A.M. Ionescu, “Multi-Gate Vibrating-Body Field Effect Transistor (VB-FETs)”, IEEE Electron Devices Meeting, 2008, pp. 1-4

[1.50] J.T.M. van Beek, K.L. Phan, G.J.A.M. Verheijden, G.E.J. Koops, C. van der Avoort, J. van Wingerden, D.E. Badaroglu, J.J.M. Bontemps, and R. Puers, “A piezo-resistive resonant MEMS amplifier”, IEEE Electron Devices Meeting, 2008, pp. 1-4

[1.51] M.A. Hopcroft, “Temperature Compensation of a MEMS Resonator Using Quality Factor as a Thermometer”, IEEE International Conference on Micro Electro Mechanical Systems, 2006, pp. 222 - 225

[1.52] W.-T. Hsu and A.R. Brown, “Frequency Trimming for MEMS Resonator Oscillators”, IEEE International Frequency Control Symposium, 2007, pp. 1088-1091

[1.53] R. Melamud, M. Hopcroft, C. Jha, B. Kim, S. Chandorkar, R. Candler, and T.W. Kenny, “Effects of stress on the temperature coefficient of frequency in double clamped resonators”, The 13th International Conference on Solid-State Sensors, Actuators and Microsystems (Transducers '05), volume 1, 2005, pp. 392- 395

[1.54] B. Kim, R. Melamud, M.A. Hopcroft, S.A. Chandorkar, G. Bahl, M. Messana, R.N. Candler, G. Yama, and T. Kenny, “Si-SiO2 Composite MEMS Resonators in CMOS Compatible Wafer-scale Thin-Film Encapsulation”, IEEE International Frequency Control Symposium, 2007, pp. 1214-1219

[1.55] W.-T. Hsu and C. T. C. Nguyen, “Stiffness-compensated temperature insensitive micromechanical resonators,” IEEE International Conference on Micro Electro Mechanical Systems (MEMS ’02), 2002, pp. 731–734

[1.56] J. Mitchell, G.R. Lahiji, and K. Najafi, “Encapsulation of Vacuum Sensors in a Wafer Level Package Using a Goldsilicon Eutectic”, The 13th International Conference on Solid-State Sensors, Actuators and Microsystems (Transducers '05), volume 1, 2005, pp. 928- 931

[1.57] L. Lin, “MEMS Post-Packaging by Localized Heating and Bonding”, IEEE Transactions on Advanced Packaging, volume 23, no. 4, 2000, pp. 608-616

[1.58] R. He, L. Fan, M.C. Wu, and C.-J. Kim, “Porous polysilicon shell formed by electrochemical etching for on-chip vacuum encapsulation”, Solid-State Sensor, Actuator and Microsystems Workshop, 2004, pp. 332–335

[1.59] R.N. Candler, W.-T. Park, H. Li, G. Yama, A. Partridge, M. Lutz, and T. W. Kenny, “Single Wafer Encapsulation of MEMS Devices”, IEEE Transactions on Advanced Packaging, volume 26, no. 3, 2003, pp. 227-232

Chapter 2

MEM Resonator Modeling, Design and Simulation

This chapter is divided into three main parts: a theoretical modeling part, a design part and an optimization part, mainly based on finite element simulations.
The first section presents the resonator model, the electrical equivalent circuit in linear conditions, the nonlinear behavior which degrades the resonator's performance at high vibration amplitudes, and finally a discussion about the resonator quality factor and different loss mechanisms which can affect its performance.
The design section introduces two device classes studied throughout the following chapters: longitudinal beam resonators and the novel fragmented membrane resonator designs which respond to both high quality factor and low motional resistance requirements.
The final optimization part discusses some of the issues affecting the resonator performance and proposes structure optimizations for stable resonance frequency with minimal losses due to anchoring and energy coupling to spurious vibration modes.
Following chapters will present the original fabrication process used to manufacture the proposed devices, and their successful characterization.

2.1. Modeling of Bulk-Mode Resonators

2.1.1. Mechanical Model in Linear Conditions

Figure 2.1 shows the mechanical lumped model for the MEM resonator. The equation of motion for forced oscillations of this system is:

$$m\ddot{x} + \gamma\dot{x} + kx = f = F\,sin\,\omega t \quad (2.1)$$

where *m* is the mass, γ is the damping, *k* is the linear spring constant of the resonator and *f* is the forcing term with the magnitude *F*. We also define the quality factor $Q = \sqrt{km}/\gamma$ and the resonance frequency $\omega_{res} = \sqrt{k/m}$.

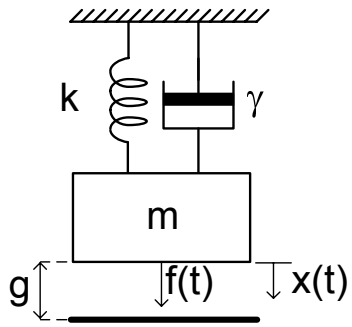

Figure 2.1. Schematic of the mass-spring-dashpot system

The solution of this equation gives the sinusoidal displacement of the resonator, caused by the forcing term [2.1, 2.2]:

$$x(t) = \frac{f/k}{1 - \frac{\omega^2}{\omega_{res}^2} + j\frac{1}{Q}\frac{\omega}{\omega_{res}}} \quad (2.2)$$

The amplitude of vibration, |*x*|, is then equal to:

$$|x| = \frac{f/m}{\sqrt{(\omega_{res}^2 - \omega^2)^2 + \frac{\omega_{res}^2\omega^2}{Q}}} \quad (2.3)$$

At resonance, ω=ω_{res}, and the amplitude becomes: $|x| = Q\frac{f}{k}$ (2.4)

The MEM resonator is actuated using an electrostatic force, f_e. The coupling is provided by capacitive transduction over a narrow gap, g, which separates the resonator from the electrode.

Knowing that:

$$f_e = \frac{\partial E}{\partial x} \quad (2.5)$$

$$E = \frac{1}{2} C v^2 \quad (2.6)$$

$$v = V_{DC} + v_{ac} = V_{DC} + V_{AC} \sin \omega t \quad (2.7)$$

where E is the energy of the system, C is the transducer working capacitance, V_{DC} is the bias voltage and v_{ac} is the alternating excitation voltage, the electrostatic force can be calculated as:

$$f_e = \frac{1}{2}\frac{\partial C}{\partial x} v^2 = \frac{1}{2}\frac{\varepsilon_0 A}{g^2} v^2 = \frac{1}{2}\frac{\varepsilon_0 A}{g^2}(V_{DC}^2 + 2V_{DC}V_{AC} \sin \omega t + V_{AC}^2 \sin^2 \omega t) \quad (2.8)$$

where ε_0 is the vacuum permittivity and A is the overlap area between the resonator and the electrode.

The first term in the bracket represents the constant component of the force, caused by the DC bias. In normal operation, the high order terms are very small, and can be neglected. The second term is the signal component of the force:

$$f = F \sin \omega t \cong \frac{\varepsilon_0 A}{g^2} V_{DC} V_{AC} \sin \omega t \quad (2.9)$$

This force excites the resonator to vibrate, creating a DC-biased, time-varying capacitor between the movable structure and the electrode, which sources an output current given by:

$$i = V_{DC} \frac{\partial C}{\partial t} = V_{DC} \frac{\partial C}{\partial x}\frac{\partial x}{\partial t} = \eta \dot{x} \quad (2.10)$$

where we identify

$$\eta = V_{DC} \frac{\partial C}{\partial x} \cong V_{DC} \frac{\varepsilon_0 A}{g^2} \quad (2.11)$$

as the electromechanical coupling coefficient which establishes the connection between the mechanical and electrical domains (velocity and current) [2.2]

2.1.2. Small Signal Electrical Equivalent Circuit

Figure 2.2 presents the equivalent series RLC circuit which can be used to model the operation of a MEM resonator. The intrinsic resonator behavior is modeled using a motional inductance L_m, a motional capacitance C_m, and a motional resistance R_m, which are physical representations of the resonator mechanical properties: effective mass (m_{eff}), stiffness (k_{eff}) and damping (γ) respectively. C_s is the feedthrough capacitance between port 1 and 2 and C_p are the capacitances coupling the pads to the substrate.

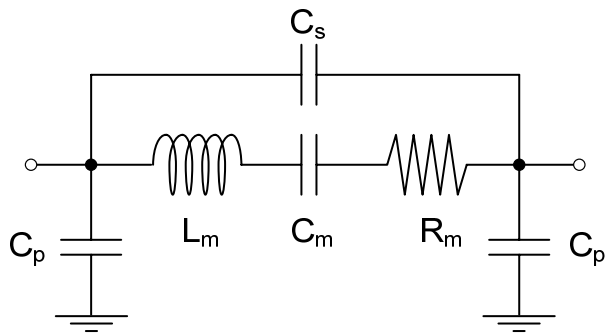

Figure 2.2. Small signal equivalent circuit

Using the electromechanical coupling coefficient (Equation 2.11), the lumped elements can be calculated as shown below, in Equations 2.12 - 2.14. [2.2]

$$L = \frac{m_{eff}}{\eta^2} \quad (2.12) \qquad C = \frac{\eta^2}{k_{eff}} \quad (2.13) \qquad R_m = \frac{\gamma}{\eta^2} = \frac{\sqrt{m_{eff} k_{eff}}}{Q} \cdot \frac{1}{\eta^2} \quad (2.14)$$

At resonance, $\omega_{res} L_m = 1/\omega_{res} C_m$, thus the equivalent inductance and capacitance cancel each other, and the resonator admittance becomes equal to:

$$Y_{res} = \frac{1}{R_m} + j\omega_{res} C_s \quad (2.15)$$

Two currents are possible: from the feedthrough capacitance and from the resonator motion, which should dominate. Consequently, in order to maximize the desired current,

R_m should be as small as possible, by building structures with small mass, stiffness, and high electromechanical coupling.

Knowing that $\omega_{res} = \sqrt{k_{eff} / m_{eff}}$, we can detail the motional resistance formula, as follows:

$$R_m = \frac{k_{eff}}{\omega_{res} Q} \cdot \frac{g^4}{V_{DC}^2 \varepsilon_0^2 w^2 h^2} \quad (2.16)$$

It becomes clear that in order to minimize R_m, while keeping reasonable DC bias levels, the most important design parameter is the gap width, *g*. The overlap between the electrode and the resonator (*w*h*) and the quality factor should also be maximized.

2.1.3. Nonlinear Effects in MEM Resonators

The linear model previously presented is only usable when small-displacement characteristics of the device are requested. However, MEMS structures can present strong nonlinearities due to large signal related phenomena, which limit the power handling of the device and hence the maximum signal-to-noise ratio which can be achieved.

Nonlinearities in electrostatically actuated MEM resonators, also called amplitude-frequency (A-f) effects, create Duffing bifurcation instabilities, and excess phase noise [2.3]. The nonlinear effects can have mechanical and capacitive origin. Even though single crystal silicon is considered to be a quasi-linear material until the fracture point, in micromechanical structures with very high Q even small material nonlinearities can become significant. Another source of mechanical nonlinearity is the geometrical deformation of the structure under large forces. The capacitive nonlinearity is inherent to the electrostatic coupling mechanism, due to inverse relationship between displacement and parallel plate capacitance [2.4].

Figure 2.3. presents a schematic view of the nonlinearity effect on the resonator response [2.5]. At the bifurcation point, x_b, the A-F curve has an infinite slope. Above bifurcation, the curve is no longer a single-valued function, but it shows a hysteretic behavior. Thus, the response becomes dependent on the frequency sweep direction: if increased, the resulting response will follow the first curve; if decreased, it will follow the second one. As indicated in the nonlinearity graphs, the greatest vibration amplitude before hysteresis, called the critical vibration amplitude, x_c, is higher than the vibration amplitude at the bifurcation point. This parameter can be used to estimate the limit for linear operation.

Depending on the type of nonlinearity, the spring can (1) soften (usually due to capacitive nonlinearity), bending the response to the left, as shown in Figure 2.3.a., or (2) it can become stiffer (typically due to mechanical effects), and the response will bend to the right, as shown in Figure 2.3.b.

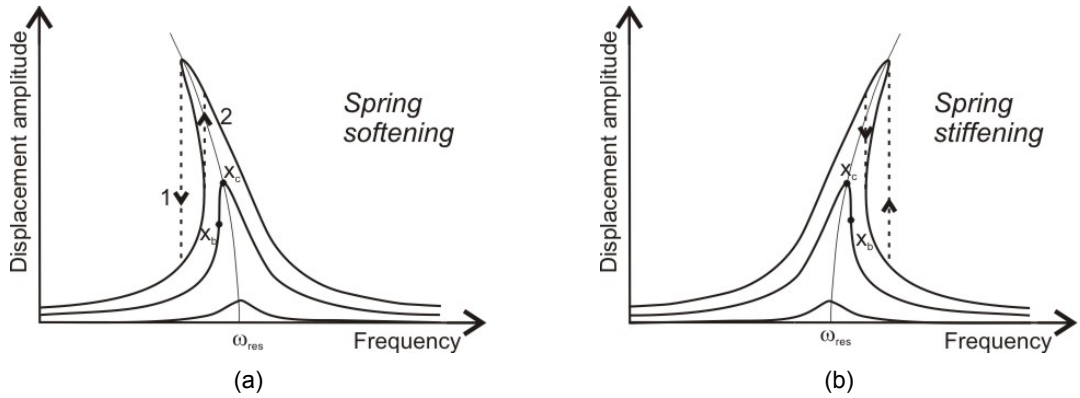

Figure 2.3. Schematic of nonlinear displacement amplitude vs. frequency around resonance. (a) The curves bend to the left in case of spring softening or (b) to the right if the spring becomes stiffer.

In order to take into account the nonlinear effects, the linear spring constant, *k*, has to be replaced in the equation of motion for forced oscillations (Equation 2.1) with the nonlinear spring, $k(x)=k_0(1+ k_1x+ k_2x^2+\ldots)$. Thus, if we take into consideration only the first three nonlinear terms, the equation of motion becomes:

$$m\ddot{x} + \gamma\dot{x} + k_0 x + k_1 x^2 + k_2 x^3 = f \quad (2.17)$$

According to [2.3], the critical drive level can be calculated as:

$$I_{critical} = \frac{2}{\sqrt{3\sqrt{3}|\kappa|Q}} \quad (2.18)$$

$$\kappa_m = -\frac{3k_3 d^4}{4m\omega_0^4 \varepsilon^2 w^2 h^2 V_{bias}^2} \quad (2.19)$$

$$\kappa_e = -\frac{3}{m\omega_0^4 \varepsilon whd} \quad (2.20)$$

where κ is the A-f coefficient due to mechanical (κ_m) or electrical (κ_e) origin.

It is interesting to note that as shown by Equation (2.18), a higher quality factor will decrease the critical level. Thus, by increasing Q, the resonator will become more prone to nonlinear effects. Also, Equation (2.19) shows that resonators with extremely narrow

gaps will be affected by mechanical nonlinearities. An optimum should be thus found between improved capacitive coupling and power handling ability of the device.

In order to increase the power handling, the A-f coefficient should be minimized, by increasing the resonator mass, frequency and transversal cross-section, *w*h* (which will also improve the capacitive coupling, due to higher electrode-to-resonator overlap).

2.1.4. Quality Factor and Loss Mechanisms in MEM Resonators

The quality factor of a resonator is a measure of the ratio between the maximum stored energy and the dissipated energy per oscillation cycle:

$$Q = 2\pi \frac{E_{stored_in_the_system}}{E_{dissipated_per_cycle}} \quad (2.21)$$

In mechanical resonators, operating in linear regime, the quality factor is defined starting from Equation (2.1). By normalizing it to the resonator mass, *m*, we obtain:

$$\ddot{x} + \frac{\gamma}{m}\dot{x} + \frac{k}{m}x = \frac{f}{m} \quad (2.22)$$

or we can rewrite it as:

$$\ddot{x} + 2\zeta\omega_{res}\dot{x} + \omega_{res}^2 x = \frac{f}{m} \quad (2.22')$$

where we define the damping factor, ζ, as:

$$\zeta = \frac{\gamma}{2m\omega_{res}} \quad (2.23)$$

When ζ=1, the system is critically-damped, and the system converges to zero fastest than in any other case, without oscillating. When ζ>1, the over-damped system will still not oscillate, but it will take longer to converge to zero.

When ζ<1, the system is under-damped, and it oscillates at a natural frequency ω_{res}. In this case, the quality factor is defined in relationship to the damping factor and the resonance peak will have higher amplitude with higher Q:

$$Q = \frac{1}{2\zeta} \quad (2.24)$$

The quality factor of a resonator is experimentally approximated from the 3dB bandwith (BW_{3dB}):

$$Q = \frac{\omega_{res}}{2\pi \cdot BW_{3dB}} \quad (2.25)$$

According to Equation (2.21), in order to increase the quality factor of a resonator which oscillates at a given frequency ω_{res}, it is possible to either (1) maximize the stored energy by increasing the mass, or (2) to reduce the energy losses.

There are several different loss mechanisms [2.6] which decrease the total quality factor of a device and that should be minimized:

- *Air Damping (Viscous Damping)* [2.7-8]: When oscillating, the resonator has to overcome the resistance of air trapped in the actuation gaps (squeeze-film damping) and those generated by friction with air for the sides parallel to the vibration displacement (slide-film damping). The energy loss caused by squeeze-film damping dominates when it exists. This source of energy loss is dominant at low and medium frequencies, and it can be avoided by packaging the resonator under vacuum.

- *Thermoelastic Damping (TED)* [2.9]: TED is a design-dependent type of loss, caused by the cyclic temperature gradient generated in the resonator's body by opposing volume changes due to vibration. The resonator will dissipate heat to return to the equilibrium state, thus loosing energy.

- *Internal Friction* [2.10]*:* This effect is generated by material imperfections like metastable defects (impurities, dangling or broken bonds), which cause energy dissipation in the form of heat. The contribution of these losses to the system depends on both the material and fabrication technology used.

- *Acoustic Anchor Losses* [2.11-12]: MEM resonators are freestanding structures, anchored to the substrate with suspension tethers or pillars. In all cases, the suspensions create paths of energy dissipation, which can be minimized by placement in the nodal points of the resonating structure, by choosing small widths, and by carefully designing their shape / dimensions for low motion of the suspensions.

- *Energy Transfer to Other Vibration Modes:* If the desired mode is in the close vicinity of other spurious modes, they can couple, generating energy loss of the

main mode. The separation between these modes can be enlarged by carefully designing the resonator.

All the abovementioned loss mechanisms add up directly for total energy loss, and the overall quality factor can be expressed as:

$$\frac{1}{Q_{total}} = \frac{1}{Q_{viscous}} + \frac{1}{Q_{acoustic}} + \frac{1}{Q_{TED}} + \frac{1}{Q_{internal}} + \frac{1}{Q_{coupling}} \quad (2.26)$$

In most cases, the thermoelastic damping and internal frictions are negligible. Also, if the resonator is operated under vacuum, the losses due to air damping are very small. Therefore, the most important phenomena affecting the quality factor are the acoustic anchor losses and the energy transfer through coupling to other vibration modes.

2.2. Resonator Designs

In this work, two main resonator designs were investigated, which will be detailed in the following sections: a longitudinal beam resonator, and a fragmented membrane resonator. Both types of devices are designed to vibrate in bulk modes. This choice was made considering the trend from Figure 1.11: due to larger sizes, bulk mode resonators are less susceptible to fabrication tolerances and thus can attain larger frequencies with better precision than flexural mode devices, and they usually have higher reported quality factors.

Simulations of the resonator designs included in this work have been performed using finite element method (FEM) software ANSYS. The main goal was to select designs, to analyze their operation and to optimize them for lower losses, thus higher quality factors. Both modal and harmonic analyses have been used to determine the natural frequencies, the mode shapes of the structures and the associated displacements.

2.2.1. Longitudinal Beam Resonators

Figure 2.4 presents one of the selected designs analyzed in this work, a longitudinal beam resonator. It is a relatively simple design, which has been previously fabricated and characterized by other groups also [2.13]. Our mail goal for investigating it was to evaluate our technology and to study a simple and well understood design, which precedes the original fragmented-membrane resonator presented further on.

This resonator vibrates in a Lamé mode, which couples longitudinal and lateral vibrations, with each two opposite sides moving in anti-phase. Due to the very low width-over-length ratio of our design, the longitudinal movement is negligible and thus the

vibration mode is also called lateral length-extensional. The resonance frequency of the fundamental mode is determined mainly by its length, according to [2.14]:

$$f_{res} = \frac{1}{2L}\sqrt{\frac{E}{\rho}} \quad (2.27)$$

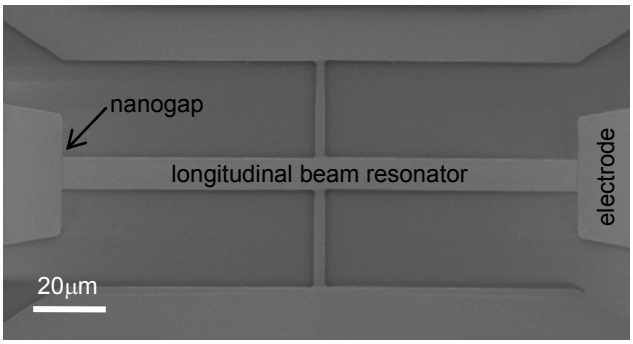

Figure 2.4. SEM image of a longitudinal beam resonator.

The main disadvantage of the longitudinal beam resonators is that due to the small overlap between the resonator and the electrode, they have high motional resistances. In order to lower R_m, an "improved" beam design which widens near its ends was also designed and tested. Figure 2.5 shows an SEM image of this device. Characterization of both resonators is presented in Chapter 4, demonstrating the motional resistance decrease of the improved design.

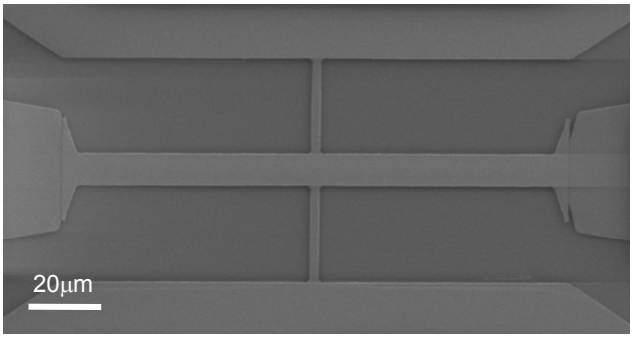

Figure 2.5. SEM image of an "improved" longitudinal beam

2.2.2. Fragmented-Membrane Bulk Lateral Resonators

Another approach for increasing the electrode-to-resonator overlap is by connecting in parallel many longitudinal beams. This design, called a fragmented-membrane BLR MEM resonator, is presented in Figure 2.6. The device is fabricated on SOI substrate and operated with capacitive detection. Two SOI wafers with silicon film thicknesses of 1.5μm and 6.25μm were used, resulting in two groups of resonators: we will classify as type-A the resonators built on 1.5μm layer and type-B the ones on 6.25μm layer. The

MEMS structure in Figure 2.6.a is a type-B resonator, with simple suspension arms, functioning in a 24.46MHz bulk mode, as shown by ANSYS finite element modeling simulations in Figure 2.6.b.

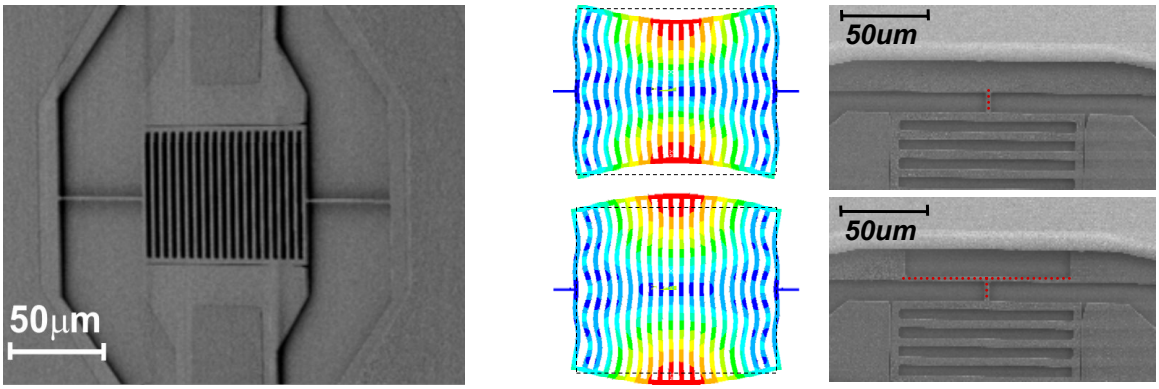

(a) (b) (c)

Figure 2.6. (a) Optical image of a fabricated type-B fragmented-membrane bulk-mode MEM resonator with 20 parallel connected beams, (b) ANSYS simulation showing the mode shapes for a 24.6MHz fragmented-membrane resonator and (c) Anchor-loss optimization: 'simple-arm' (top) vs. 'T-arm' (bottom)

The MEM resonator is composed of a rectangular membrane fragmented by parallel rectangular holes, which serve a double purpose: (1) they enable the resonator to be designed as a multi-beam structure (with all the beams connected in parallel, which increases the lateral actuation width), and (2) they allow easier sacrificial layer etching.

This design answers the task of obtaining a high frequency resonator with high quality factor. In order to further reduce the losses, design variations were investigated (e.g. different types of suspension arms for lower anchor losses). Figure 2.6.c shows the SEM images of two different arm types, a 'simple-arm' (top) and a 'T-arm' (bottom), designed for reduced anchor losses, as it will be discussed in Section 2.3.3.2.

The one dimensional model of fundamental vibration frequency presented from Equation (2.27) is corrected with the mass loading corresponding to beam parallel connections, resulting in the following expression:

$$f_{res} = \frac{1}{2\pi}\sqrt{\frac{k_{eff}}{m_{eff}}} \cong \frac{\beta}{2L}\sqrt{\frac{E}{\rho}} \quad (2.28)$$

where β=0.942 is a correction factor, which reflects the k_{eff}/m_{eff} ratio deviation from the single-beam model, due to the added mass.

Table 2.1 summarizes the design parameters of the fragmented-membrane resonators investigated in this thesis.

Table 2.1. Design Parameters of Fragmented-Membrane MEM resonators. Resonator type refers to the silicon film thickness. Type-A stands for 1.5μm SOI, and Type-B for 6.25μm SOI wafers

Resonator type	A simple-arm	B simple-arm	B T-arm
E [GPa], Si Young's modulus	125[1]	165	
ρ [kg/m^3], Si density		2330	
L_b [μm], beam length		161	
w_b [μm], beam width		5	
N_b, nb. of parallel beams		20	
L_c [μm], lateral connection length		195	
w_c [μm], lateral connection width		5	
L_{arm} [μm], arm length	20	10	30 / 70
w [μm], electrode width		183	
g [nm], gap width	250[1]	100	
h [μm], SOI thickness	1.3[1]	6.25	

2.3. Resonator Design Optimizations

Two types of optimizations were done that will be presented in the following sections:

- frequency stability and energy loss optimization with respect to the width over length ratio of the device
- suspension arm length and shape optimization to avoid energy losses to the anchors or transfer to spurious modes.

2.3.1. Frequency Roll-Off

An important parameter which needs to be considered when designing any bulk rectangular resonator is the width-over-length ratio. Even though the analytical formula for the resonance frequency (Equation 2.27) indicates that f_{res} is independent of the width, w, of the resonator, more accurate modeling shows that as w increases beyond a certain value with respect to the resonator length, the frequency starts to roll-off, probably due to the Poisson effect [2.15]. As the fragmented membrane resonator design is composed of multiple longitudinal beams connected in parallel, where each beam has a small w/L ratio, it does not suffer from frequency roll-off.

Figure 2.7. plots the Lamé-mode resonance frequency of a BLR with respect to the w/L ratio. The values were obtained from ANSYS simulations. The plot shows that the frequency is constant for w/L ratios between 0.1 and 0.8. Below this interval, we notice a very slight increase, probably due to arms-induced stiffening. Above it, the frequency decreases rapidly, as previously explained. Thus, we obtain a superior limit for the

[1] Reduced Young's modulus, gap-width and thickness as a result of unwanted silicon galvanic corrosion which will be discussed in Chapter 3.

resonator width, which sets a consequent limit for the minimum achievable motional resistance, R_m.

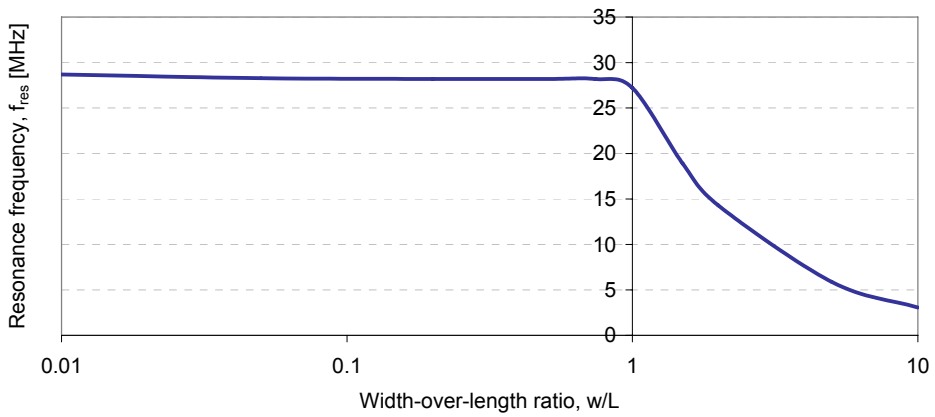

Fig. 2.7. Frequency roll-off for the Lamé-mode as a function of resonator width-over-length ratio

2.3.2. Energy Transfer to Other Vibration Modes

As already mentioned, an important design parameter for MEM resonators is the width-over-length ratio (*w/L*) of the BLR.

Figure 2.8 plots the resonance frequency versus *w/L* of the lowest order Lamé-mode and two other nearest modes (the "corner"-mode in green and the extensional-mode in red). For *w/L*'s between 0.7 and 2, the natural frequencies of the three modes are very near, and thus the energy losses to other modes are enhanced.

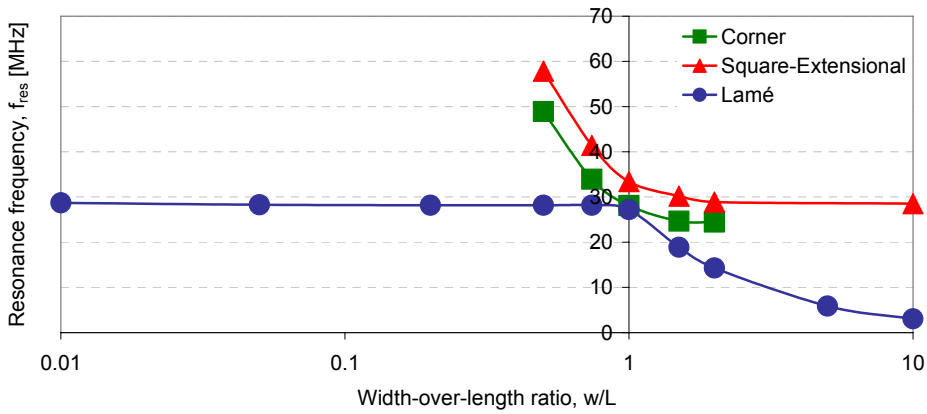

Figure 2.8. Lamé-mode, "Corner"-mode and Extensional-mode frequencies as functions of resonator *w/L*

Figure 2.9 shows the three modes studied for a square resonator (*w/L=1*): the targeted Lamé-mode (Figure 2.9.a) and the two parasitic modes from its vicinity (the "corner"-mode shown in Figure 2.9.b and the extensional mode from Figure 2.9.c).

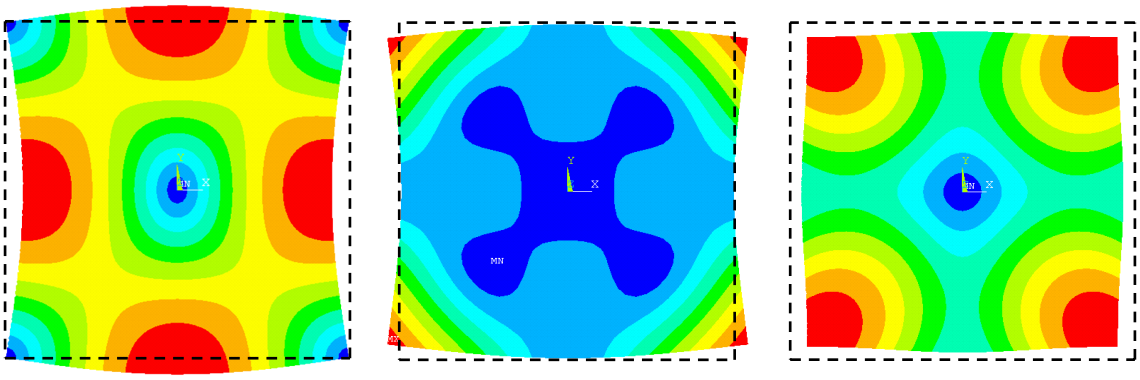

(a) (b) (c)

Figure 2.9. Three studied bulk modes for a square MEM resonator: (a) Lamé, (b) "corner" and (c) square-extensional

Given the frequency roll-off and the spurious modes close proximity at certain *w/L* ratios, we can draw the conclusion that for stable frequency and a minimum energy loss of the Lamé mode, the rectangular resonator dimensions should respect the rule: *w/L=[0.1,0.8]*.

2.3.3. Anchor Loss Reduction

Resonating structures which are anchored to a substrate lose a certain amount of mechanical energy through the suspension tethers. This energy dissipation sets a limit for the maximum attainable quality factor. Therefore, it is important to optimize both the dimensions and the location of the tethers in order to maximize Q.

The anchor losses are affected by the placement, size and shape of the suspension tethers. For an optimal result, the resonator should be suspended from its nodal points, and the tethers should be as thin as possible, in order to minimize the impact on the resonator movement. Due to practical reasons (fabrication tolerances, rigidity issues), all anchors have finite width and it is impossible to fix them at the nodal point alone. Thus, the tether shape and dimensions become significant in minimizing anchoring losses.

2.3.3.1. Tether Length Optimization

Figure 2.10 plots the simulated and the analytical resonance frequencies of a longitudinal beam resonator oscillating in Lamé-mode (blue curves) and the simulated one for the tether beam (red curve), with respect to the arm length (*AL*). We can see that the Lamé-mode has a constant frequency in all points apart from the values where the tether length approaches $\lambda/2$. At half-wavelength, the suspension resonance frequency equals the one of the Lamé mode, generating energy losses and frequency shift of the latter. This behavior is periodical, with a period of $\lambda/2$.

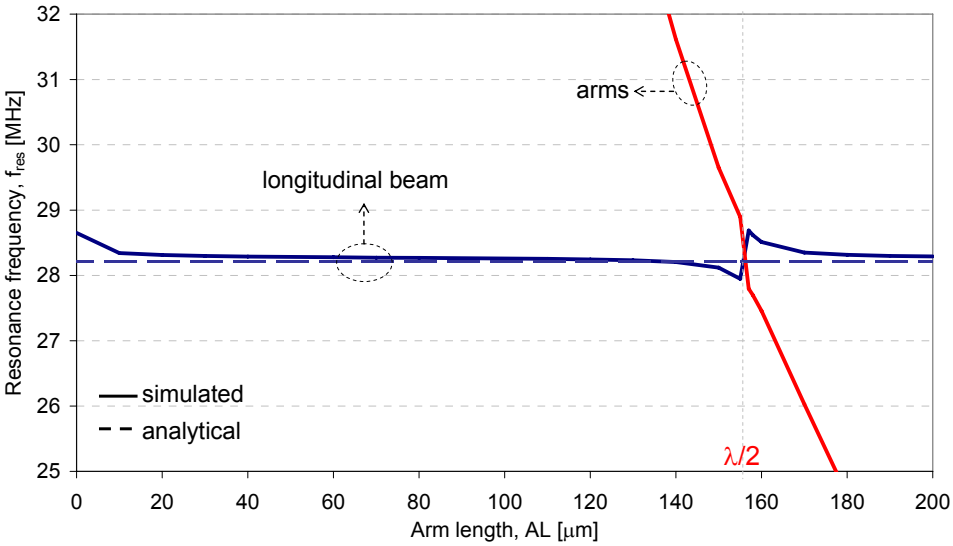

Figure 2.10. Simulated and analytical resonance frequency vs. arm length for a longitudinal-beam resonator (blue curves) and the doubly-clamped beam composed by the resonator arms (red curve)

Consequently, in order to minimize the impact of anchoring on quality factor but also on resonance frequency, *λ/4* arms have been designed.

This result is not surprising, since vibrating beams can be modeled as mechanical transmission lines and from the transmission line theory results that at half wavelength there is full energy transmission into the anchors, while at quarter wavelength we obtain maximum reflection of the energy back to the resonator.

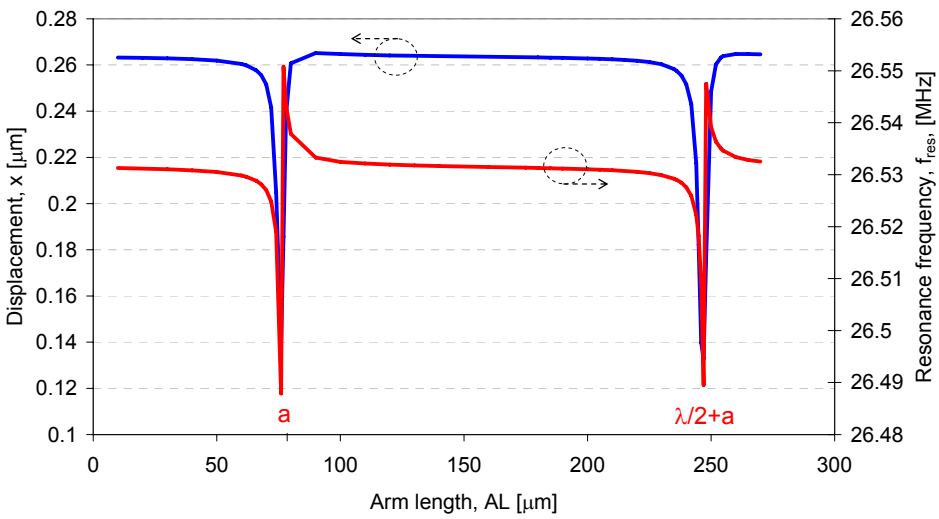

Figure 2.11. Simulated displacement (with blue) and frequency (with red) of a fragmented membrane resonator, with respect to the arm length

Similar behavior is observed for fragmented-membrane resonators, as presented in Figure 2.11. Periodically, with the same period of $\lambda/2$, the resonator displacement has a sudden drop from its constant value and at the same time, the resonance frequency shifts. The arm length value, *a*, where the first shift occurs is design dependent, influenced mostly by the spacing between the beams which compose the membrane.

2.3.3.2. Tether Shape Optimization

Another aspect which has an influence on the energy loss is the suspension shape. In addition to the simple-beam arms (Figure 2.12.a) we have also designed T-shaped arms (Figure 2.12.b). Characterization results for both device-types are presented in Chapter 4, demonstrating improved resonator performance for the T-shape arm configuration.

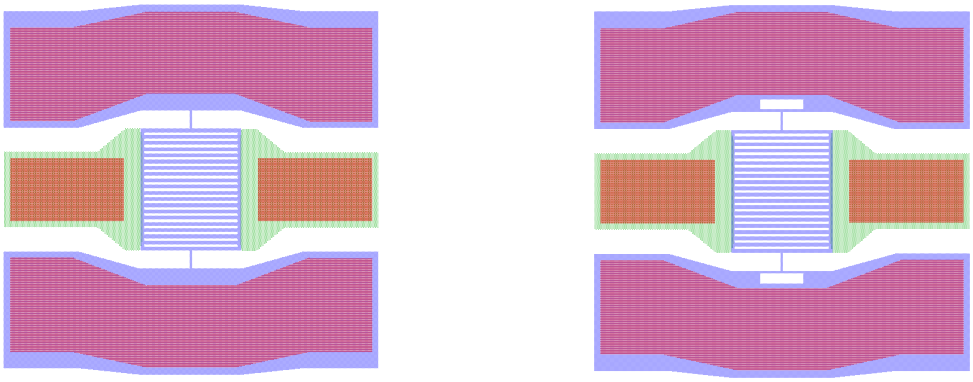

(a) (b)

Figure 2.12. Design layout of (a) simple-arm resonator and (b) T-arm resonator

2.4. Summary

In this chapter we have presented the bulk-mode MEM resonator modeling, design and finite element simulation. Bulk-mode MEM resonator modeling in linear conditions was presented starting from the equation of motion for a mass-spring-dashpot system. Then, the small signal electrical equivalent circuit, which converts the mechanical domain parameters into electrical ones, and the nonlinear resonator behavior, were explained.

The work in this thesis is focused on two resonator design classes, both vibrating in bulk modes: (1) a simple longitudinal beam resonator and an optimized beam, whose ends are widening in order to increase the resonator-to-electrode overlap and thus to decrease the motional resistance and (2) a novel fragmented-membrane bulk lateral resonator composed of parallel longitudinal beams connected together at their ends.

We have discussed the device width-over-length ratio effect on the resonant frequency and quality factor, and we have given ANSYS finite element modeling simulation-based design guidelines to avoid the Poisson effect-induced frequency roll-off and the energy losses due to energy coupling to spurious vibration modes. Moreover, a guideline for optimal anchor design has been proposed, based on transmission line theory, and confirmed by simulations, which will minimize the acoustic anchor losses, and thus improve the resonator's quality factor.

2.5. Bibliography

[2.1] H. C. Nathanson, W.E. Newell, R.A. Wickstrom, and J.R. Davis Jr., “The Resonant Gate Transistor”, IEEE Transactions on Electron Devices, volume ED-14, no. 3, 1967, pp. 117-133

[2.2] V. Kaajakari, J.K. Koskinen, and T. Mattila, “Phase Noise in Capacitively Coupled Micromechanical Oscillators", IEEE Transactions on Ultrasonics, Ferroelectrics, and Frequency Control, volume 52, no. 12, 2005, pp. 2322-2331

[2.3] M. Agarwal, S.A. Chandorkar, R.N. Candler, B. Kim, M.A. Hopcroft, R. Melamud, M. JHA Chandra, T.W. Kenny, and B. Murmann, “Optimal Drive Condition for Nonlinearity Reduction in Electrostatic Microresonators”, Applied Physics Letters 89, 214105, 2006

[2.4] V. Kaajakari and T. Mattila, “Nonlinear Limits for Single-Crystal Silicon Microresonators”, Journal of Microelectromechanical Systems, volume 13, no. 5, 2004, pp. 715-724

[2.5] V. Kaajakari, “MEMS Tutorial: Nonlinearity in Micromechanical Resonators”, http://www.kaajakari.net

[2.6] J. Brotz, “Damping in CMOS-MEMS resonators”, Master thesis report, Carnegie Mellon University, 2004

[2.7] F. R. Blom, S. Bouwstra, M. Elwenspoek, and J. H. J. Fluitman, “Dependence of the quality factor of micromachined silicon beam resonators on pressure and geometry”, Journal of Vacuum Science and Technology B, volume 10, issue 1, 1992, pp. 19-26

[2.8] T. Corman, P. Enoksson, and G. Stemme, ”Gas damping of electrostatically excited resonators”, Sensors and Actuators A: Physical, volume 61, issues 1-3, 1997, pp. 249-255

[2.9] A. Duwel, R. N. Candler, T. W. Kenny, and M. Varghese, “Engineering MEMS Resonators with Low Thermoelastic Damping”, Journal of Microelectromechanical Systems, volume 15, no. 6, 2006, pp. 1437-1445

[2.10] P. Mohanty, D. A. Harrington, K. L. Ekinci, Y. T. Yang, M. J. Murphy, and M. L. Roukes, “Intrinsic dissipation in high-frequency micromechanical resonators”, Physical Review B, volume 66, issue 8, 2002, pp. 085416

[2.11] Y.-H. Park and K. C. Park, “High-Fidelity Modeling of MEMS Resonators—Part I: Anchor Loss Mechanisms Through Substrate”, Journal of Microelectromechanical Systems, volume 13, no. 2, 2004, pp. 238-247

[2.12] F.D. Bannon, J.R. Clark, and C.T.-C. Nguyen, “High-Q HF microelectromechanical filters,” IEEE Journal of Solid-State Circuits, volume 35, no. 4, 2000, pp. 512- 526

[2.13] T. Mattila, J. Kiihamäki, T. Lamminmäki, O. Jaakkola, P. Rantakari, A. Oja, H. Seppä, H. Kattelus and I. Tittonen, "A 12MHz Micromechanical Bulk Acoustic Mode Oscillator", Sensors and Actuators A, volume 101, 2002, pp. 1-9

[2.14] T. Mattila, A. Oja, H. Seppä, O. Jaakkola, J. Kiihamäki, H. Kattelus, M. Koskenvuori, P. Rantakari, and I. Tittonen, “Micromechanical Bulk Acoustic Wave Resonator”, IEEE Ultrasonics Symposium, 2002, 945-948

[2.15] B. Bircumshaw, G. Liu, H. Takeuchi, K. Tsu-Jae, R. Howe, O. O'Reilly, A. Pisano, “The Radial Bulk Annular Resonator: Towards a 50Ω RF MEMS Filter”, The 12th International Conference on Solid-state Sensors and Actuators (Transducers '03), 2003, pp.875-878

Chapter 3

Nanogap MEM Resonator Technology

This chapter describes in detail the original nanogap fabrication process used in this thesis. Based on a lateral spacer technique, we manufacture lithographic constraint-free, fully monocrystalline silicon resonators with very narrow transduction gaps.
The chapter starts with an introductory part which briefly reviews the current silicon-based nanogap resonator fabrication methods. Most interesting and effective, the lateral-spacer technique stands as starting point for the fabrication process developed during this work. Detailed descriptions of each fabrication step are given, including discussions on the main challenges and their solutions.
Successful characterization of the devices fabricated with this process is presented in Chapter 4.

3.1. Motional Resistance Reduction: Role of Gap Scaling and Silicon Film Thickness

Micro-Electro Mechanical (MEM) resonators promise to be a viable alternative to stable but bulky quartz crystals, due to their remarkably miniaturized sizes which allow high integration levels. In order to extend the operating frequencies domain in the MHz to GHz range, the resonator size, so also the actuation area is dramatically decreasing, and it becomes challenging to maintain acceptable resonator impedance (R_m) and power levels. Moreover, if one would like to maintain a reasonable capacitance coupling for resonators realized on relatively thin films (less than 10μm), it becomes extremely important to significantly reduce the actuation gap which separates the resonator from the fixed electrodes.

As detailed in Chapter 2, the motional resistance of a MEM bulk lateral resonators (BLR) can be calculated as [3.1]:

$$R_m = \frac{\sqrt{k_{eff} m_{eff}}}{Q\eta^2} = \frac{\sqrt{k_{eff} m_{eff}}}{V_{DC}^2 Q\varepsilon_0} \times \frac{g^4}{h^2 w^2 L} \qquad (3.1)$$

where k_{eff} and m_{eff} are the effective spring constant and mass, Q is the quality factor and η is the electromechanical coupling coefficient. In the second part of the expression, V_{DC} is the bias voltage and ε_0 is the vacuum permittivity; g is the gap width, h the silicon layer thickness and L and w are resonator length and width, respectively.

As Equation (3.1) shows, in order to meet the specifications for practical applications, e.g. low motional resistances at low DC biases and high quality factors, it is essential to decrease the gap width, while maximizing the trench aspect-ratio (h/g) as much as possible. Also, as the quality factor is proportional to the resonator mass, the thickness (which doesn't affect the resonance frequency) can be maximized for improved performance.

As an example, let's consider a beam resonator which vibrates laterally in a bulk mode, as shown in Figure 3.1. The resonator parameters are summarized in Table 3.1. For this device, we can calculate the motional resistance value as a function of the transduction gap width using Equation (3.1). The resulting values are plotted in Figure 3.2., for two different resonator silicon film thicknesses, which correspond to the SOI wafers used in this work. For R_m values below 500kΩ, the gap should measure less than 200nm. We have targeted and achieved gaps in the 100nm range, with aspect-ratios as high as [60:1].

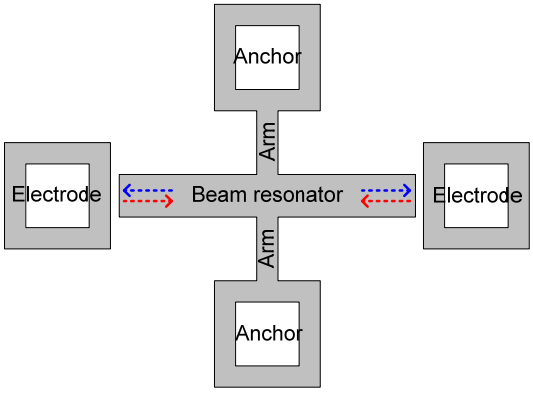

Figure 3.1. Schematic of a longitudinal beam resonator

Table 3.1. Longitudinal beam resonator design and material parameters

Layer thickness, h [μm]	1.5 / 6.25
Resonator width, w [μm]	10
Resonator length, L [μm]	161
Resonance frequency, f_{res} [MHz]	26
Vacuum permittivity, ε_0 [$A^2s^4kg^{-1}m^{-3}$]	8.85E-12
Young's modulus, E [GPa]	165
Density, ρ [kg/m^3]	2330
DC bias, V_{DC} [V]	10
Quality factor, Q	100'000

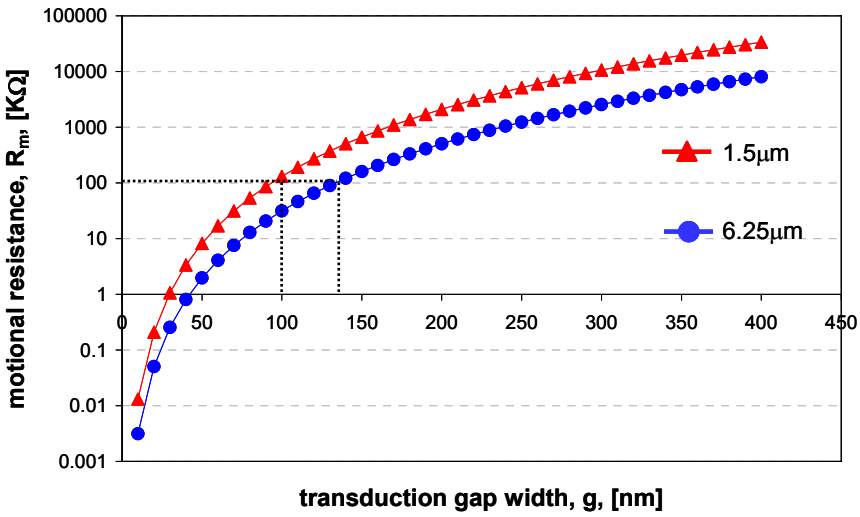

Figure 3.2. Motional resistance dependence on the gap width of the beam BLR for two different resonator thicknesses: 1.5μm and 6.25μm.

The silicon film thickness choice was made keeping in mind that the thicker the device layer, the more relaxed will be the requirements on needed nanogap width, in order to reach a given motional resistance. Moreover, for thicker film resonator, higher quality factors can be expected, due to larger mass and thus increased energy storage. A middle ground had to be found between the layer thickness and the gap width, so the first technology run was carried out on 1.5μm-thin SOI, and the second one on 6.25μm. This thickness range corresponds to partially depleted SOI, which can be a substrate of choice for the fabrication of future integrated hybrid MEMS-CMOS integrated circuits for communication applications.

3.2. Silicon-Based Lateral Nano-Gap Fabrication Methods

Several different methods have been reported in the literature for achieving resonators with very narrow, nanometer-sized gaps on silicon platforms, which will be discussed further on:

- By **FIB-milling**, nano-gap MEM single-crystal-silicon (SCS) resonators can be rapidly prototyped [3.2] by locally milling very narrow gaps in the hard mask layer using gallium ions from the focused ion beam, and then transferring them into the silicon resonator layer through dry etching. Gaps with widths in the order of 50nm have been obtained in 300nm and in 1.3μm silicon films, as shown in Figure 3.3. This process though is only suitable for fabricating a small number of test structures and not for batch processing. Other inconvenients are the local contamination with gallium ions and the possible silicon amorphization.

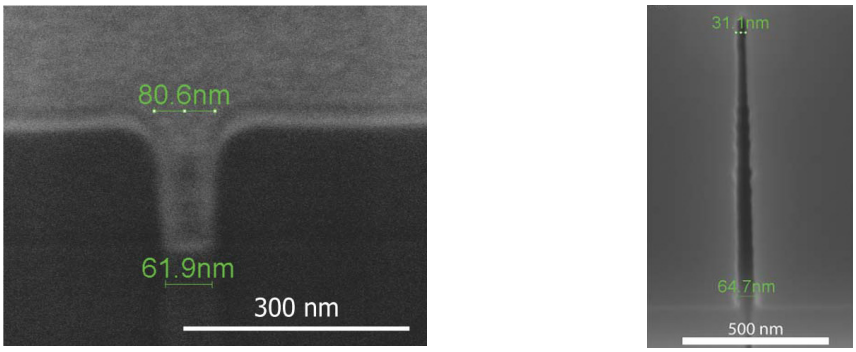

(a) (b)

Figure 3.3. Cross section through nanogaps obtained by FIB milling of the mask and transfer into (a) 300nm and (b) 1.3μm SOI layers [3.2]

- **E-beam lithography** can be used to pattern very narrow trenches. Widths in photoresist as small as 47nm have been testified [3.3] However, this paper reports 120nm-wide gaps with a depth of 400nm, probably due to etch-related widening (Figure 3.4).

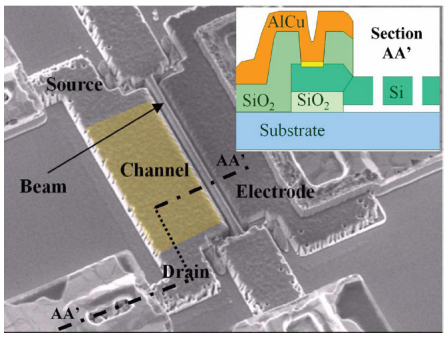

Figure 3.4. SEM picture of a beam resonator with 120nm-wide gaps, patterned by e-beam lithography [3.3]

Even though the resolution achievable by e-beam lithography is remarkable, the process is slow and expensive, thus not very well suitable for mass production. Also, another e-beam related challenge is the need of advanced dry-etching recipes, capable of transferring the pattern in the silicon layer with high selectivity with respect to the photoresist, and in the same time avoiding excessive widening of the gap.

- Another possibility is to employ a **gap reduction** technique [3.4]. The hard mask is initially composed of two layers: silicon nitride and polysilicon on top. The polysilicon is patterned by optical photolithography and then it is oxidized, thus the gap widths reduce to sub-micrometer dimensions. The oxide is then used to etch through the silicon nitride and the silicon, resulting in gap widths as small as 200nm, with aspect ratios of [60:1], shown in Figure 3.5. Main drawbacks of this method include the gap width variation of up to 50nm at wafer level, and mask-induced vertical sidewall striation.

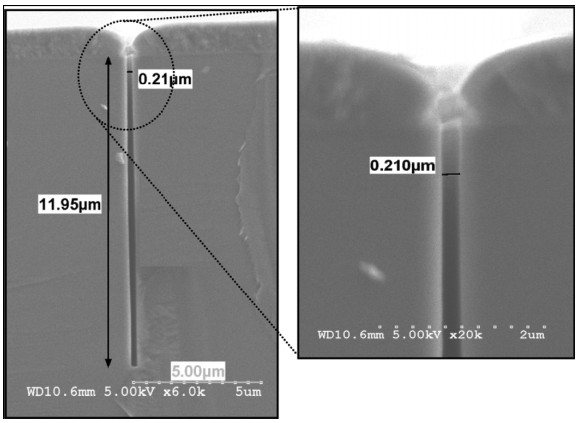

Figure 3.5. SEM cross sections through 210nm gaps with [60:1] aspect ratios, fabricated by gap reduction [3.4].

- A very promising method is the **lateral gap-spacer** technique, which defines vertical gaps by depositing a very thin vertical layer between two structures composed of a different material, and then by selectively removing it. Thus, a lithography free, very narrow space is left between the two structures. This thesis work is based on the same principle, as will be explained further on.

  One possible approach, suitable for MEMS-last cointegration with electronics, is to fabricate poly-SiGe devices using a poly-Ge spacer. Early work [3.5] has shown problems with the stress and strain in the structural layer, causing great reduction of the transduction gaps (to almost zero) and vertical deflection of the resonators. Other reported problems were related to gap widening during release due to low selectivity of the wet etch solution between poly-Ge and poly-SiGe and also very high temperature drift of the resonance frequency of certain

flexural designs due to thermal mismatch between the poly-SiGe structure and the Si substrate. More recent results [3.6] demonstrate improvements in deposited poly-SiGe stress levels and in etch selectivity. The thermal drift was also reduced using centrally-anchored disk designs. Images of the reported device are presented in Figure 3.6.

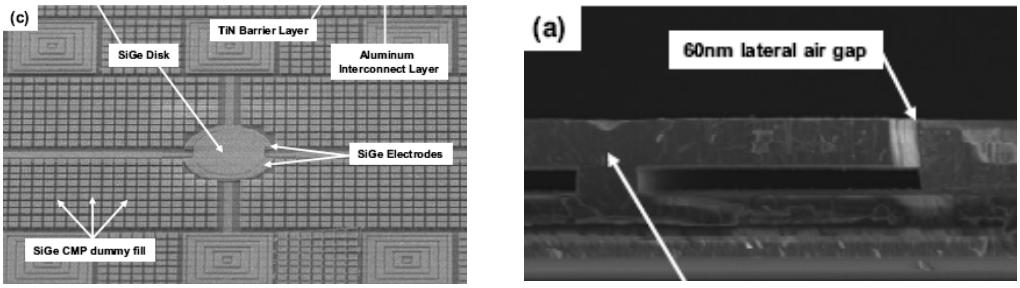

(a) (b)

Figure 3.6. SEM image of a poly-SiGe disk (a) top-view and (b) cross-section [3.6].

Other groups have used silicon oxide or polysilicon spacer layers to fabricate nano-gap resonators composed from different materials, as will be later discussed. SEM images of such resonators are shown in Figure 3.7.

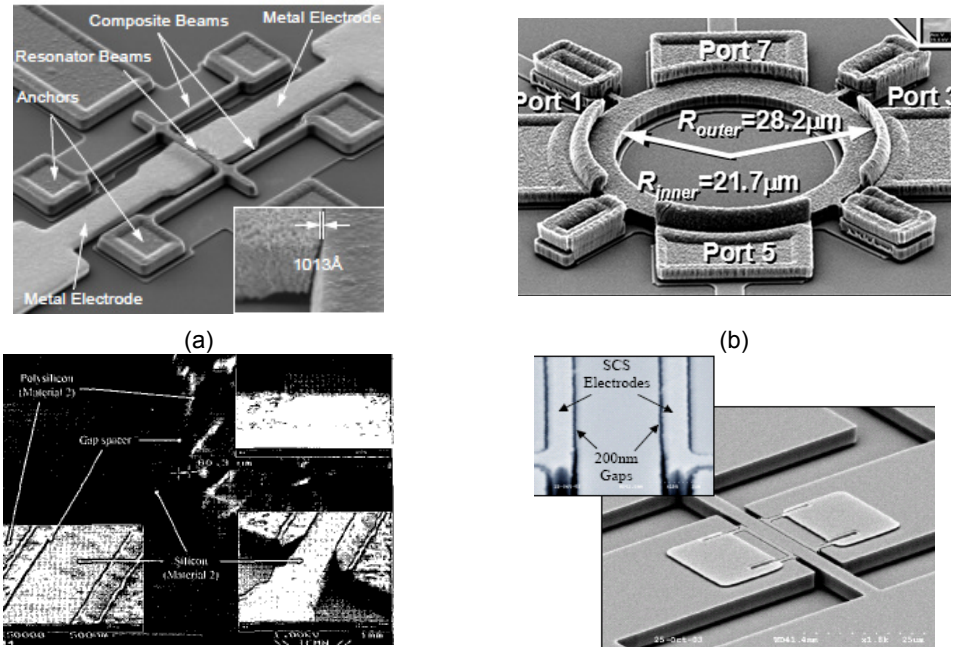

(a) (b)

(c) (d)

Figure 3.7. (a) SEM image of a polysilicon beam resonator with metal electrodes [3.7], (b) SEM image of a fully polysilicon resonator [3.8], (c) SEM close-up of an SCS resonator with polysilicon electrodes [3.9] and (d) SEM image of a fully SCS beam resonator [3.10]. Devices in the first three images were fabricated using an oxide spacer, while the last one employed polysilicon.

Among the possible material combinations achieved on silicon platforms manufactured using an oxide spacer, the most notable are: polysilicon resonators with metal electrodes [3.7] or polysilicon electrodes [3.8] and monocrystalline silicon resonators with polysilicon electrodes [3.9]. Gaps with widths of less than 100nm have been reported. By increasing the complexity of the method, fully-SCS resonators (and electrodes) were fabricated using a polysilicon spacer. Nano-gaps were created in an oxide hard mask, which were then transferred into the silicon film. Gaps with widths of 130nm and [20:1] aspect ratios were achieved [3.10].

Table 3.2 (on the next page) summarizes the main silicon-based nanogap resonator fabrication techniques which have been previously discussed:

Table 3.2. Summary of nanogap fabrication techniques

Technique		Device material	Gap width / A.R.	Issues
FIB		SCS	50nm / [26:1]	+ Fast prototyping - Serial process, not suitable for batch fabrication - Advanced dry etching needed - Local Ga+ contamination - Possible silicon amorphization
E-Beam		SCS	120nm / [5:1]	+ Very good resolution - Expensive, slow process
Gap reduction		SCS	200nm / [60:1]	+ Batch processing + Cost effective + Thick mask => deep gaps - 50nm gap width variation at wafer level - Vertical sidewall striation - Advanced dry etching needed
Lateral nanogap-spacer	Poly-Ge	Poly-SiGe resonator and electrodes	60nm / [33:1]	+ MEMS last process allows vertical stacking of structures => low die size and reduced interconnect parasitics + Low thermal budget (<450°C) possible + Ohmic poly-SiGe contact with the interconnects, with no performance degradation compared with SiGe only - Need good control of stress levels in the poly-SiGe layers - Non fully crystalline resonators
	Oxide	Polysilicon resonator with metal or polysilicon electrodes	100nm / [30:1]	+ Batch processing + Very narrow gaps, without the need of advanced etching - Limited by oxide conformity - Non fully crystalline structural material => more material losses, debris trapped in gaps during release, inferior electrical isolation between input and output, lower polarization voltage tolerance
		SCS resonator with polysilicon electrodes	60nm / n.a.	
	Polysilicon	SCS	130nm / [20:1]	+ Batch, cost effective processing, + Fully SCS structures (resonator and electrodes) + Very narrow, uniform gaps, defined by polysilicon layer thickness - Advanced dry etching needed

3.3. Lateral Spacer Technique

The goal of our project has been to manufacture nano-gap MEM resonators employing conventional techniques only, especially with the use of normal optical photolithography. We have focused our efforts on obtaining trenches with widths of the order of 100nm, with a depth of more than 1.5μm without the use of any advanced lithography technique, like DUV or E-beam. All four masks used in the process were transferred using a SüssMicrotec MA150 1x Exposure-Aligner with maximum achievable resolution of 0.8μm.

As depicted in Figure 3.8, the spacer layer technique consists of interposing a thin vertical layer of material between two layers of a different one. This way, the middle layer will act as a spacer between the other two, and by selectively etching it, we can obtain a narrow trench. The width of the gap will be defined by the spacer layer thickness, which, depending on the material choice, can be extremely well controlled. Thus, we have managed to obtain much smaller features than the optical resolution.

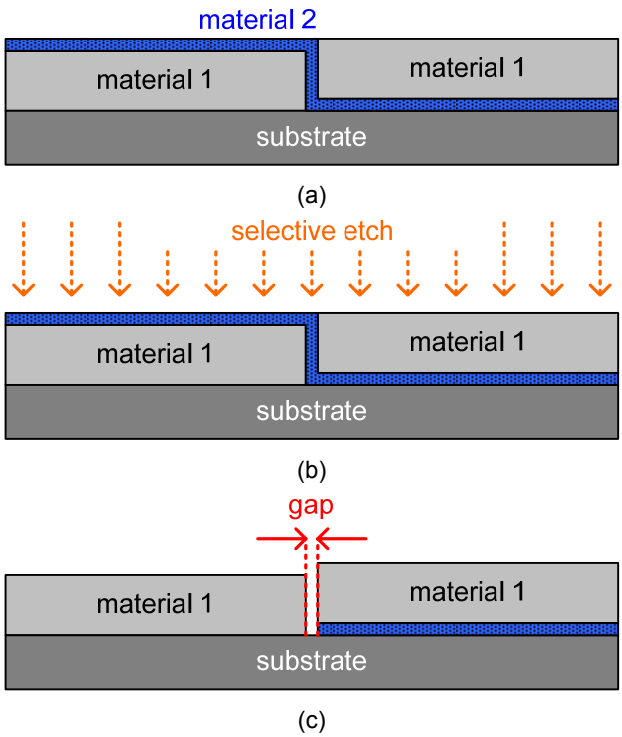

Figure 3.8. Spacer layer technique: (a) alternate layer arrangement, (b) removal of spacer by selective etch and (c) nanogap mask resulted after spacer removal

3.4. Process Flow

The detailed nanogap fabrication process is reported in Figure 3.9, which shows the main process steps by depicting the device cross-sections. All steps of the nano-gap MEM resonator fabrication process were developed at EPFL Center on Micro-Nanotechnology (CMI)[1] except for the TEOS deposition.

The starting material is Silicon-On-Insulator (SOI) substrate, with a silicon film thickness of 1.5μm and 1μm buried oxide (BOX). A three-layer deposition process is used to create the resonator hard mask, employing a sacrificial-layer technique. The process uses a total of four masks. Process run-cards for both SOI thicknesses can be found in Appendixes A and B.

First, a tetraethyl orthosilicate (TEOS) layer with 500nm thickness is deposited and patterned by dry etching (Figure 3.9.a), in order to form a hard mask for the MEM resonating structure and anchors. A polysilicon layer with a thickness of less than 100nm is then deposited (Figure 3.9.b), which will act both as nano-gap spacer and as protection for the first oxide during dry-etch patterning of the second one. Next, a second TEOS layer of 1.5μm is deposited (Figure 3.9.c), followed by a combination of Chemical Mechanical Polishing (CMP) and wet etch in order to expose the polysilicon layer (Figure 3.9.d). A second photolithography step and a dry SiO_2 etch will define the resonator's electrodes (Figure 3.9.e). At this stage, the hard-mask which will be used to etch the Si MEM resonator is complete. The structure is then etched with a low-frequency pulsed plasma ICP-RIE in order to avoid Si notching at the BOX interface (Figure 3.9.f), and the oxide hard mask is removed using a buffered HF (BHF) solution (Figure 3.9.g). Subsequently, using a third mask, the undoped polysilicon is removed from the contact area (Figure 3.9.h), and metal is plated and patterned with a fourth mask (Figure 3.9.i). At last, the structure is released in buffered HF etch, as depicted in Figure 3.9.j.

The typical process steps used for fabricating 1.5μm-thick nanogap MEM resonators are described in detail in Appendix A.

---

[1] The Center of MicroNano Technology, CMI, is in charge of a complex of cleanrooms in EPFL, managed by a staff of specialists which offers basic and advanced training and access to processing equipments for both cleanroom users and EPFL students in the field of microtechnology. The main cleanroom is divided into seven different class 100 zones, connected together by class 1'000 corridors and class 10'000 material access areas. Each zone groups equipments by the type of process (lithography, dry or wet etching, material deposition etc.). More details about the CMI can be found on their web site [3.11].
While different techniques for patterning nano-gaps are available in the CMI, like FIB-milling and an e-beam lithography system acquired in 2006, our process explores the possibilities of achieving very narrow gaps (in the order of 100nm) by using conventional optical photolithography, through the spacer-layer technique.

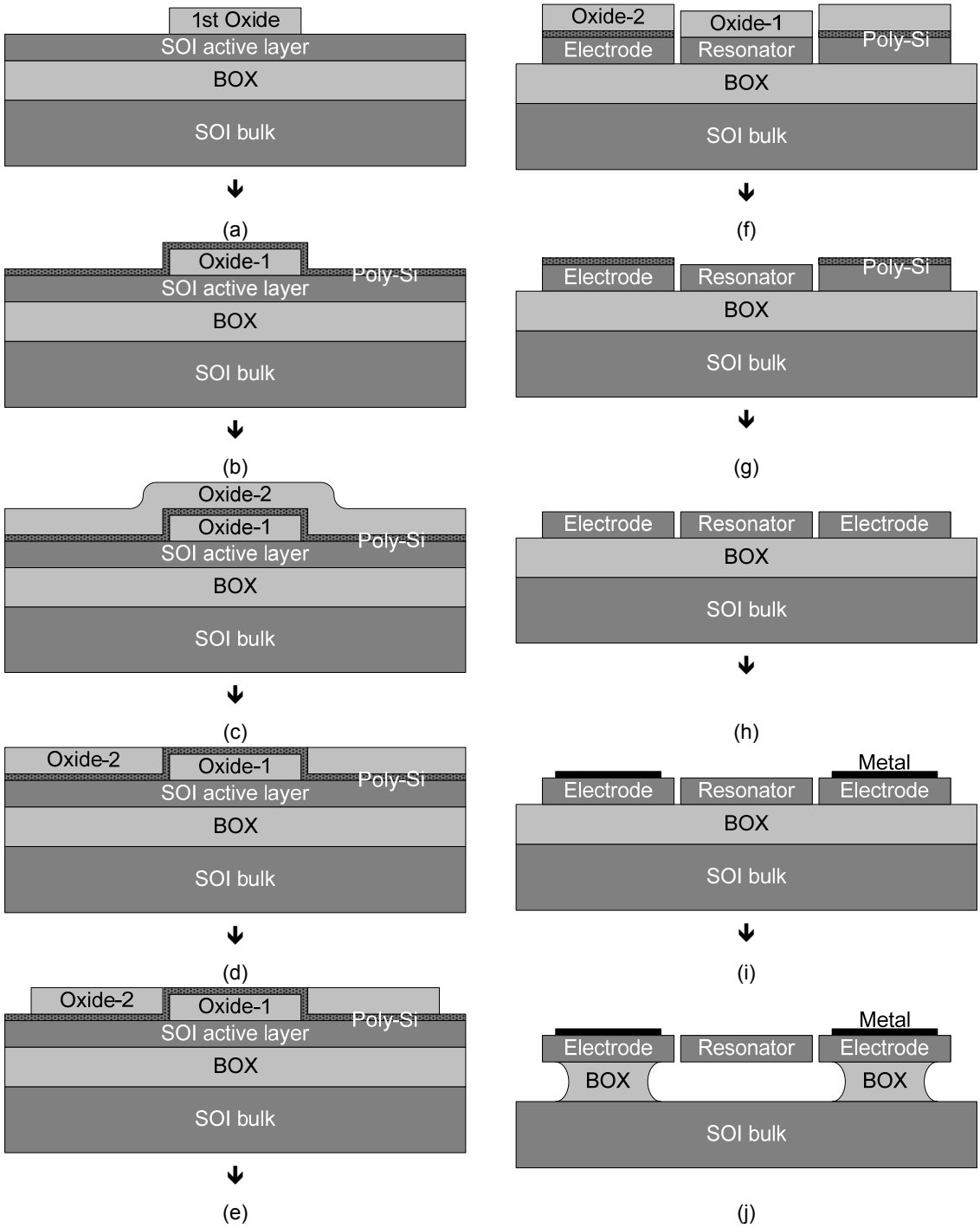

Figure 3.9. Process flow steps: (a) TEOS layer deposition and mask 1: patterning of the resonator structure hard mask, (b) deposition of the thin polysilicon gap spacer, (c) deposition of the second oxide layer which forms the hard mask, (d) CMP and BHF back-etch of the second oxide to reveal the polysilicon layer, (e) mask 2: patterning of electrodes, (f) transferring the hard mask into the silicon film by dry etch, (g) mask oxide removal, (h) mask 3: opening of electrode contacts in the polysilicon layer, (i) metal deposition and patterning using mask 4, and (j) final structure wet etch release and critical point drying

3.5. Hard Mask Formation and CMP Optimization

The deep sub-micron openings in the TEOS hard mask which are used to etch the nano-gaps are obtained by depositing and then selectively removing a very thin polysilicon spacer layer. The PolySi LPCVD has very good uniformity; therefore the in-wafer nano-gap mask opening variation is smaller than ±5%.

It is important that after patterning the first mask, the TEOS sidewalls are very smooth and vertical. Otherwise, the polysilicon gap spacer which follows exactly the shape of the structure will be tilted and the plasma won't have directional access to the SOI layer when etching the resonators. For this reason, the first photolithography step is essential, as well as a selective and smooth oxide dry-etch recipe.

A second oxide is then deposited above the polysilicon, and then etched back with a combination of CMP and BHF wet etch, until the spacer layer is uncovered. It is important that the polysilicon layer isn't damaged by the etching process, because later on it will be used to protect the oxide underneath during the selective dry etch for patterning the electrodes. The CMP speed is highly dependent on the pattern density and size, the general rule being that some wide, high-density patterns planarize the slowest and narrow, isolated features planarize the fastest. Therefore, in some areas, the polysilicon layer will be exposed faster and it will start to erode. Since the layer thickness is of 100nm or less, there is a high risk of punching through the polysilicon in the areas with less dense pattern. This problem can be avoided by stopping the CMP before reaching the polysilicon layer, and by finishing the oxide back-etch with a short BHF step. The CMP parameters are summarized in Table 3.3.

Table 3.3. CMP parameters

Slurry	30N50
Head speed	30 rpm[1]
Platen speed	35 rpm
Back pressure	0.02 psi[2]
Working pressure	1.04 psi

Special attention must be paid to the second oxide deposition. At first, LPCVD low temperature oxide (LTO) has been tested, and the electrodes were etched using BHF. The SEM images taken at this point (Figure 3.10.a) revealed that voids were formed during LTO deposition, which were etched faster in BHF, generating an uneven shape in the hard mask at the electrode corner in contact with the polysilicon spacer. For this reason, as shown in Figure 3.10.b, after etching the gaps, the trench interface with a wider opening was very rough, strong skirting effect being observed.

[1] rpm = rotations per minute
[2] psi = pounds per square inch

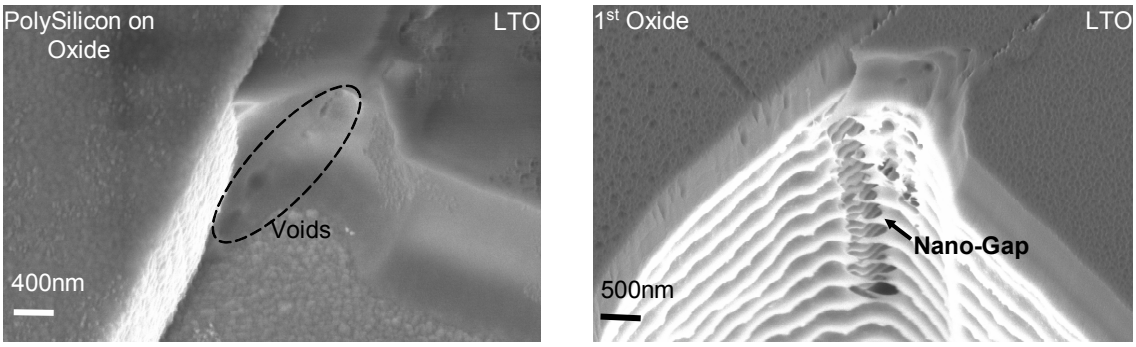

(a) (b)

Figure 3.10. SEM pictures showing (a) voids in the LTO layer after patterning the electrodes and (b) the strong skirting resulted after gap etching

In order to solve this problem, the process flow was improved by replacing the LTO with LPCVD TEOS, which has better step-coverage and higher density, and by etching the electrodes with selective anisotropic C_4F_8 plasma etch instead of wet BHF-etch. The results obtained with the improved process are shown in Figure 3.11. Figure 3.11.a presents an SEM image of the void-free interface between the TEOS and the structure, and Figure 3.11.b shows the skirting-free gap, etched with the TEOS hard-mask.

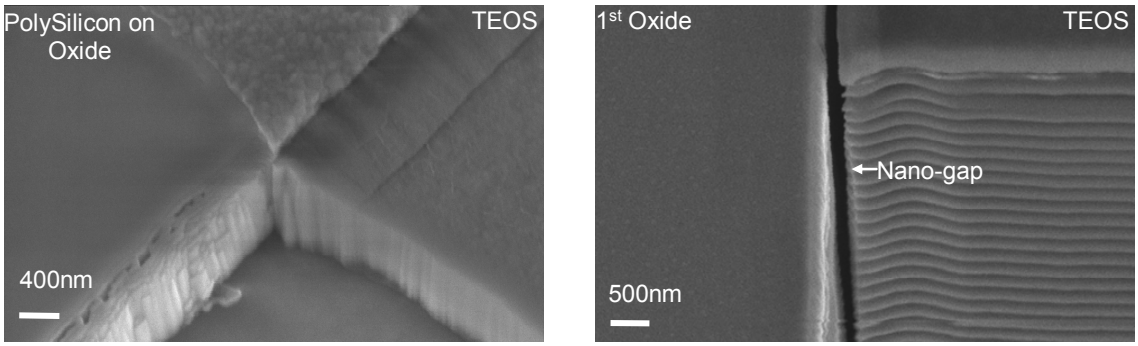

(a) (b)

Figure 3.11. SEM pictures of the improved process, showing the hard mask after patterning the electrodes with a dry plasma etch (a) and the etched nano-gap (b)

3.6. Nano-Gap Etch

A typical gap of 110nm, obtained with a Bosch-like process called Super High Aspect Ratio Process (SHARP), developed at Alcatel Vacuum Technology [3.12], is depicted in Figure 3.12. To our knowledge, this is one of the smallest actuation gaps results reported to date for SOI MEM resonators. As shown in Figure 3.12.a, the scalloping-induced vertical roughness is limited on the top of the gap to 30nm, and is decreasing with depth. The lateral roughness, generated mainly by photolithography, sidewall thickness-variation and etching is quasi-negligible (<10nm, Figure 3.12.b).

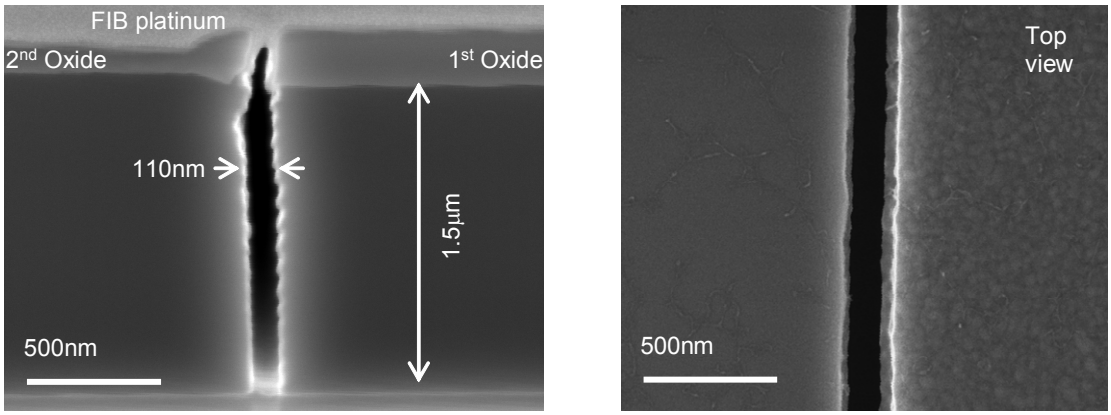

(a) (b)

Figure 3.12. (a) FIB-cut through a 110nm-wide, 1.5µm-deep nanogap and (b) top view of the gap after hard mask removal

3.6.1. Continuous vs. Bosch-like process

One of the most critical steps of the process is the deep sub-micron gap etch. Two different techniques have been evaluated, a continuous etch-process, and the Super High Aspect Ratio Process (SHARP), developed at Alcatel Vacuum Technology.

The continuous process uses a mix of etching (SF_6) and passivating (C_4F_8) gasses, and due to the directional ion bombardment, the passivation layer is removed at much higher rate from the bottom of the trench, exposing it to the etch. This process has the advantage of generating smooth walls, but it proved to be very sensitive to any angle in the hard-mask opening, caused by the first photolithography step, as shown in Figure 3.13:

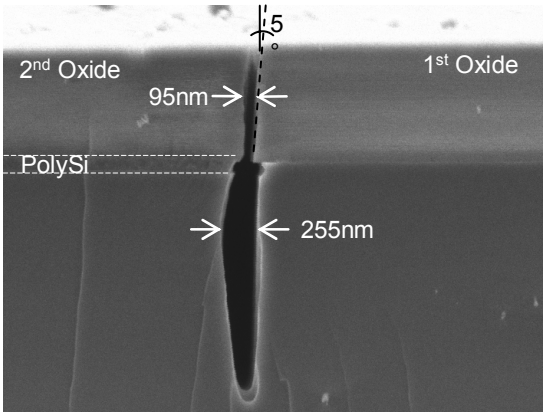

Figure 3.13. SEM picture of a nano-gap etched using the continuous process

In the picture above we can see that as the ions which are reaching the substrate are not coming under a 90°, but a slightly smaller angle, one of the trench walls is bowed, noticeably increasing the gap-width.

Better results were obtained starting from the SHARP process, based on the Bosch technique, which uses alternating etching and passivating steps to achieve high aspect ratio trenches in silicon. The Bosch process has its limitations, among which we can consider the scalloping-induced wall roughness, the large undercut and the aspect-ratio limited to maximum [30:1]. When used for etching deep sub-micron trenches, all these effects become critical, being a major limiting factor. The main SHARP process improvements include: (1) fast-switching of etching and passivating steps to reduce the wall roughness, (2) raising the platen power and decreasing the pressure for a longer ion mean free path, (3) adding an O_2 plasma step for better polymer removal and (4) decreasing the substrate temperature for higher mask selectivity.

Figure 3.14 shows the SEM picture of a 200nm-wide and 7.5μm-deep gap etched with this technique. Aspect-ratios of [40:1] and low scalloping, thus smooth vertical walls have been demonstrated. The limiting factor for the achieved trench depth was the etch selectivity between silicon and the oxide hard-mask. For further tests regarding the maximum achievable aspect ratio, thicker oxide hard-mask should be used.

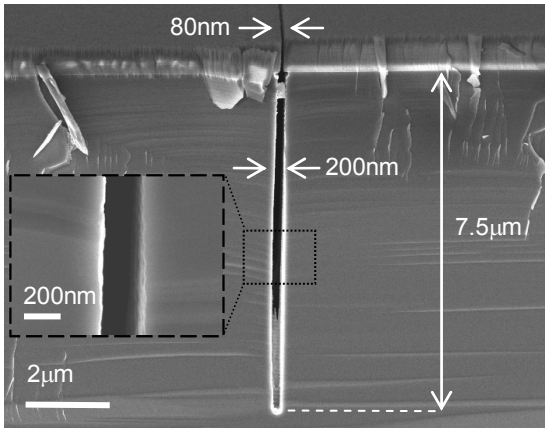

Figure 3.14. SEM picture of a 200nm-wide and 7.5μm-deep trench, etched with a SHARP-based process

3.6.2. Notching Effect

Deep Reactive Ion Etch (DRIE) processes have different silicon etch-rates in different areas of the wafer, due to loading effects as the Aspect-Ratio-Dependent-Etch (ARDE) or the general loading effect by which edges of the wafer etch faster than the center [3.13]. The same applies to the SHARP process, whose etch-rate is more than two times lower in the nano-gap area than in the large openings. For this reason, wide opened spaces on the wafer will be overetched by as much as 150% until the nano-gaps are completely opened.

At the same time, as it can be seen in Figure 3.15.a, plasma etching of silicon over an insulator layer can result in a notching problem at the silicon/insulator interface, due to trapped charges in the insulator which induce bending of the trajectory of ions. The

notch size is proportional to the etch time, so large overetch of the big openings results in significant notching effect.

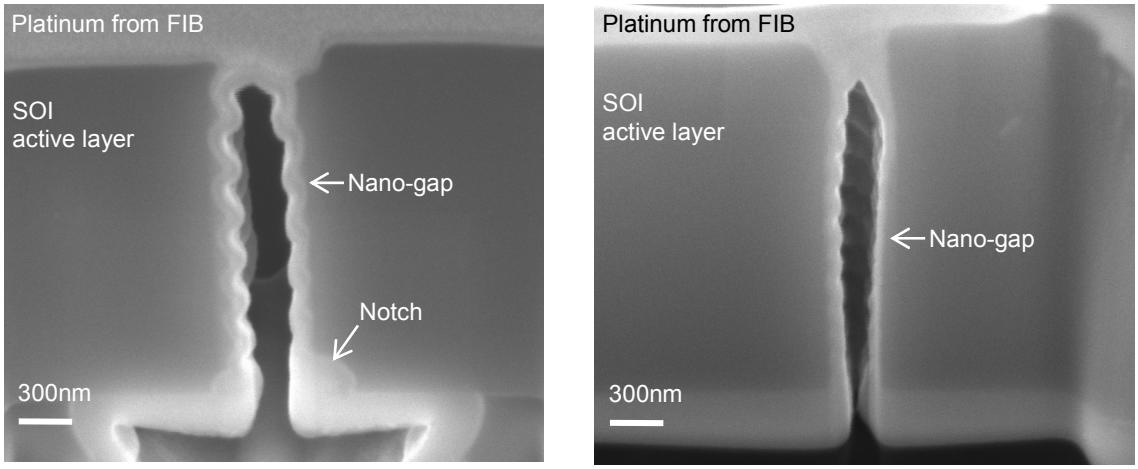

(a) (b)

Figure 3.15. FIB cross-sections of fully etched nano-gaps showing (a) notching and (b) notch-free profile obtained with an Adixen AMS 200 DSE etcher.

This effect can be avoided by using a low frequency pulsed substrate polarization, which allows the ions to escape, preventing charge accumulation. We have used an Adixen AMS 200 DSE etcher and a typical notch-free result is shown in Figure 3.15.b.

3.6.3. Skirting Effect

One additional phenomenon related to the DRIE processes, which can cause a short circuit between the electrodes and the resonating structure, is the so called “skirting effect”. Due to over-passivation, the etch fails to entirely remove the silicon at the interface between narrow trenches and larger openings, producing a result as shown in Figure 3.16.

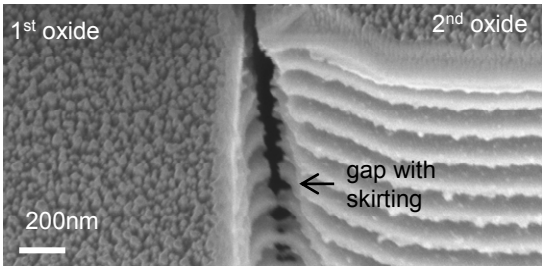

Figure 3.16. SEM picture of the nano-gap interface with a large opening, showing an extreme case of skirting

Since the skirting effect cannot be solved by modifying the process parameters without affecting the selectivity of the etch, the undercut and the gap profile, a special anti-

skirting design was conceived. The design uses a smooth transition between the trench and the open area, as shown in Figure 3.17.

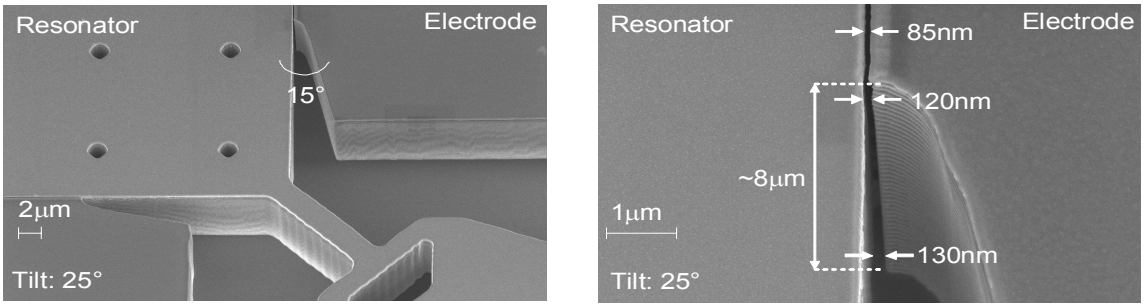

(a) (b)

Figure 3.17. SEM picture of (a) an anti-skirting designed nano-gap MEM resonator and (b) technological validation of the design

Due to high SOI wafer price, all anti-skirting tests were done on bulk silicon wafers. From the figure above we can see that the anti-skirting design solves the problem for depths of up to 8μm. However, on SOI wafers results are slightly different, and skirting occurs after around 6μm, as will be discussed in Section 3.8.

3.7. Metallization, Final Release and Critical Point Drying

The fabrication run on 1.5μm silicon films has used a stack of metals composed of 50nm TaN sputtered seed layer, 150nm sputtered Cu, 3μm plated Cu, and 300nm plated Au for passivation (listed from bottom to top). The metallization was done by our EU project partner, IMEC Belgium.

In the end of the first run, an unexpected compatibility issue has been noticed between the metallization gold and the n+, low resistivity wafers used, which caused galvanic corrosion [3.14] of all structures when dipped in the final BHF release bath. Due to this effect, the actual gaps were increased to around 250 - 300nm and the film was slightly thinned down from 1.5μm to ~1.3μm.

The corrosion problem was solved in the next fabrication run, on 6.25μm-thick SOI, as it will be described in the next section.

The final critical step of the process was the resonator drying. The 1.5μm-thick structures are not stiff enough to endure air-drying, and they collapse under the high tension forces. Therefore, critical point drying (CPD) of the structures was employed, which increases the temperature and pressure inside a liquid CO_2-filled chamber bringing the carbon dioxide at a supercritical state, where the distinction between gas and liquid ceases to apply.

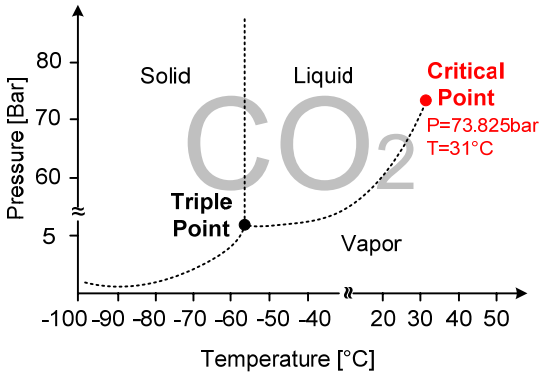

Figure 3.18. CO_2 phase diagram. Beyond a specific temperature and pressure (the critical point), the carbon dioxide becomes a supercritical fluid, a state that is neither gas nor liquid, but has properties of both

The CO_2 phase diagram is shown in Figure 3.18 [3.15]. After reaching the supercritical region, the pressure inside the chamber is slowly vented away, while keeping the temperature constant, and bringing the CO_2 to the gas phase. By this technique, no structure collapsed due to stiction. A fully released and dried MEM resonator with nanogaps is shown in Figure 3.19.

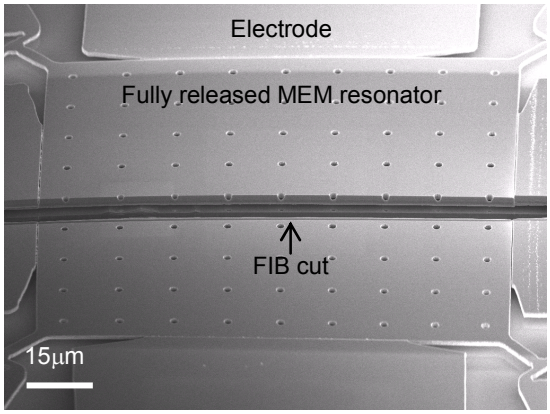

Figure 3.19. SEM image of a fully released MEM resonator, showing an FIB-cut through the structure

3.8. Resonator Fabrication on 6.25μm SOI

An extension of the process flow described in Section 3.4 was used to fabricate MEM resonators on SOI wafers with 6.25μm-thick silicon film. The BOX thickness is 3μm.

While most of the steps remained similar to the 1.5μm-Si process, the deposited layer thicknesses and etch times had to be adapted, and a few additional steps were introduced. A typical 6.25μm SOI wafer runcard can be consulted in Appendix B.

First change was to increase the first oxide thickness to 1μm (instead of 500nm for the 1.5μm-SOI batch). Given the [14:1] etch selectivity of the SHARP-process between oxide and silicon in the nanogaps and the fact that after CMP & BHF, the second oxide

is always thinner than the first oxide, this mask thickness corresponds at the limit to a maximum achievable nano-gap depth of 6.25μm. Actually, it is so close to the limit, that without very good control of the CMP process, some of the structures start to be etched away because of mask punch through. In the same time, the mask thickness cannot be increased more than 1μm, while keeping the same polysilicon layer and thus the same targeted nanogap widths, because of the [12:1] selectivity between TEOS and PolySi of the oxide-etch recipe. In the future, better control of the CMP process, and design improvement by adding CMP dummy-structures for pattern uniformity should be considered, in order to reach higher nanogap depths.

For 6.25μm-thick structures, the anti-skirting design proved not enough to completely solve the problem. This surprising result was probably due to the different etching conditions on SOI wafers, than on silicon bulk wafers. Thus, a very short additional isotropic Si etch step was introduced, subsequent to a quick BHF-dip of the wafer for native oxide removal, which would otherwise prevent the silicon from being etched away. This step removed only the skirting, while due to the smaller etch-rate inside narrow trenches, it introduced very little or no enlargement of the transduction gaps.

Another challenge when transferring the process on thicker substrates was to perform the last photolithography step, due to the high topography (~10μm). Much thicker photoresist (8μm) had to be used, with a corresponding longer exposure time.

As mentioned in Section 3.7, the incompatibility issue between the gold used to passivate the metallization stack and the BHF-etch was solved by replacing the TSM with aluminum, and by releasing the structures with Silox-etch instead of BHF.

Finally, the drying step proved to be more straightforward than for the 1.5μm-layer batch, because the structures were stiff enough to withstand air drying. Thus, some of the wafers were dried in the CPD, while for the others the water was first replaced by isopropanol and then by acetone, and then they were air dried. Comparison of the two methods showed same results: no drying-related stiction for any of them.

Figure 3.20.a shows an FIB cross-section through the transduction gap separating the electrode and the resonator, and Figure 3.20.b. an SEM top-view image of the successfully released fragmented-membrane resonator. The notch visible on the gap-top in the first image is generated by a small tilt of the vertical polysilicon wall which acts as gap-spacer (~5° deviation from vertical position), combined with the long etch-time needed to completely open the gaps.

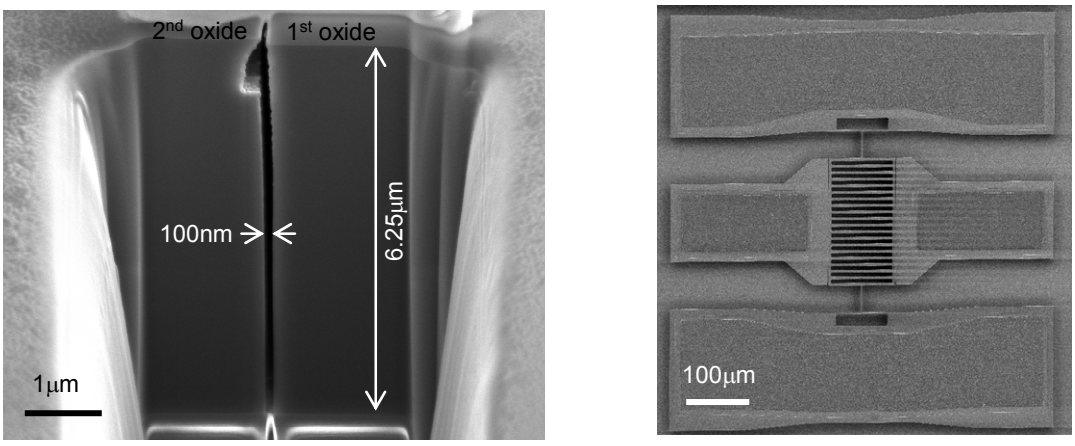

(a) (b)

Figure 3.20. (a) FIB section through a 100nm nanogap and (b) a finalized MEM resonator on 6.25μm SOI

3.9. Summary

In this chapter we have presented and discussed the nanogap technology developed by the author of the manuscript for SOI MEM resonator fabrication. The main conclusions and achievements are summarized as follows.

There is a critical need of low motional resistance for MEM resonators. The most effective ways to reduce its value are to increase the DC bias voltage or to reduce the width of the actuation gap. The second solution is of great interest because R_m scales with the fourth power of the gap, but also generates technological challenges due to the need of gap widths in the order of 100nm.

By analyzing various nanogap fabrication techniques, we have concluded that one very interesting and effective solution is the lateral spacer technique, which enables lithography constraint-free fabrication. We have presented such a technique using polysilicon as gap spacer, which resulted in single crystal silicon structures with 100nm actuation gap width.

We have reported an original process flow and detailed descriptions of every fabrication step were given. The batch-level, four-mask fabrication sequence employs only standard optical lithography with 1μm resolution and IC-compatible processing steps to obtain fully monocrystalline devices with ~100nm wide gaps. By using thinner spacer layers, the process can be scaled down to even narrower gaps, in the order of tens of nm. Additionally, an original antiskirting design technique has been proposed and validated for gap depths of up to 10μm. The full process has been successfully validated on two different SOI batches, with silicon film thicknesses of 1.5μm and 6.25μm.

With our process, aspect-ratios as high as [60:1] were demonstrated, using an optimized, notch-free dry etch based on Alcatel Vacuum Technology's SHARP. This combination of narrow and very deep transduction gaps etched in single crystalline silicon is one of the best results yet published.

3.10. Bibliography

[3.1] T. Mattila, J. Kiihamäki, T. Lamminmäki, O. Jaakkola, P. Rantakari, A. Oja, H. Seppä, H. Kattelus and I. Tittonen, “A 12 MHz Micromechanical Bulk Acoustic Mode Oscillator”, Sensors and Actuators A, volume 1, no. 1, 2002, pp.1-9

[3.2] D. Grogg, N.D. Badila Ciressan, and A.M. Ionescu, "Focussed ion beam based fabrication of micro-electro-mechanical resonators", Journal of Microsystem Technologies, volume 14, no 7, 2008, pp. 1049-1053

[3.3] C. Durand, “In-Plane Silicon-On-Nothing Nanometer-Scale Resonant Suspended Gate MOSFET for In-IC Integration Perspectives”, IEEE Electron Device Letters, volume 29, no. 5, 2008, pp. 494-496

[3.4] R. Abdolvand and F. Ayazi, "A Gap Reduction and Manufacturing Technique for Thick Oxide Mask Layers with Multiple-Size Sub-μm Openings," Journal of Microelectromechanical Systems, volume 15, issue 5, 2006, pp. 1139-1144

[3.5] E. P. Quévy, S.A. Bhave, H. Takeuchi, Tsu-Jae King, and R.T. Howe, “Poly-SiGe high frequency resonators based on lithographic definition of nano-gap lateral transducers,” 11th Solid-State Sensor, Actuator, and Microsystems Workshop, 2004, pp. 360-363.

[3.6] E. P. Quévy, A. San Paulo, E. Basol, R.T. Howe, Tsu-Jae King, and J. Bokor, “Back-End-Of-Line Poly-Sige Disk Resonators”, 19th IEEE International Conference on Micro Electro Mechanical Systems (MEMS’06), 2006, pp. 234-237

[3.7] W.-T. Hsu, J.R. Clark, and C.T.-C. Nguyen, “A sub-micron capacitive gap process for multiple-metal-electrode lateral micromechanical resonators”, 14th IEEE International Conference on Micro Electro Mechanical Systems (MEMS’01), 2001, pp. 349-352

[3.8] Y. Xie, S.-S. Li, Y.-W. Lin, Z. Ren, and C.T.-C. Nguyen, “1.52-GHz micromechanical extensional wine-glass mode ring resonators”, IEEE Transactions on Ultrasonics, Ferroelectrics and Frequency Control, volume 55, no. 4, 2008, pp. 890-907

[3.9] E. Quevy, B. Legrand, D. Collard, and L. Buchaillot, "Ultimate technology for micromachining of nanometric gap HF micromechnical resonators", 16th IEEE International Conference on Micro Electro Mechanical Systems (MEMS ’03), 2003, pp. 157-160

[3.10] S. Pourkamali, and F. Ayazi, "Fully Single Crystal Silicon Resonator with Deep-Submicron Dry-Etched Transducer Gaps," 17th IEEE International Conference on Micro Electro Mechanical Systems (MEMS ’04), 2004, pp.813-816

[3.11] http://cmi.epfl.ch

[3.12] M. Puech, N. Launay, N. Arnal, P. Godinat, and J.M. Gruffat, “A Novel Plasma Release Process and a Super High Aspect Ratio using ICP Etching for MEMS”, Proceedings SEMICON, Japan, December 2003

[3.13] J. Karttunen, J. Kiihamaki, and S. Franssila, “Loading effects in deep silicon etching”, Proceedings of SPIE 2000, volume 4174, pp. 90–97

[3.14] H. Xia, C.M.A. Ashruf, P.J. French, and J.J. Kelly, “Galvanic Cell Formation in Silicon/Metal Contacts: The Effect on Silicon Surface Morphology”, Chemistry of Materials, volume 12, issue 6, 2000, pp. 1671-1678

[3.15] W. Leitner, “Green chemistry: Designed to dissolve”, Nature, volume 405, no. 6782, 2000, pp. 129-130

Chapter 4

Characterization and Analysis

The fourth chapter presents full characterization of bulk-mode nanogap MEM resonators fabricated during this thesis work. Analysis and discussion of the results are also proposed.

Initial electrical measurements of microgap devices fabricated using a simple two-mask process show very high motional resistances in the order of MΩ and require DC biases of almost 100V. This poor performance originates in the extremely wide transduction gaps, and motivates the efforts made for creating nanogap devices.

Nanogap device characterization demonstrating the excellent resonator performance includes room temperature measurements at low pressure in linear regime, ambient pressure and DC bias influence studies, nonlinear behavior analysis at high AC powers and a novel temperature dependence study for very wide temperature range from liquid nitrogen temperature of 80K up to 320K.

4.1. Measurement Setup

Resonators have been measured inside a PMC-150 vacuum cryogenic prober using an HP8753D network analyzer without additional pre-amplification.

The setup allows manual probing of devices at low temperatures, under vacuum conditions (as high as 10^{-6}mbar), free from ice and frosting on the surface down to a temperature of 70K (temperatures as low as 20k are achievable by using liquid helium). High temperature measurements can also be performed, up to 400K. The prober is set on a vibration isolation table so that the equipment is not disturbed by any external movements. A picture of the entire setup is presented in Figure 4.1.

Figure 4.1. The measurement setup: on the left side, the HP8753D network analyzer, and in the middle and right side, the PMC-150 vacuum cryogenic prober

The DC bias voltage has been applied via the same equipment at both input and output electrodes, while the resonating structure and the bulk silicon of the SOI wafer were connected to ground, as shown in Figure 4.2. G-S-G (ground-signal-ground) on-wafer pads are used to electrically connect and test the resonator.

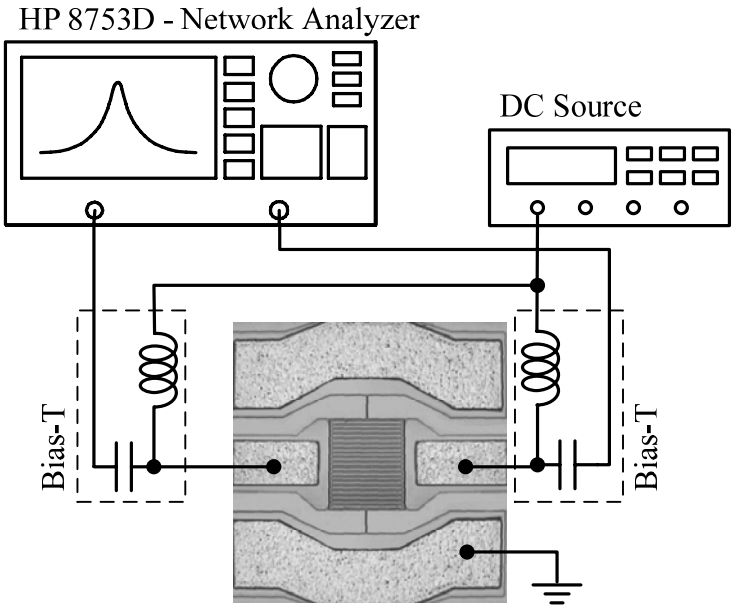

Figure 4.2. 2-port resonator measurement setup

4.2. Micro-Gap vs. Nano-Gap Resonators

An initial micro-gap technology run, meant to quickly evaluate resonator designs, as well as serve as comparison for nano-gap technology improvement, was performed at Philips Research, Eindhoven, The Netherlands.

The starting material was SOI with silicon and buried oxide layers of 20μm and 2μm thick, respectively. The resonators were patterned with only one mask, using optical lithography, and then were transferred via dry-etching into the SOI active layer. Typical gaps of 1.3μm were obtained, as shown in Figure 4.3.

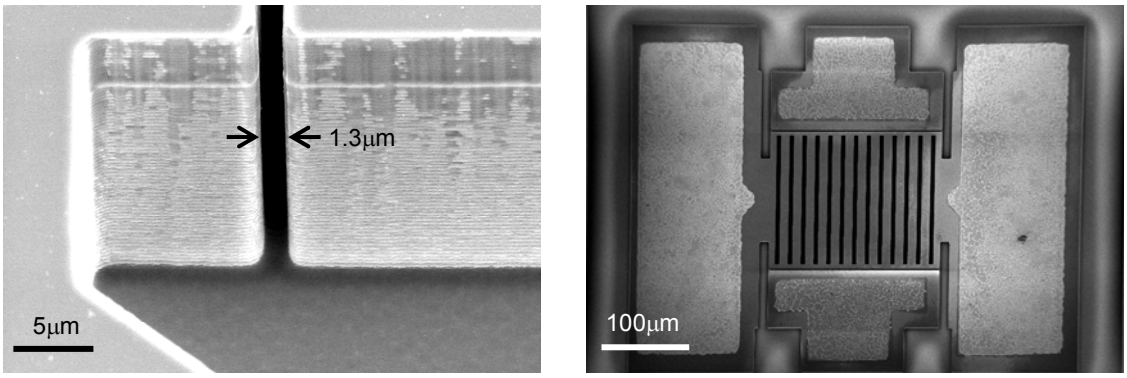

(a) (b)

Figure 4.3. (a) SEM cross-section view of 20μm deep and 1.3μm wide resonator-to-electrode gap and (b) SEM top view image of the microgap resonator

The fabricated MEM resonators have been tested at wafer-level in a vacuum chamber. Figure 4.4. reports the measured S_{21} parameter. Quality factors up to 18,000 for the first resonating bulk-mode (25.5MHz) have been experimentally derived from the transmission parameter, as the center frequency over the 3dB bandwidth, for V_{DC}=80V, at ambient pressure lower than $2*10^{-3}$mbar and RF power of -10dBm. The lower than expected quality factor value is probably due to sub-optimal anchor design, which was improved in the next fabrication run.

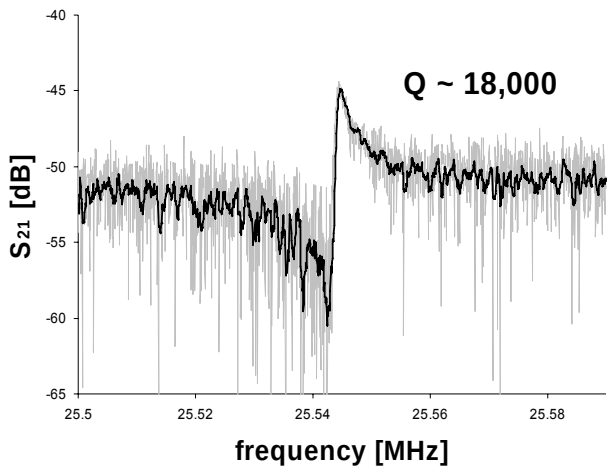

Figure 4.4. S_{21} transmission parameter for a 25.5MHz resonator at V_{DC}=80V (measured data: grey and 10-point averaged data: black);

The resonator performance has been investigated at different values of DC bias voltage. A typical drift of S_{21} transmission parameter with respect to V_{bias} is presented in Figure 4.5.

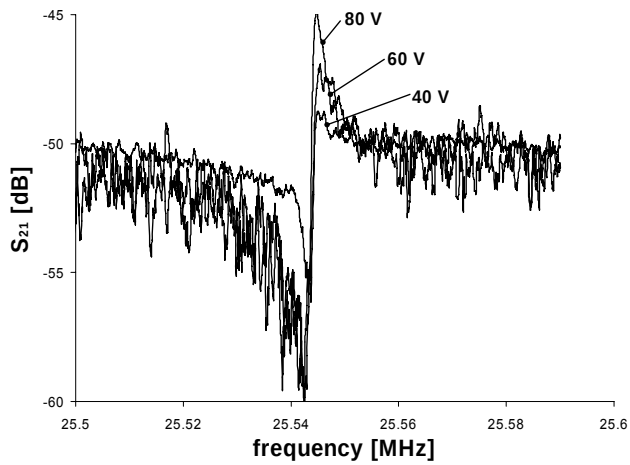

Figure 4.5. S_{21} transmission parameter dependence on applied bias voltage in vacuum

The very high bias voltages needed to operate this device (more than 60V), are a direct consequence of large, micron-sized transduction gaps. Thus, as predicted by the theory, it becomes evident that for practical applications, nanogap technology is essential.

4.3. Nanogap Resonator Typical Responses in Vacuum[1], at Room Temperature

4.3.1. Longitudinal Beam Resonators

The S_{21} transmission parameter peak at resonance presented in Figure 4.6 corresponds to a nanogap longitudinal simple beam resonator, fabricated on 6.25μm-thick silicon layer. The resonator dimensions are: length, L=360μm and width, w=10 μm. The device has a resonance frequency, f_{res}=11.5MHz, and shows an extremely high quality factor, Q=235'000. The extracted motional resistance, R_m=285kΩ. The measurement is performed at 8V DC bias and -20dBm AC power.

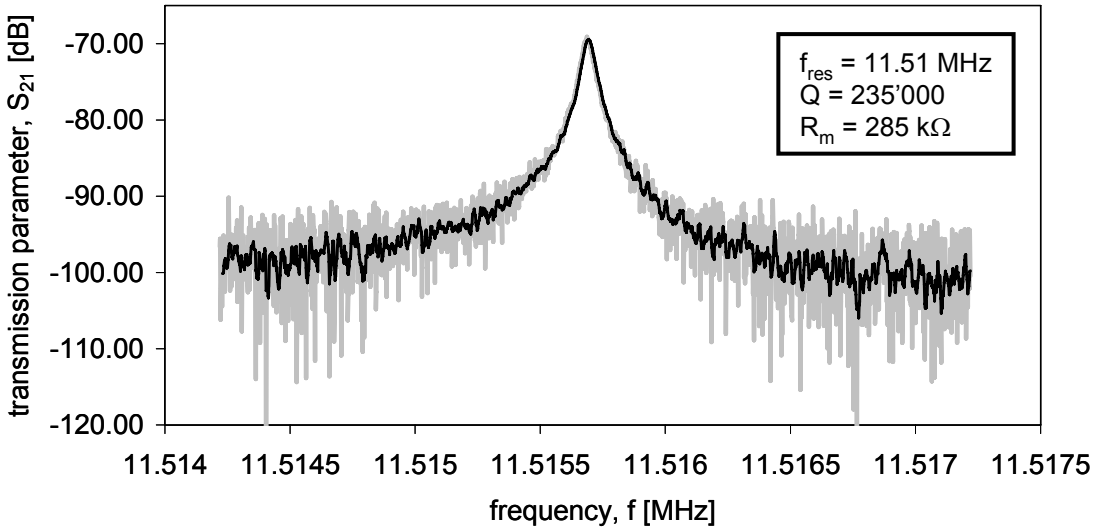

Figure 4.6. S_{21} scattering parameter for an 11.5MHz longitudinal beam at resonance

Figure 4.7 presents the S_{21} transmission parameters of two similar devices: a simple longitudinal beam and an improved beam (which has flared edges for increased electrode-to-resonator overlap, as explained in Section 2.2.1). Both designs have the same dimensions: length, L=161μm and width, w=10 μm. The lower curve corresponds to the simple beam, operating at f_{res}=26MHz. The high motional resistance extracted for this device is a consequence of the small overlap between the resonator and the electrodes. The upper curve in Figure 4.7 corresponds to the transmission parameter near resonance of the improved design. We can notice the smaller resonance frequency, due to the added mass. Both measurements are performed at the same bias voltage as the previous one (V_{DC}=8V), but at higher AC power: P_{AC}=0dBm.

[1] This section presents measurements performed in high vacuum, at pressures below 10^{-5}mbar

The improved design has almost three times lower motional resistance at the same DC bias and in the same frequency range.

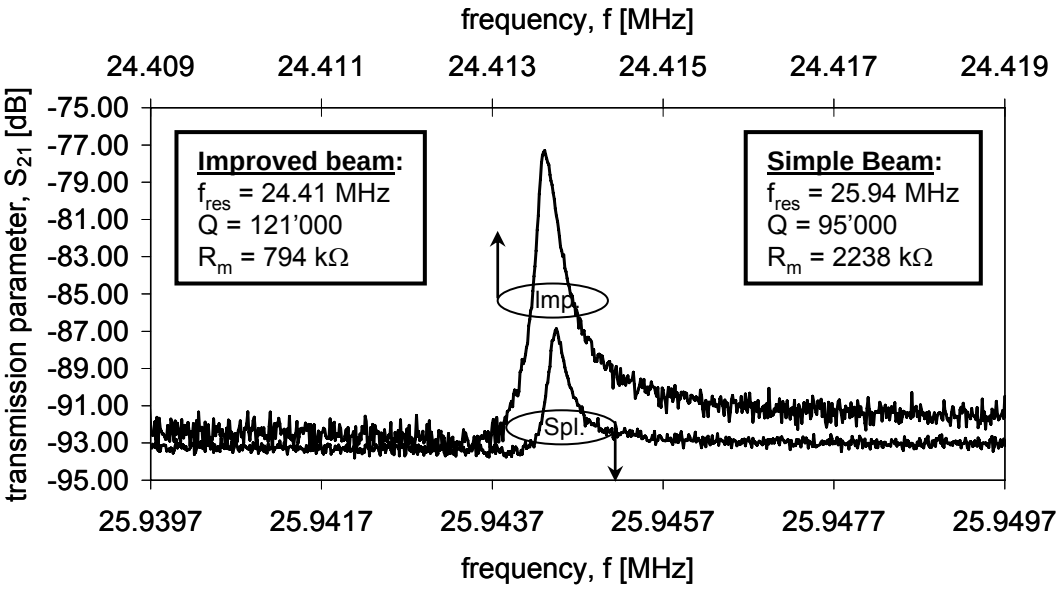

Figure 4.7. S_{21} scattering parameter for a 26MHz simple longitudinal beam at resonance is compared to the one of an "improved" beam, resonating at 24.2MHz

4.3.2. Fragmented Membrane Resonators

Figure 4.8 presents the typical peak resonance responses of the S_{21} transmission parameters for two simple-arm MEM resonators: the type-A device has a silicon thickness of 1.3μm while the type-B device has a silicon thickness of 6.25μm, as summarized in Table 2.1.

The measured resonance frequencies are 21.72MHz for the type-A and 24.46MHz for type-B, respectively. Quality factor Q=33'000 and motional resistance, R_m=582kΩ are extracted for the type-A device at 20V DC bias voltage and -25dBm AC power, and Q=67'000 and R_m=113kΩ, are extracted for the type-B device at 12V DC bias voltage and -20dBm AC power; both measurements were performed at room temperature and in vacuum (<10^{-5}mbar). These results demonstrate a quality factor increase by factor of 2 and motional resistance decrease by a factor of more than 5 (at almost half V_{DC}) that can be obtained by the use of thicker silicon layers.

Nevertheless, it is also shown that very good quality factors (>10'000) and relatively acceptable motional resistance (500kΩ at low applied voltage) can be still achieved for 1μm-thick MEM bulk resonators, with appropriate gap scaling and optimized design.

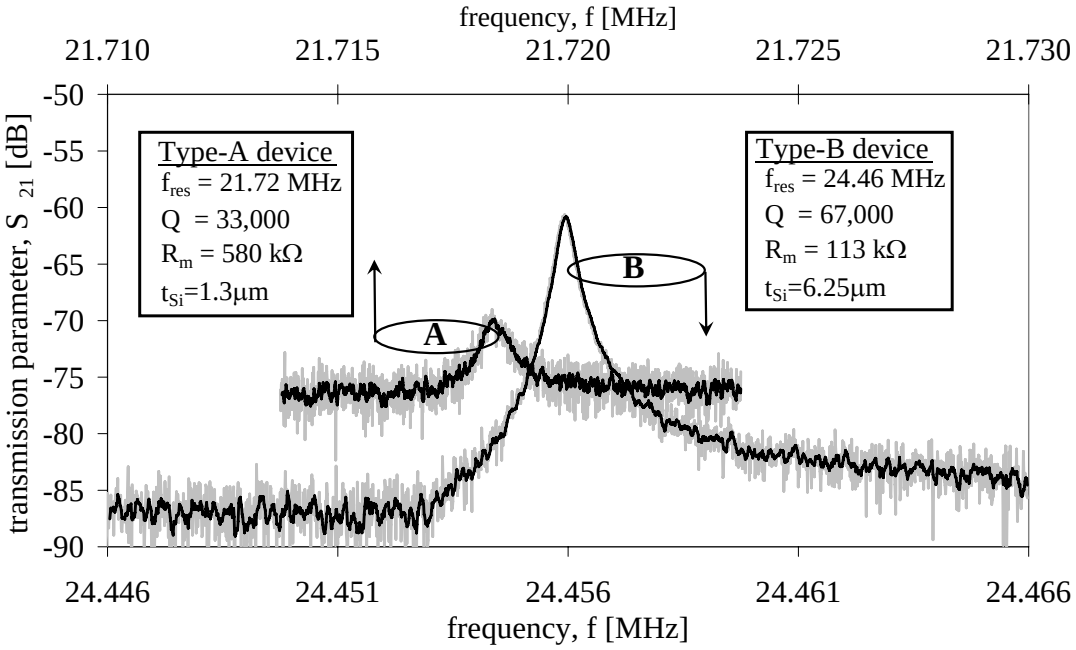

Figure 4.8. *S_{21}* scattering parameter for a simple-arm, type-B device at resonance frequency is compared to the one of a T-arm, type-B resonator

S_{21} transmission parameter peaks for simple-arm and T-arm designs of the type-B device are compared in Figure 4.9.

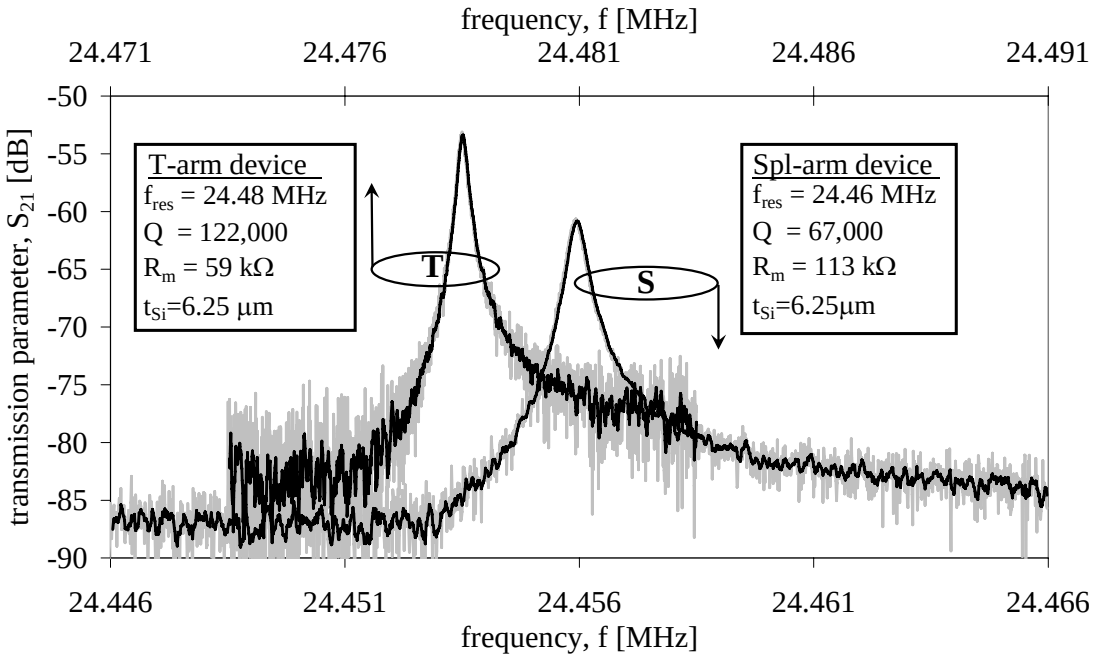

Figure 4.9. *S_{21}* scattering parameter for a simple-arm, type-B device at resonance frequency is compared to the one of a T-arm, type-B resonator

We can notice in Figure 4.9 the resonator performance improvement due to anchor-loss optimization: the T-arm resonator has a double quality factor, Q=122'000 and motional resistance decreased at half, R_m=59kΩ. The values were extracted at 12V DC bias voltage and -25dBm AC power, at room temperature and in vacuum (<10^{-5}mbar). The measured resonance frequency is f_{res}=24.48MHz for the T-arm, very slightly different than the simple-arm design value.

4.4. Small Signal Equivalent Circuit Extraction in Linear Conditions

In order to fully characterize the MEM resonator, all its electrical and mechanical parameters need to be determined. The procedure for this is described below.

4.4.1. Lumped Element Extraction Procedure [4.1]

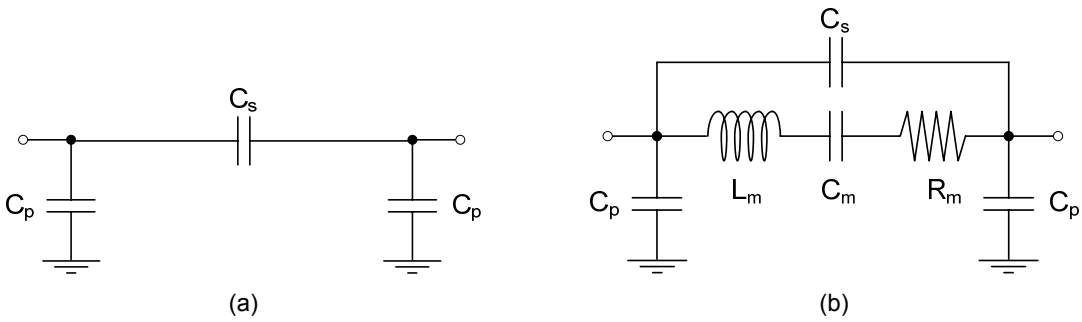

Figure 4.10. (a) Equivalent resonator circuit when the bias voltage is removed (V_{DC}=0V) and (b) Equivalent resonator circuit with bias voltage (V_{DC}>0V)

The circuits in Figure 4.10 describe the resonator electrical behavior when the DC bias is removed (Figure 4.10.a) and when a non-zero bias voltage is applied (Figure 4.10.b). The electrical quality factor of the parasitics are very small compared to the resonator, thus their frequency dependence can be neglected.

The circuits presented in Figure 4.10 can be simplified by expressing them by a combination of complex admittances, as shown in Figure 4.11.

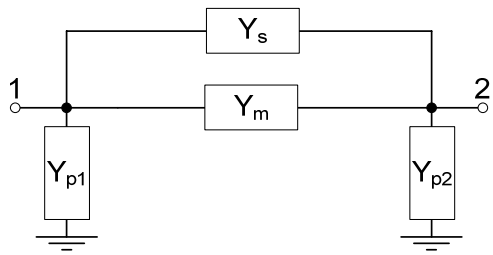

Figure 4.11. Equivalent resonator circuit expressed in terms of complex impedances

The complex impedances are given by:

$$
\begin{aligned}
Y_s &= j\omega C_0 \\
Y_{p1} &= j\omega C_{p1} \\
Y_{p2} &= j\omega C_{p2} \\
Y_m &= \frac{1}{R_m + \frac{1}{j\omega C_m} + j\omega L_m}
\end{aligned}
\tag{4.1}
$$

When $V_{DC}=0$, the impedance describing the intrinsic resonator, Y_m, disappears. Thus, the Y-parameters of the network, are:

$$
\begin{aligned}
Y_{11} &= \left.\frac{I_1}{V_1}\right|_{V_2=0} = Y_{p1} + \left(Y_m + Y_0\right) \\
Y_{22} &= \left.\frac{I_2}{V_2}\right|_{V_1=0} = Y_{p2} + \left(Y_m + Y_0\right) \\
Y_{21} &= \left.\frac{I_2}{V_1}\right|_{V_2=0} = \left.\frac{I_1}{V_2}\right|_{V_1=0} = Y_{12} = -\left(Y_m + Y_s\right)
\end{aligned}
\tag{4.2}
$$

Thus, the complex admittances Y_s, Y_{p1}, Y_{p2} and Y_m of the circuit can be calculated as:

$$
\begin{aligned}
Y_{p1} &= Y_{11} + Y_{21} \\
Y_{p2} &= Y_{22} + Y_{21} \\
Y_s &= -Y_{21}\big|_{V_{DC}=0} \\
Y_m &= Y_{21}\big|_{V_{DC}>0} - Y_{21}\big|_{V_{DC}=0}
\end{aligned}
\tag{4.3}
$$

The Y-parameters can be calculated from the 2 port scattering parameters of the MEM resonator as expressed below, where Y_c is the characteristic admittance given by $Y_c=1/Z_c=1/50\Omega^{1}$

$$
\begin{aligned}
D &= (1+S_{11})(1+S_{22}) - S_{21}S_{12} \\
Y_{11} &= Y_c \frac{\left[(1-S_{11})(1+S_{22}) + S_{21}S_{12}\right]}{D} \\
Y_{12} &= \frac{-2Y_c S_{12}}{D} \\
Y_{21} &= \frac{-2Y_c S_{21}}{D} \\
Y_{22} &= Y_c \frac{\left[(1+S_{11})(1-S_{22}) + S_{21}S_{12}\right]}{D}
\end{aligned}
\tag{4.4}
$$

Using Equations (4.3) and (4.4), it is straightforward to determine C_0, C_{p1} and C_{p2}. In order to get R_m, C_m and L_m, a frequency dependent fit of the Y_m data has to be performed. First, a fit of the phase angle, θ, is made for determining the quality factor and for getting a first approximation of the frequency, ω_0, and then a second fit of Y_{mag}, the magnitude of Y_m, gives the value for A and refines the result for ω_0:

$$
\begin{aligned}
\theta &= ArcTan\left[\frac{Im\{Y_m\}}{Re\{Y_m\}}\right] = ArcTan\left[Q\frac{\omega_0^2 - \omega^2}{\omega_0 \omega}\right] \\
Y_{mag} &= 20 \cdot Log|Y_m| = 10 \cdot Log\left[\frac{A^2}{\left(\omega_0^2 - \omega^2\right)^2 + \left(\omega\omega_0 / Q\right)^2}\right]
\end{aligned}
\tag{4.5}
$$

From the fitted values of Q, A and ω_0, the equivalent electrical circuit parameters, R_m, C_m and L_m and the mechanical parameters k, m and γ can be obtained as:

$$
\begin{aligned}
Y_m &= \frac{1}{R_m + \frac{1}{j\omega C_m} + j\omega L_m} = \frac{A}{\omega_0^2 - \omega^2 + \frac{j\omega\omega_0}{Q}} = \frac{\frac{j\omega\eta^2}{m}}{\frac{k}{m} - \omega^2 + \frac{j\omega\gamma}{m}} \\
\omega_0^2 &= \frac{1}{L_m C_m} = \frac{k}{m} \\
Q &= \frac{\omega_0 L_m}{R_m} = \frac{1}{\omega_0 R_m C_m} = \frac{\sqrt{km}}{\gamma} \\
A &= \frac{j\omega}{L_m} = \frac{j\omega\eta^2}{m}
\end{aligned}
\tag{4.6}
$$

4.4.2. Extracted Fragmented Membrane Resonator Parameters

Table 4.1 fully summarizes type-A and type-B resonator parameters, obtained with the extraction procedure described in the previous section for resonators measured in vacuum (<10^{-5}mbar) at room temperature:

Table 4.1. Experimental Electrical Parameters For The Fabricated SOI MEM Bulk Lateral resonators.

Resonator type	A, Simple-arm	B, Simple-arm	B, T-arm
V_{bias} [V], *DC* bias voltage	20	12	12
P_{AC} [dBm], *AC* signal power	-25	-20	-25
f_{res} [MHz], resonance frequency	21.72	24.46	24.48
Q, quality factor	32'802	67'000	122'000
R_m [kΩ], motional resistance	582	113	59
L_m [H], motional inductance	140.0	49	46.8
C_m [aF], motional capacitance	0.384	0.865	0.903
C_s [fF], feed-through capacitance	25.90	107.91	107.9
C_{p1} [fF], pad capacitance	735	392	448
C_{p2} [fF], pad capacitance	744	373	345

4.5. Ambient Pressure Influence on Fragmented Membrane BLR Performance

The electrical characterization of the resonator performance as a function of the pressure inside the vacuum chamber is presented in Figure 4.12. Due to damping, the quality factor degrades from 126'000 in vacuum (<10^{-5}mbar) down to 3'600 in air, which is still quite promising compared to the similar *Q* degradation for flexural mode resonators (down to few tens - hundreds [4.2]). The resonance frequency shift is rather small, increasing with 0.01% in air, compared to the vacuum conditions.

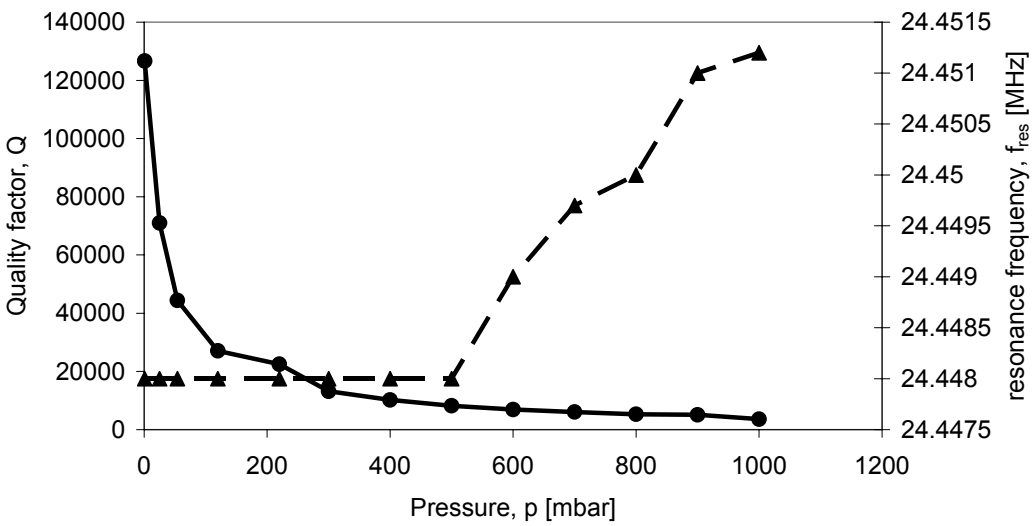

Figure 4.12. Fragmented-membrane resonator performance, *Q* and f_{res}, measured as a function of pressure

Figure 4.13 presents the S_{21} peak measured in air at 8V of DC bias voltage and 0dBm AC power. The resonance frequency is f_{res}=24.4512MHz.

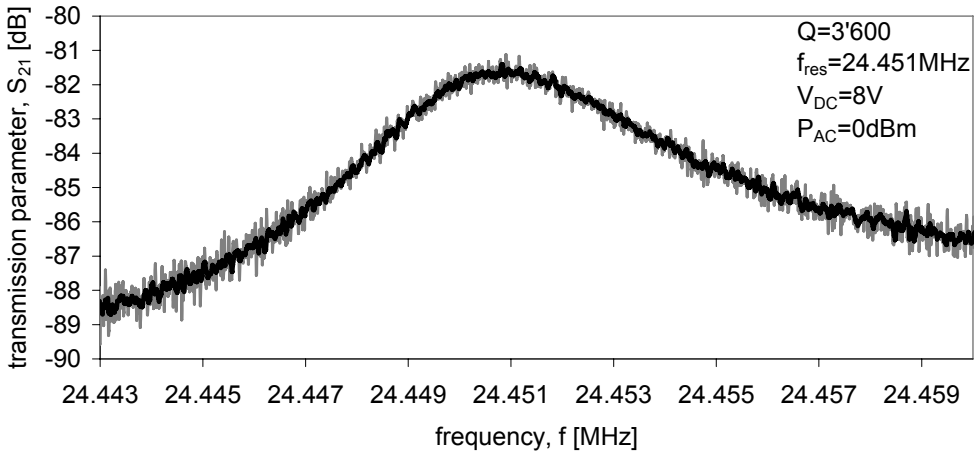

Figure 4.13. S_{21} peak of a fragmented-membrane resonator, measured in air

4.6. DC Bias Influence on Fragmented Membrane Resonator Performance

While the DC bias voltage has relatively little influence on the quality factor (less than 10-15% experimental variation), it is confirmed that it has a significant impact on the resonance frequency and on the motional resistance of BLR with fragmented electrodes.

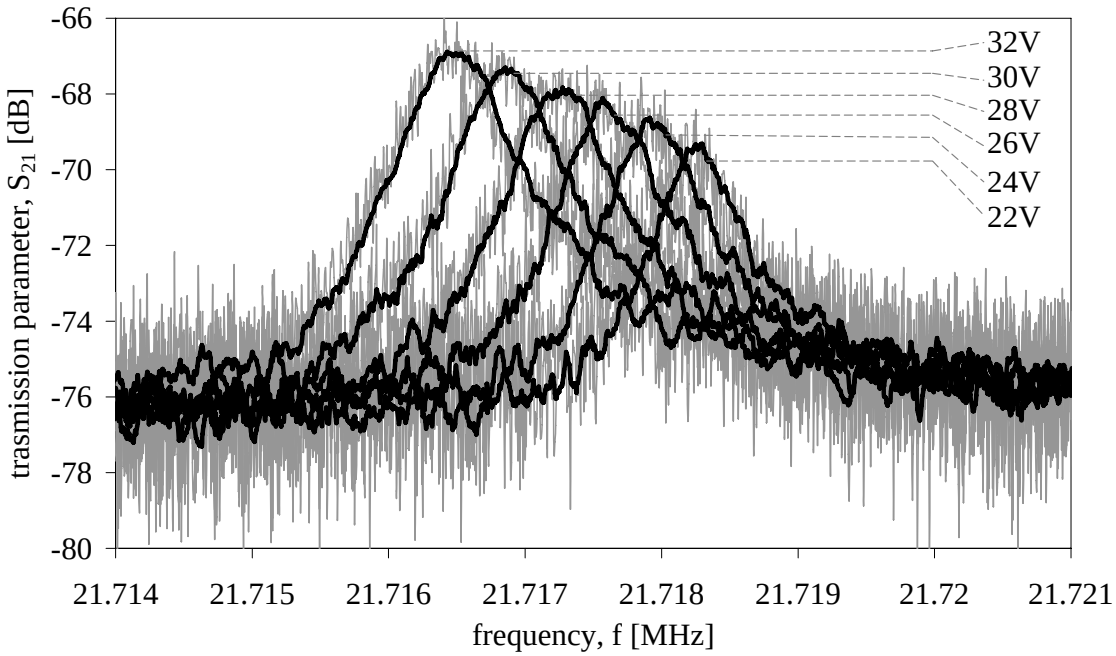

Figure 4.14. Type-A, simple-arm resonator transmission parameter S_{21} response with varying bias voltages and AC power set at -25 dBm.

Figure 4.14 shows the resonance frequency drift due to spring softening, for a type-A, simple-arm resonator, measured in vacuum: when increasing the DC bias, the resonance peaks become higher, narrower and their resonance frequency decreases.

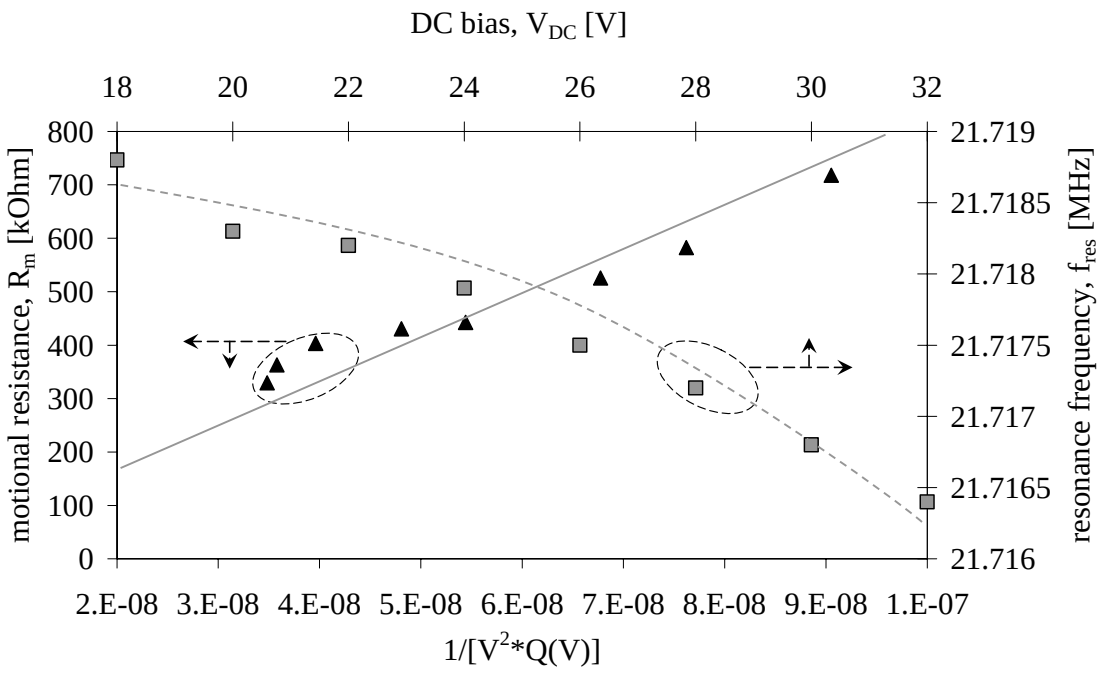

Figure 4.15. (a) Resonance frequency dependence on DC bias voltage and (b) motional resistance dependence on $1/V^2 \cdot Q(V)$ for a type-A, simple-arm device

Figure 4.15 confirms two key dependencies for the same device:

(i) the quadratic dependence of the resonance frequency with DC bias, according to [4.3]:

$$\omega_{res}^2 = \frac{k_{eff} - k_{el}}{m_{eff}} = \frac{k_{eff}}{m_{eff}} - \frac{\varepsilon A V_{DC}^2}{m g^2} \qquad (4.7)$$

where k_{el} is the bias voltage-dependent electrical spring constant, that subtracts from the mechanical spring constant, k_{eff}, lowering the overall spring stiffness (and thus the resonance frequency of the resonator).

(ii) the linear dependence of the motional resistance, R_m, with $1/V^2 \cdot Q(V)$ as predicted by Equation (2.16) (for the precision of the extraction, Q is extracted at each DC bias)**.** It is worth noting that the motional resistance can be greatly decreased from 720kΩ to nearly 300kΩ by increasing V_{DC} from 18V to 32V.

4.7. Nonlinear Effects

Linear behavior of the resonator is a key concern for granting both optimal energy transmission to the resonator and for obtaining non-distorted signal and hence lower phase-noise in an oscillator.

4.7.1. Simple Longitudinal Beam Resonator

Electrical nonlinearities were observed when applying a large AC signal of more than 5dBm. Figure 4.16 presents the nonlinear response of a longitudinal beam resonator for two different DC biases, measured in vacuum: $V_{DC1}=8V$ and $V_{DC2}=10V$. In both cases, the AC power has been increased from 5dBm (where linear behavior is granted) to 14dBm (strong nonlinearity). This resonator response is inline with the nonlinearity theory presented in Section 2.1.3.

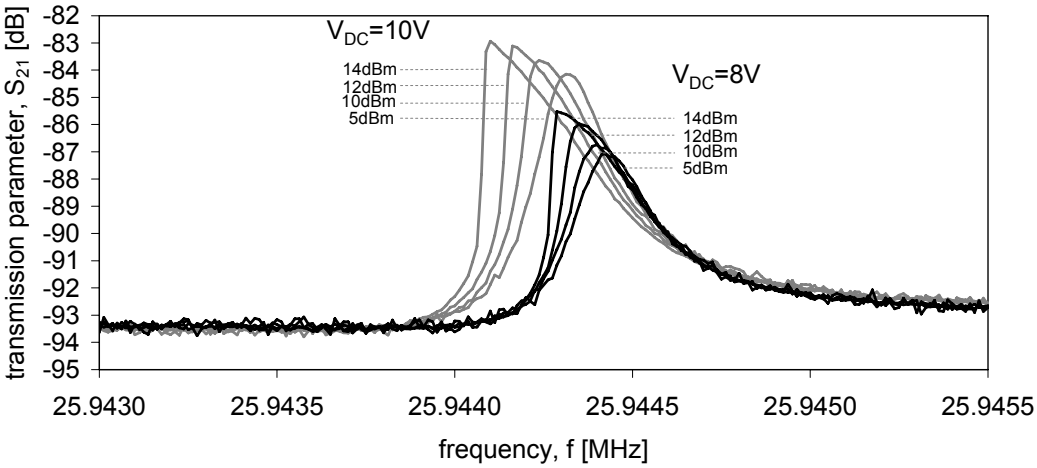

Figure 4.16. Nonlinearity effects in a longitudinal beam resonator, which appear when increasing the AC input power from 5dBm to 14dBm, for two different DC biases: 8V and 10V

The model presented in Section 2.1.3 can be used to predict the maximum vibration amplitude, above which nonlinearities occur. Starting from Equations (2.10 – 2.11), and knowing that $\dot{x} = \omega_0 x$ [4.4], the displacement amplitude can be calculated as:

$$x = \frac{ig^2}{V_{DC}\varepsilon_0 wh\omega_0} \quad (4.8)$$

For the simple longitudinal beam resonator, the A-f model predicts a critical current of 1.16μA, resulting in a critical displacement amplitude of 15.4nm at V_{DC}=8V.

In order to compare this value with the measurement data, we have calculated the experimental current using the measurement setup at resonance, shown in Figure 4.17.

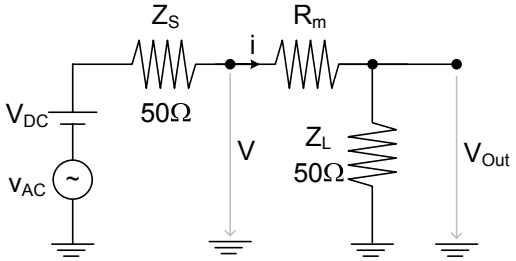

Figure 4.17. Measurement setup at resonance

According to this figure, the current can be calculated as:

$$i \approx \frac{V_{AC}}{R_m + Z_S + Z_L} \quad (4.9)$$

where the effective AC voltage at the generator is:

$$V_{ac} = 2\sqrt{Z_S P_{ac}(W)} \quad (4.10)$$

and the motional resistance, R_m, is calculated as:

$$S_{21}(mag) = 10^{\frac{S_{21}(dB)}{20}} = \frac{V_{Out}^2}{V^2} = \frac{Z_L^2}{(Z_L + R_m)^2}$$

$$\Downarrow$$

$$R_m = 2\left(\frac{Z_L}{10^{\frac{S_{21}}{20}}} - Z_L\right) \quad (4.11)$$

From the measurement data plotted in Figure 4.16, the resonator becomes nonlinear at 5dBm when 8V of DC bias are applied, which gives a critical current value of 0.35μA. The critical experimental amplitude is thus of 4.8nm. This result is about 3 times lower than the model prediction. Further work is needed in order to understand this mismatch.

4.7.2. Fragmented Membrane Resonator

Figure 4.18 shows the peak shape degradation of a type-A, simple-arm resonator, with respect to the AC injected power, measured in vacuum: below -25dBm, the curves are superposed, while at -20dBm a slight deviation appears, and finally, at -15dBm, the behavior becomes completely nonlinear.

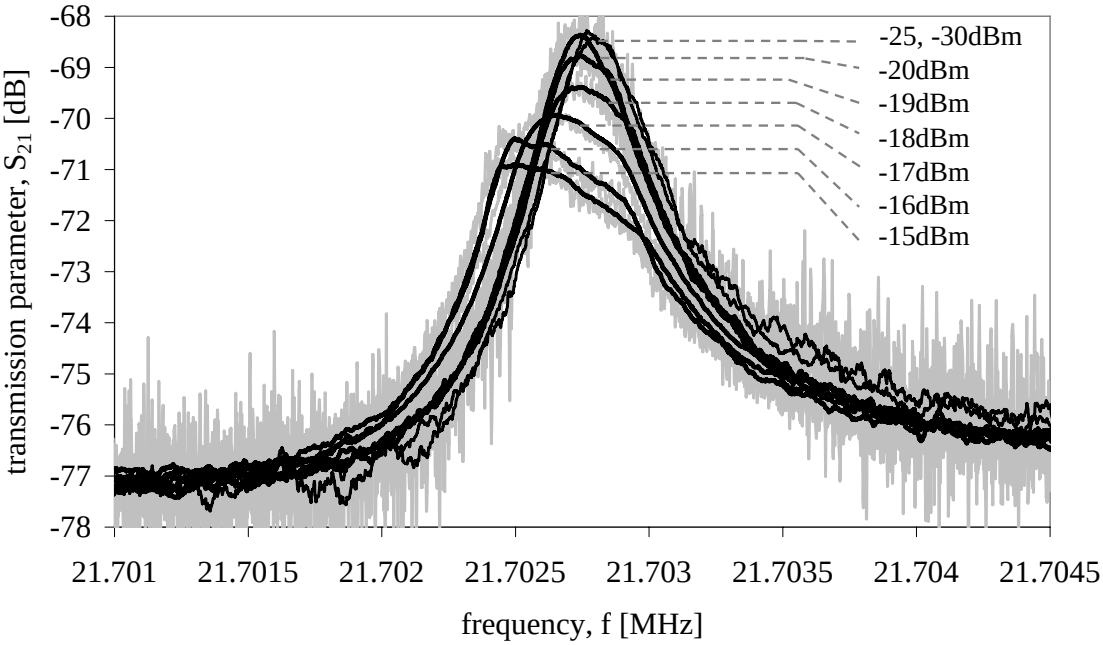

Figure 4.18. Nonlinearity effects appearing when increasing AC input power from -15dBm to -30dBm on a type-A, simple-arm resonator. Biasing voltage is 20V

In a similar way, in Figure 4.19, we can see the peak shape degradation of a type-B, T-arm resonator, with respect to the AC injected power, at V_{DC}=6V. Nonlinearities appear beyond -2dBm. The thicker device has an improved drive level, as predicted by Equations (2.18 - 2.20), due to the increased *w*h* product.

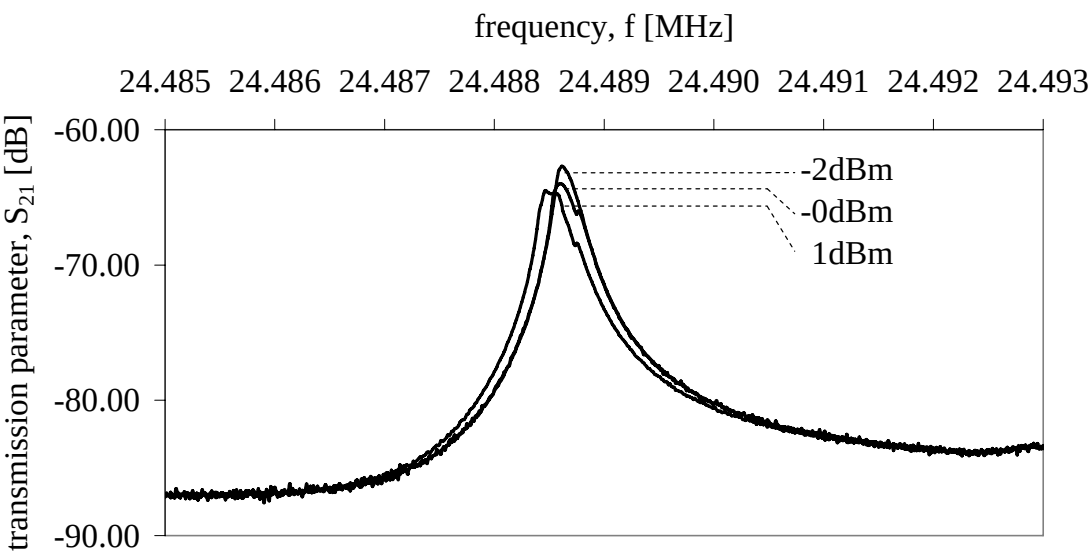

Figure 4.19. Nonlinearity effects for a type-B, T-arm resonator, at different AC powers, with biasing voltage of 6V

4.8. Temperature Influence on Fragmented Membrane Resonator

The temperature drift of MEM resonator characteristics is of critical importance for the future device success in circuit applications. The resonance frequency dependence on temperature is investigated here from 80K to 320K in vacum, for a type-B, T-arm MEM resonator, and is presented in Figure 4.20.

At temperatures beyond 160K, the measured resonance frequency values are in good agreement with the ones calculated with Equation (4.12). Thus, the temperature dependence is mainly controlled by Young's modulus variation, which follows Wachtman's law [4.5] as follows:

$$E = E_0 - BTe^{-\frac{T_0}{T}} \qquad (4.12)$$

The parameter values corresponding to the reported fit, E_0=164.4GPa (Young's modulus at 0K), B=12.5MPa/K and T_0=317K (high temperature limit beyond which Young's modulus dependence becomes linear), are in good agreement with published data [4.6, 4.7].

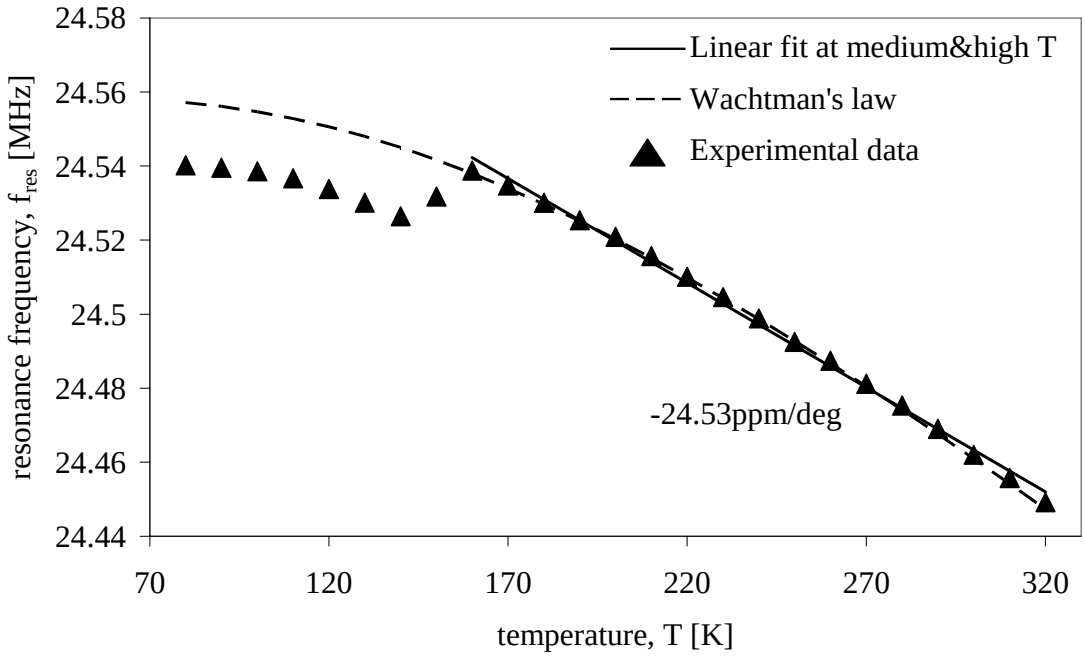

Figure 4.20. Resonance frequency dependence on temperature for T-arm, type-B resonator, between 80K and 320K. The triangles correspond to experimental data; the dotted line corresponds to Wachtman's equation and the black line is a linear fit through the values at medium and high temperature.

At high temperatures, as T approaches T_0, Young's modulus variation becomes quasi-linear, with a drift of -46ppm/K [4.8]. From Equation (2.27), we calculate:

$$f(T) \cong \frac{1}{2L}\sqrt{\frac{E(T_0)+\alpha_E(T-T_0)}{\rho}} \cong f(T_0)\left[1+\frac{\alpha_E}{2}(T-T_0)\right] \quad (4.13)$$

Based on our data, a linear approximation of $f_{res}(T)$ in the 170K÷320K range has a slope of -24.5ppm/K (black line in Figure 4.20) which is in good agreement with Equation (4.13).

Between 140K and 160K, the frequency dependence on temperature has an inversed trend, probably due to the phase change of an unknown material inside the vacuum chamber. The shift has been noticed on all measured structures, independently of the resonance frequency. At temperatures below 140K, the resonance frequency variation resumes the trend described by Wachtman's law, with slightly lower values (compared to the extracted model) probably due to added mass.

The quality factor dependence on temperature is plotted in Figure 4.21. At room temperature, the resonator shows a Q of around 120'000. Quality factor values slowly fall while decreasing the temperature and reach a minimum around 220K. Below this value, Q sharply rises reaching 200'000 at 80K. The large spread of experimental Q data, especially for the very high values, is due to the measurement precision, i.e. frequency steps are becoming comparable with the 3dB bandwidth, resulting in a relative error of 33%. Similar Q-T curves have been previously observed in other works, such as [4.9, 4.10], on flexural and torsional resonators. It has been suggested that two main mechanisms could be responsible for such behavior: (1) internal friction losses and (2) surface or near surface related phenomena. Silicon internal friction has been reported to present a maximum sharp peak (and hence a Q factor minimum) in the temperature range 115-124K.
The thermally activated internal loss mechanisms are governed by Debye's relaxation equation [4.11]:

$$\frac{1}{Q_{defects}} = \Delta\frac{f_{res}}{1+(f_{res}\tau)^2} \quad (4.14)$$

$$\tau = \tau_0 \cdot exp\left[\frac{E}{k_B T}\right] \quad (4.15)$$

where Δ is the relaxation strength, τ is the relaxation time, E and τ_0 are defect activation energy and time constant, k_B is Boltzmann's constant, T is the temperature and f_{res} is the resonance frequency.

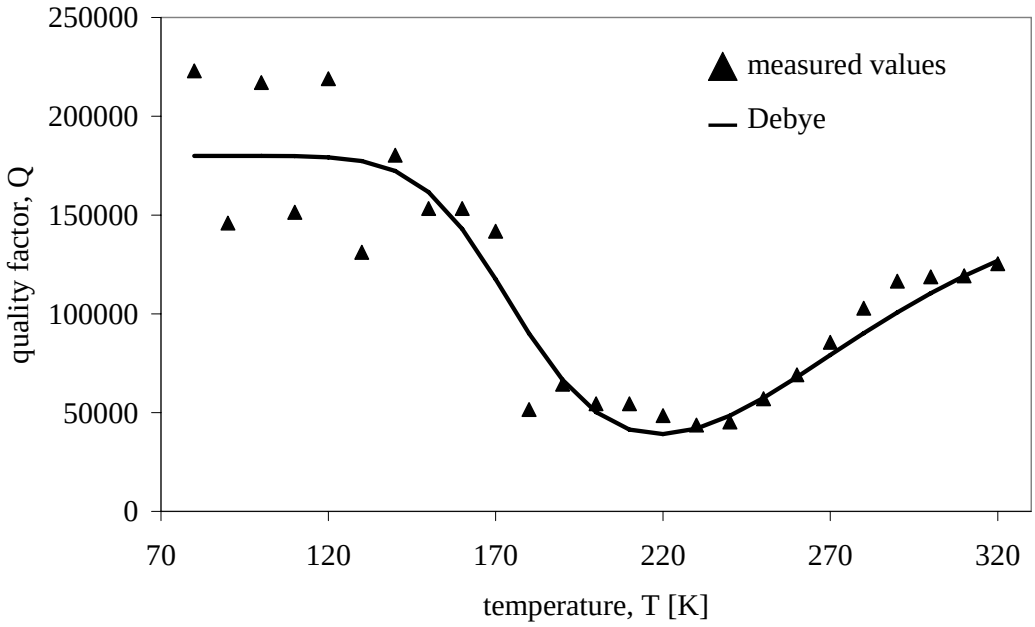

Figure 4.21. Quality factor versus temperature for type-B resonator: measured values (triangles) and Debye's analytical model.

In order to fit this trend to our experimental data, we have considered that the internal friction effect dominates at medium temperature, while at low and high temperature other types of loss mechanisms limit the resonator quality factor. Thus, Q is calculated as:

$$\frac{1}{Q} = \frac{1}{Q_{defects}} + \frac{1}{Q_{other}} \qquad (4.16)$$

Figure 4.21 shows good agreement between the experimentally determined quality factor, $Q(T)$ at different temperatures and Debye's relaxation Equation (4.18), for the fitting parameters given in Table 4.2, which are consistent with other published values.

Table 4.2. Debye's relaxation equation parameters.

Parameter	Value
τ_0 [s], defect activation time constant	$0.8*10^{-12}$
E_a [eV], defect activation energy	0.17
Δ, relaxation strength	$4*10^{-5}$
Q_{other}, quality factor due to other losses	180'000

Figure 4.22 presents the S_{21} peak, measured at 80K temperature, showing an extracted quality factor, Q>200'000 and a motional resistance R_m=42kΩ for f_{res}=24.54MHz. The measurement was performed at V_{DC}=12V and P_{AC}=-20dBm.

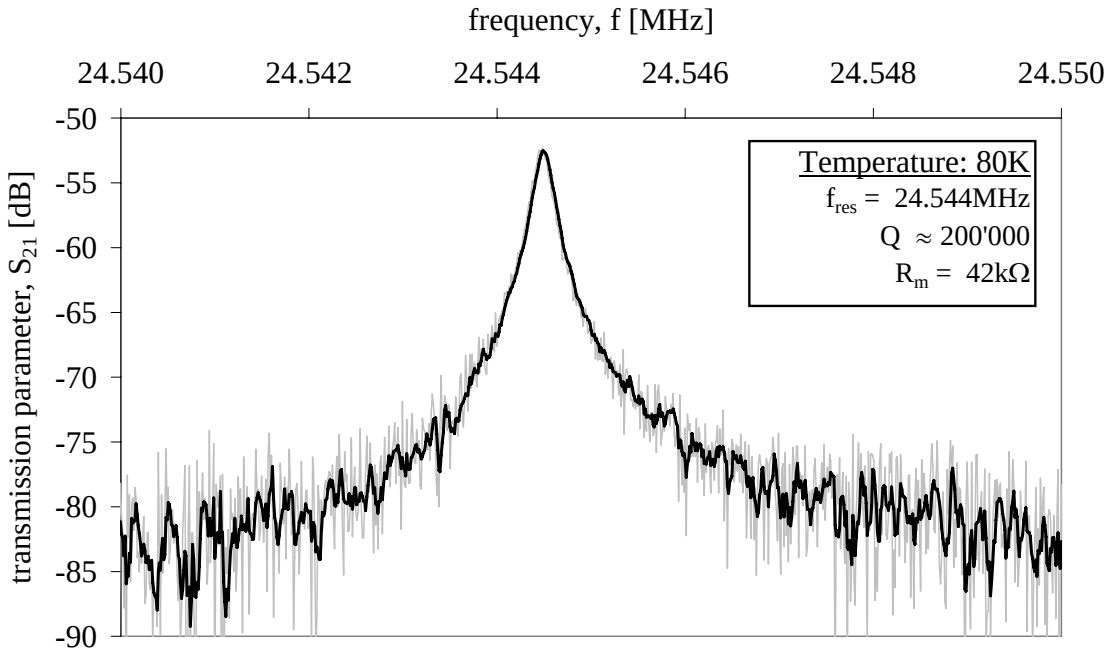

Figure 4.22. S_{21} parameter at resonance frequency of a type-B device, measured at a temperature of 80K with bias voltage of 12V and AC-signal of -20dBm.

4.9. Summary

This chapter has presented the characterization and analysis of two bulk-mode MEM resonator types: longitudinal beam resonators and original fragmented membrane resonators.

Initial fabrication run was performed with a basic process able to provide 1.3μm-wide transduction gaps, and characterization of the devices has shown very large motional resistance values, as well as the need of DC bias voltages in the range of almost 100 volts. As expected, this result is mainly due to the very wide gaps; much better results were obtained on nanogap devices fabricated using an original process based on sacrificial layer technique.

Nanogap resonator characterization at room temperature (typical peaks and full parameter extraction on calibrated measurements) reveals excellent resonator performance. Quality factors as high as 235'000 have been observed for the beam resonators, and motional resistances as low as 59kΩ have been extracted for fragmented-membranes. Figure 4.23 includes the resonators fabricated and characterized during this thesis work on the same chart presented in Figure 1.11, which compares different state of the art bulk and flexural resonators. Our results are amongst the best reported, in the tens of MHz frequency range.

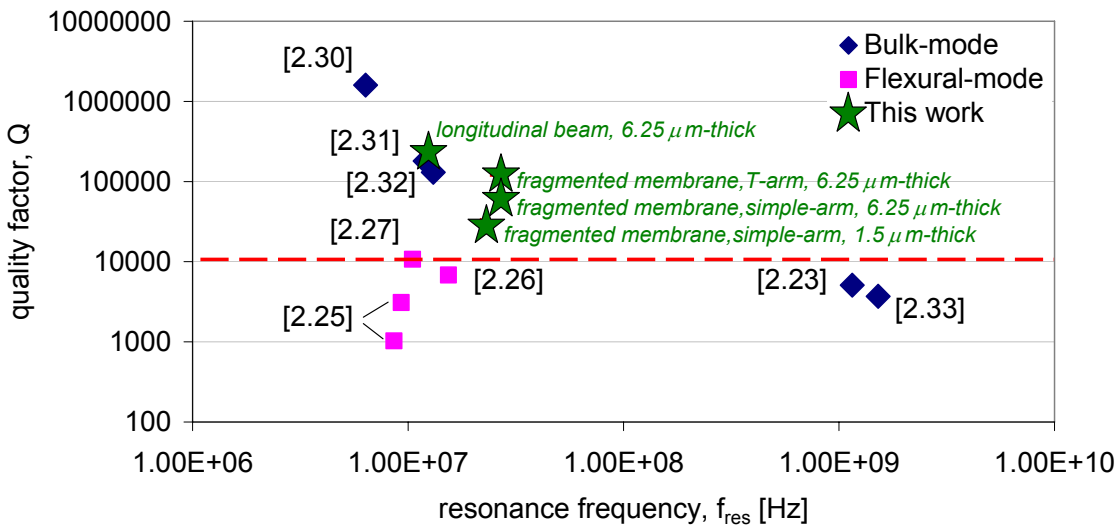

Figure 4.23. Quality factor versus frequency for different reported bulk and flexural mode resonators, compared to the bulk-mode resonators fabricated and characterized in this work

We have studied the effectiveness of several design and technology optimizations introduced in Chapter 2:

- The original longitudinal beam design improvement by widening sides proved effective in lowering the motional resistance by a factor of three;

- Transferring the nano-gap technology from 1.5μm SOI on 6.25μm resulted in devices with double quality factors and 5 times lower motional resistances;
- T-arm designs significantly reduce the acoustic losses, thus the devices showed an increase in quality factor and a decrease in motional resistance by a factor of two, compared to simple-armed resonators.

As expected, due to air damping, the fragmented-membrane quality factor degrades from 120'000 down to 3'600 at atmospheric pressure. However, this value is comparable with state of the art results, and opens the possibility for atmospheric pressure applications such as mass-detection for gas sensing applications.

The DC bias influence on resonator performance was also discussed, confirming theoretical bias dependence of the motional resistance and the frequency shift due to spring softening effect. In addition, the nonlinear resonator response was observed at high AC signal powers, and experimental nonlinearity limits were established for both type resonators. This behavior should be avoided for granting optimal energy transmission and for obtaining non-distorted signals, hence low phase-noise in oscillator applications.

Finally, a novel study on temperature dependence of the fragmented membrane resonators was presented and discussed between 80K and 320K. Two key aspects are shown: (1) the resonance frequency trend follows Wachtman's law for the whole temperature range and (2) the quality factor dependence on temperature, probably due to internal losses, follows Debye's relaxation equation. Inline with this trend, significant Q increase and R_m reduction are reported at cryogenic temperatures.

4.10. Bibliography

[4.1] Deliverable D5.1, IST-2003-507914 NanoTIMER, January 2006

[4.2] J.-F. Gong, Z.Y. Xiao, and P.C.H. Chan, “Integration of an RF MEMS resonator with a bulk CMOS process using a low-temperature and dry-release fabrication method”, Journal of Micromechanics and Microengineering, volume 17, 2007, pp. 20–25

[4.3] F. D. Bannon, J.R. Clark, and C.T.-C. Nguyen, “High Q HF Microelectromechanical filters”, IEEE Journal of Solid-State Circuits, volume 35, no. 4, 2000, pp. 512-526

[4.4] Y.-W. Lin, S. Lee, S.-S. Li, Y. Xie, Z. Ren, and C.T.-C. Nguyen, “Series-Resonant VHF Micromechanical Resonator Reference Oscillators”, IEEE Journal of Solid-State Circuits, volume 39, no. 12, 2004, pp. 2477-2491

[4.5] J. B. Jr Wachtman, W.E. Tefft, D.G. Lam, and C.S. Apstein, “Exponential Temperature Dependence of Young’s Modulus for Several Oxides”, Physical Review, volume 122, issue 6, 1961, pp. 1754-1759

[4.6] U. Gysin, S. Rast, P. Ruff, E. Meyer, D.W. Lee, P. Vettiger, and C. Gerber, “Temperature dependence of the force sensitivity of silicon cantilevers”, Physical Review B, volume 69, issue 4, 2004, id. 045403

[4.7] S. Reid, G. Cagnoli, D.R.M. Crooks, J. Hough, P. Murray, S. Rowan, M.M. Fejer, R. Route, and S. Zappe“, Mechanical Dissipation in Silicon Flexures”, Physics Letters A, volume 351, issue 4-5, 2006 pp. 205-211

[4.8] W.-T. Hsu, J.R. Clark, and C.T.-C. Nguyen, “Mechanically temperature-compensated flexural-mode micromechanical resonators”, IEEE International Electron Devices Meeting (IEDM ‘00), 2000, pp. 399-402

[4.9] K.Y. Yasumura, T.D. Stowe, E.M. Chow, T. Pfafman, T.W. Kenny, B.C. Stipe, and D. Rugar, “Quality factors in micron- and submicron-thick cantilevers”, Journal of Microelectromechanical Systems, volume 9, 2000, pp.117-125

[4.10] A. Olkhovets, S. Evoy, D.W. Carr, J.M. Parpia, and H.G. Craighead, “Actuation and internal friction of torsional nanomechanical silicon resonators”, Journal of Vacuum Science & Technology B: Microelectronics and Nanometer Structures, volume 18, issue 6, 2000, pp. 3549-3551

[4.11] A.S. Nowick, and B.S. Berry, “Anelastic Relaxation in Crystalline Solids”, Academic Press, New York, 1972

Chapter 5

MEM resonator applications

This last chapter investigates the main MEM resonator applications. Promised miniaturization and MEMS-IC integration are main drivers for MEM-based oscillators and filters, which could in the future replace conventional circuits based on discrete components. Additionally to the MEM-based oscillator state-of-the-art overview, we have presented a simulation which demonstrates the possibility of using our original fragmented membrane bulk lateral resonator as frequency selective component in a Pierce oscillator, with very good performance, which nearly meets the GSM specifications.

The third application discussed in this chapter is in the field of mass sensing. MEM resonator-based sensors show extremely good sensitivities; when scaled into NEM resonators, they can enable detection of masses as small as 10s of zeptograms (10^{-21}g). Theoretical evaluation of the MEM resonators fabricated in this work for mass detection application is also shown.

5.1. Oscillators

In any electronic product, a clock gives the heartbeats. Almost all analog or digital electronic systems, starting from radios and televisions to computers and communication or navigation systems, rely on oscillators for time keeping and frequency reference. The oscillators provide periodic output signals with precisely-defined frequency. They are based on a loop integrating a resonating element as frequency selective component with a sustaining amplifier, and a buffer amplifier which outputs the signal to the outside world (Figure 5.1). At turn on, the oscillator starts amplifying the noise in the circuit and positively feeds it to the resonator, which inputs it back to the amplifier and so on, until stable oscillations are reached, with the condition that both gain and phase conditions are met (loop gain magnitude equals unity and phase shift is either 0° or 360°).

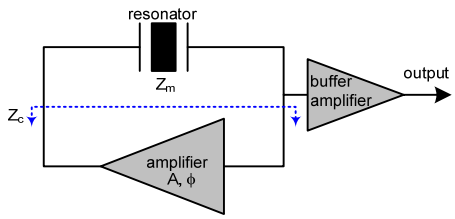

Figure 5.1. Schematic of the electronic oscillator circuit

The oscillator frequency stability, given mainly by the resonator, is a vital requirement. Over the past decades, quartz crystal oscillators have been providing with very accurate frequency reference and excellent stability. However, conventional quartz resonators are bulky, power hungry devices which are hardly integrable with the CMOS circuit. Thus, MEM resonators offer a very interesting alternative for the frequency selective component, especially for portable applications, due to their small sizes, resistance to shocks and IC-integration which promises cost savings, parasitics and power consumption reduction, and opens the possibility of novel architectures.

According to [5.1], an oscillator can be split between the resonator's linear motional impedance, Z_m, and the equivalent impedance of the circuit, Z_c. The critical oscillation condition can be simply expressed in terms of impedances, as:

$$Z_m + Z_c = 0 \quad (5.1)$$

The resonator's motional impedance is given by:

$$Z_m = R_m + j\omega L_m - \frac{1}{j\omega C_m} \quad (5.2)$$

or it can also be expressed as:

$$Z_m = R_m + j\frac{2p}{\omega C_m} \quad (5.3)$$

where p is the relative amount of frequency pulling above the resonator's natural frequency, ω_{res}:

$$p = \frac{\omega - \omega_{res}}{\omega_{res}} \quad (5.4)$$

By splitting Equation (5.2) in two parts, the real and the imaginary one, we see that the condition for stable oscillations becomes:

$$-Re\{Z_c\} = R_m \quad (5.5)$$

$$-Im\{Z_c\} = \frac{2p}{\omega C_m} \quad (5.6)$$

From Equation (5.5) we can see that the negative resistance of Z_m must compensate the positive motional resistance of the MEM resonator. In consequence, R_m is of particular concern for oscillator applications, since usually it tends to be much higher than in the case of the quartz crystal. A low motional resistance value reduces the required negative resistance of the amplifier to ensure oscillation, and therefore reduces the required oscillator bias current (thus the power dissipation).

The small-signal circuit impedance is a bilinear function of its transconductance, g_m. Thus, the Z_c locus in the complex plane is given by a half circle (for g_m>0), as shown in Figure 5.2.

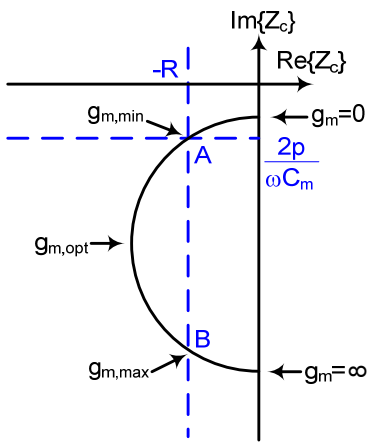

Figure 5.2. Impedance locus for different values of g_m

The condition for stable oscillations given by Equations (5.5-5.6) is satisfied at intersection points A and B, but only point A satisfies also the phase criterion. Thus, the critical transconductance for stability, $g_{m,min}$, is given by point A, while point B represents the maximum transconductance value, $g_{m,max}$, above which no oscillation can start. The optimal value, $g_{m,opt}$, represents the point where the negative resistance of the circuit reaches a maximum; it corresponds also to the minimum start-up time constant. If the MEM resonator motional resistance exceeds this maximum negative resistance, oscillations aren't possible, whichever value g_m might have.

5.1.1. Oscillator Phase Noise

Next to oscillation frequency stability, the phase noise is a key oscillator performance parameter. Noise from different sources (shot, burst, thermal and 1/f) can affect both the oscillator's output amplitude and phase. However, most oscillators possess an amplitude-limiting mechanism in order to maintain the unity gain condition for stable oscillations at large signal levels. This mechanism attenuates also the amplitude fluctuations due to noise, and thus the phase noise generally dominates.

According to [5.2], the phase noise, $L\{\Delta f\}$, can be calculated as:

$$L\{\Delta f\} = 10\,log\left\{\frac{2FkT}{P_{sig}}\left[1+\left(\frac{f_0}{2Q\Delta f}\right)^2\right]\left(1+\frac{\Delta f_{1/f^3}}{|\Delta f|}\right)\right\} \quad (5.7)$$

where F is an empirical noise figure for the oscillator, k is Boltzman's constant, T is the temperature in Kelvin, P_{sig} is the oscillator signal power, f_0 is the oscillation frequency, Q is the resonator quality factor, Δf is the frequency offset from f_0 and $f_{1/f3}$ is the corner frequency between the $1/f^3$ and $1/f^2$ regions, determined experimentally in most cases.

Figure 5.3 shows the phase noise spectrum vs frequency offset, given by Equation (5.7):

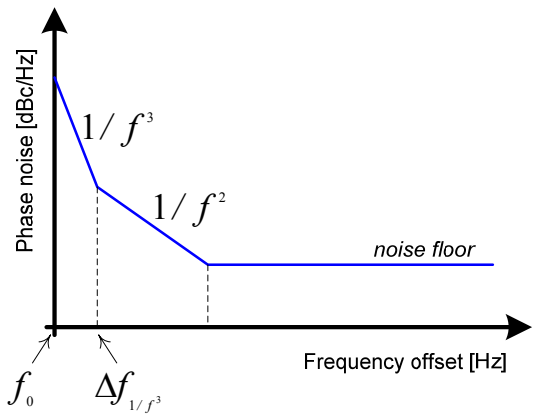

Figure 5.3. Phase noise spectrum according to Equation (5.7)

According to Equation (5.7), the oscillator phase noise decreases as the quality factor increases. That is why in addition to the MEM resonator motional resistance which, as previously explained, should be small enough to be effectively compensated by the circuit's negative impedance, the resonator's quality factor is of great importance for oscillator applications, especially for low noise at frequency offsets close to carrier.

Moreover, the same equation predicts that the output carrier power, P_{sig}, is very important in determining the phase noise performance of the oscillator, particularly at large offsets from carrier, where the resonator quality factor plays a smaller role. At the same time, the carrier power is limited by the power handling ability of the resonator, whose linear behavior should be granted. In MEM-based oscillators, due to lower resonator nonlinearity threshold, the carrier power is usually not limited by the sustaining circuit as in the case of quartz-based oscillators, but by the resonator element [5.3]. This type of limitation leads to unwanted aliasing of the 1/f noise of the sustaining electronics into the oscillator output, by nonlinearity in the resonator's capacitive transducer. The result is a strong $1/f^3$ noise component at close to carrier offsets, which degrades the oscillator phase noise performance and can prevent it from reaching the levels required by GSM standards.

Other noise sources which can degrade the phase noise performance can come from the circuit, due to noise in the active devices (shot, thermal, flicker), to losses in interconnects and in the substrate, or to supply noise. However, as previously mentioned, in current MEM-based oscillators the circuit contribution to phase noise is negligible compared to the resonator nonlinearity effect.

If the frequency selective component is considered linear (for example through gain control), the oscillator block diagram can be represented as shown in Figure 5.4 [5.4], where the primary noise sources of interest are the Brownian noise of the mechanical element, the input current noise of the sustaining amplifier and the noise of the output buffer.

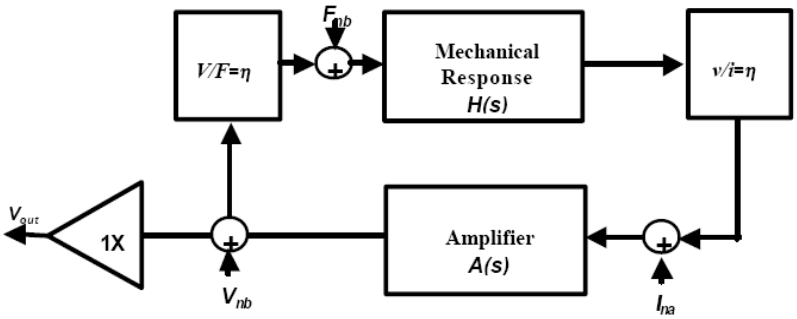

Figure 5.4. Block diagram of an oscillator indicating the primary noise sources as the thermo-mechanical noise force acting on the resonator element, the input current noise of the sustaining amplifier and the noise of the buffer [5.4].

H(s) represents the force-to-velocity mechanical transfer function, *A(s)* represents the transfer function of the sustaining amplifier (constant and equal to *A* when the amplifier bandwidth is much larger than the output frequency of the oscillator) and the transduction blocks (representing electrostatic transduction for voltage-to-force and velocity-to-current) are shown. The transduction is considered symmetric and linear; therefore, the transduction factor is denoted by a constant, η.

The transfer functions relating the thermo-mechanical noise and the input current noise to the output voltage can be written as:

$$\frac{V_{out}}{F_{nb}} = \frac{\frac{A\eta}{m}s}{s^2 + \omega_{res}^2} \quad (5.8)$$

and

$$\frac{V_{out}}{I_{na}} = \frac{A\left(s^2 + \frac{\omega_{res}}{Q_l}s + \omega_{res}^2\right)}{s^2 + \omega_{res}^2} \quad (5.9)$$

The Brownian force noise spectral density for silicon MEM resonators is given by [5.5]:

$$\overline{F}_{nb}^2 = \frac{4k_B T m \omega_{res}}{Q} \quad (5.10)$$

Similarly, analytical expressions for the input current noise of the sustaining amplifier and the noise of the output buffer can be written, which will depend on the amplifier topology.

5.1.2. Oscillator Topologies

The MEM-based oscillator general performance is not only dependent on the micromechanical resonator, but also on the topology choice for the sustaining circuit. So far, several MEM-based oscillators have been demonstrated. The most currently used topologies are the transresistance oscillator and the Pierce oscillator. Each architecture presents individual advantages compared to the other one, which will be briefly discussed next.

- **Transresistance oscillators** have a general form as depicted in Figure 5.5. In actual implementations, gain stages are often added to the initial transresistance

stage, to provide for the necessary loop gain and required loop phase shift. This topology represents an interesting choice for MEM-based circuits, because it can compensate for large R_m values, and has good frequency stability [5.6].

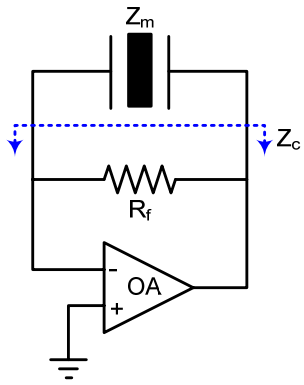

Figure 5.5. General form of the transresistance oscillator

Excellent results have been reported using transresistance oscillators, among which is notable the wine-glass disk resonator-based circuit from [5.6] which very nearly makes the GSM specifications[1] for communication reference oscillators: 60MHz reference oscillator achieving a phase noise density of -100dBc/Hz at 1kHz offset from the carrier, and -130dBc/Hz at far-from-carrier offsets (which, at 10MHz, has $L\{\Delta f\}$=-125dBc/Hz @ 1kHZ offset from carrier, and a noise floor of -147dBc/Hz). Figure 5.6 shows the detailed circuit schematic of the sustaining transresistance amplifier implemented by a fully-differential amplifier in a shunt-shunt feedback configuration (Figure 5.6.a), the top-level circuit schematic of the micromechanical resonator oscillator (Figure 5.6.b) and the phase noise density vs. frequency offset for the same oscillator (Figure 5.6.c).

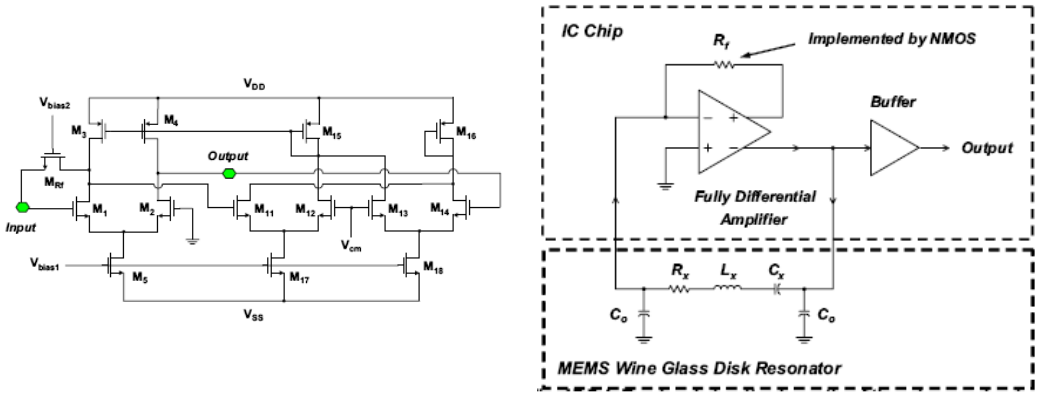

(a) (b)

[1] $L\{\Delta f\}$=-130dBc/Hz @ Δf=1kHz ; $L\{\Delta f\}$=-150dBc/Hz @ Δf=10kHz ; noise floor=-150dBc/Hz

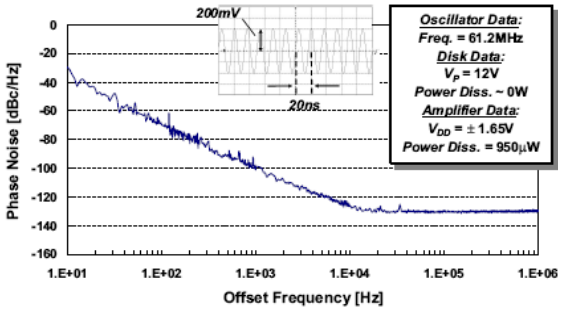

(c)

Figure 5.6. (a) Transresistance amplifier schematic, (b) schematic of the MEM resonator-based oscillator and (c) phase noise density vs. frequency offset for the 60MHz reference oscillator [5.6]

- **Pierce oscillators** are the design of choice for most quartz crystal oscillators, due to their design simplicity, small footprint, low power consumption and low contribution to the phase noise. Figure 5.7 presents the general form of the Pierce topology.

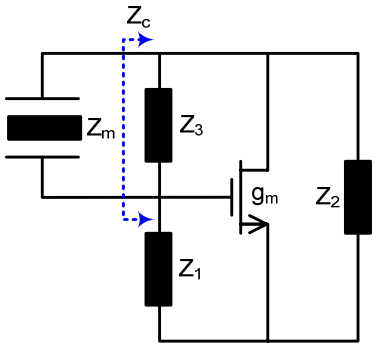

Figure 5.7. General form of the Pierce oscillator

In the case of MEM resonators, which usually have higher motional resistances than the quartz crystals, the conventional Pierce topology functions very close to its compensation capability limit: the higher the R_m, the higher is the transconductance required for stability, $g_{m,min}$. The transconductance can only be increased by using a large g_m transistor or by boosting the current, but both solutions have detrimental impact on the negative resistance at the circuit's output [5.4]. Another approach is to use some circuit adaptation to compensate for R_m and to ensure the phase criterion for stable oscillations, such as using two CMOS amplifier stages [5.7] or two bipolar transistors connected in Darlington configuration, instead of just one [5.8].

Figure 5.8 presents the modified Pierce circuit based on doubly clamped beam resonator which uses a Darlington transconductance to sustain oscillations (Figure 5.8.a) and its theoretical and measured phase noise plot (Figure 5.8.b) [5.8].

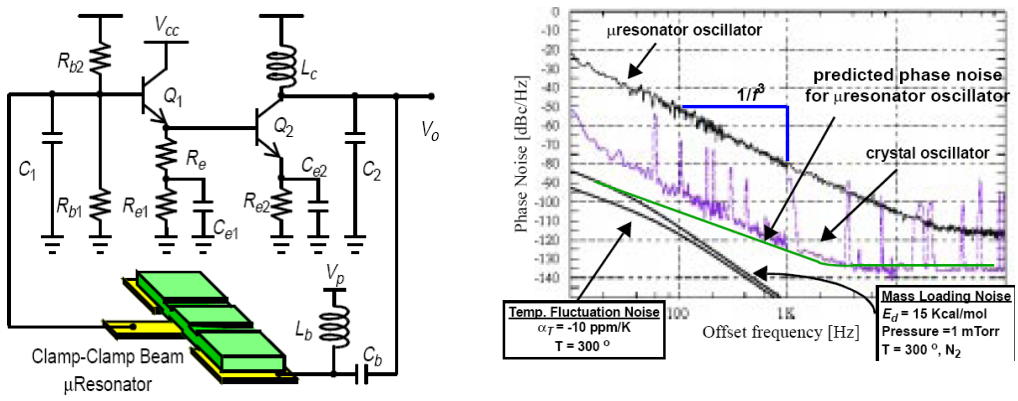

(a) (b)

Figure 5.8. (a) Modified Pierce circuit and (b) phase noise plot vs. frequency offset for the same oscillator [5.8]

The slope of the phase noise curve at small frequency offsets is given by $1/f^3$ noise component, which limits the oscillator's phase noise at -80dBc/Hz, at 1kHz offset from the carrier, probably due to nonlinearity of the MEM resonator component.

5.1.3. Pierce Oscillator Simulation using a Fragmented Membrane BLR

In order to evaluate a possible use of the MEM resonators fabricated during this thesis as frequency selective component in an oscillator, we have simulated[1] a Pierce oscillator based on the 6.25µm-thick fragmented membrane resonator characterized in Chapter 4.

Figure 5.9 presents the simulated circuit. *M1* and *M2* act as a cascade pair to provide sufficient gain to compensate the losses of the resonator. *M3* acts as the buffer transistor to isolate the output stage impedance variations from the oscillator loop. A current source of 5µA sets the current through *M5*, which is mirrored to 50µA through *M6* and *M7*. Total current consumption of the circuit is 110µA. The resonator is connected between the drain of *M2* and gate of *M1*. The parasitic capacitances of the resonator, C_{p1} and C_{p2}, are used to provide the phase shift through the loop. Input for the buffer is taken from the gate of *M1* as this node has lower noise. All transistors are 0.18µm standard CMOS technology. *L/W* values are given next to each transistor.

[1] Simulations were done using Agilent Advanced Design System software using the Harmonic Balance steady state analysis

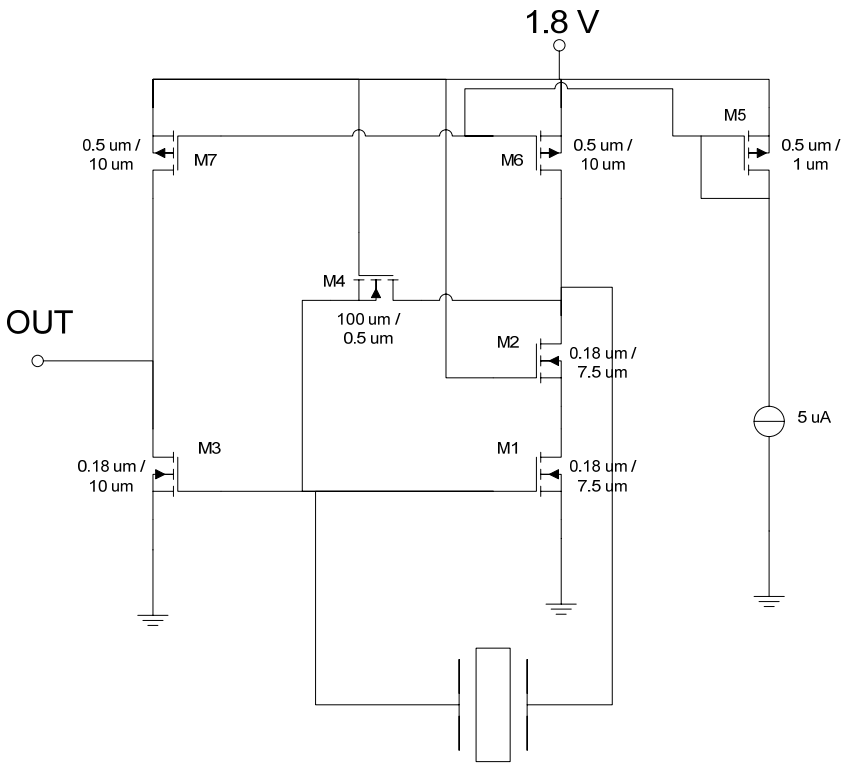

Figure 5.9. Detailed circuit of the Pierce oscillator used in the silulation

Table 5.1. Experimental parameters of the fragmented membrane MEM resonator

Resonance frequency, f_{res}	24.48	MHz
Quality factor, Q	122'000	-
Motional resistance, R_m	59	kΩ
Motional inductance, L_m	46.8	H
Motional capacitance, C_m	0.903	aF
Feedthrough capacitance, C_s	107.9	fF
Parasitic pad capacitance, C_{p1}	448	fF
Parasitic pad capacitance, C_{p2}	345	fF

Table 5.1 presents the experimentally determined parameters for our high-*Q* fragmented membrane resonator used in the simulation:

The simulated phase noise response of our circuit is presented in Figure 5.10, demonstrating the possible implementation of a reference oscillator functioning at 24.48MHz, that achieves a phase noise density of -142dBc/Hz at 1kHz offset from the carrier. The noise floor for our oscillator is at -144dBc/Hz. This result is obtained from small-signal mixing of noise in ideal conditions, supposing linear resonator operation, only considering the noise in the active devices and neglecting any additional noise sources (1/f, AM to PM conversion, interconnect losses and substrate noise). Inclusion

of all remaining noise sources and the nonlinear resonator model would result in a poorer phase noise performance compared to the ideal case.

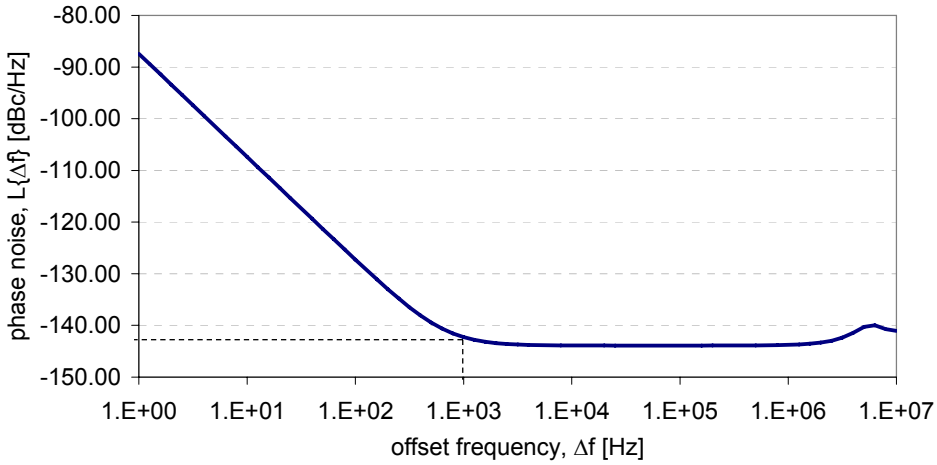

Figure 5.10. Simulated phase noise for a Pierce oscillator based on a fragmented membrane MEM resonator

A useful figure of merit for oscillator performance evaluation can be calculated as:

$$FOM = (-1)\cdot\left[20\,log\left(\frac{\Delta f}{f_0}\right) + L\{\Delta f\} + 10\,log\left(\frac{P}{1mW}\right)\right] \quad (5.11)$$

Our oscillator consumes only 99μW of power, which gives an *FOM*≈240 at 1kHz offset from carrier. This value is very good compared to state of the art results such as the 60MHz oscillator from [5.6], which consumes 430μW of power towards phase noise marks of -110dBc/Hz at 1kHz and thus has an *FOM*≈206.

Table 5.2 presents the main resonator characteristics and the phase noise performance for several MEM-based oscillators reported in the literature and for a commercially available ultra-low phase noise quartz crystal oscillator [5.9], in comparison to our simulated Pierce oscillator based on fragmented membrane MEM resonator. The fragmented membrane MEM resonator has one of the highest quality factors, and its motional resistance can be further reduced by scaling down the actuation gap. Our oscillator performance is comparable to state of the art MEM-based oscillators, with phase-noise performance which nearly satisfies the GSM specification requirements.

Table 5.2. Main parameters for different MEM-based oscillators, compared to quartz-crystal oscillator

Reference	Resonator				Oscillator	
	Type	f_{res} [MHz]	Q	R_m [kΩ]	$L\{\Delta f\}$ [dBc/Hz]	Δf [KHz]
Our work (simulation)	Fragmented membrane	24.48	122'000	59	-142 -144	1 far
Nguyen - Pierce [5.8]	CC-beam	9.75	3'600	17.5	-80 -117	1 far
Nguyen - Transresistance [5.6]	CC-beam	10	3'100	8.7	-82 -116	1 far
	Wide CC-beam	10	1'036	0.3	-80 -120	1 far
	Wine-glass disk	60	48'000	1.5	-110 -132	1 far
	Wine-glass disk	10			-125 -147	1 far
Kaajakari [5.10]	Square-extensional	13.112	130'000	4.47	-138 -150	1 far
Quartz oscillator CVHD-950 [5.9]	Quartz	50 - 125	n/a	n/a	-131 -162	1 far

5.2. Filters

As in the case of MEM-based oscillators, the lures of miniaturization and possible CMOS cointegration represent main research drivers for RF and intermediate frequency (IF) microelectromechanical filters.

A typical bandpass filter is composed of several resonator tanks connected by coupler networks, as shown in Figure 5.11.a.

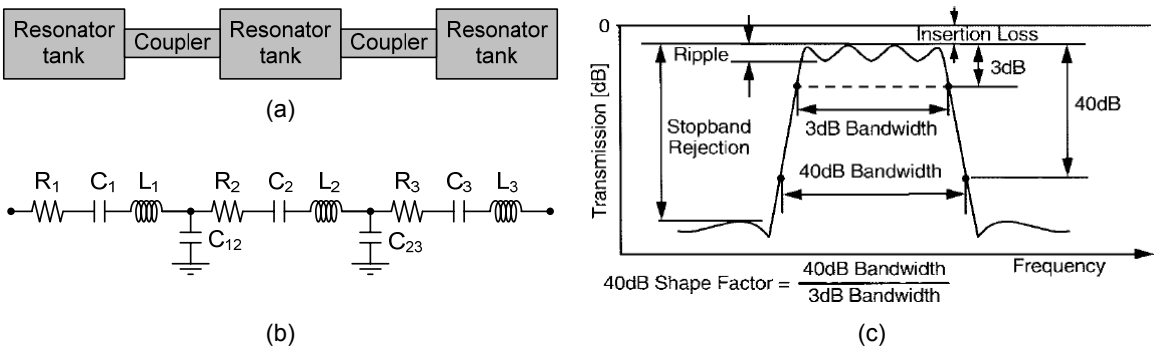

Figure 5.11. Typical filter (a) topology, (b) ladder implementation and (c) specification parameters [5.11]

Such a filter can be implemented using series LCR tanks and capacitive couplers (Figure 5.11.b).The parameters used in general for filter specifications, according to [5.11], are shown in Figure 5.11.c. The filter performance increases by reducing the insertion loss (*IL*) and ripples, and by increasing the stopband rejection. Also, tiny percent bandwidths (calculated as the ratio between the 3dB bandwidth and the center frequency, times 100) and small shape factors (close to unity), thus very steep passband to stopband roll-offs are important [5.12].

Similarly to electrical filters, mechanically or electrically coupled MEM resonators (arrays) may be used for filtering applications. Multiple structures can be mechanically connected together through quarter wavelength beams placed in the nodal points, as shown in Figure 5.12.a: in this case, two flexural-beam resonators which, as explained in [5.13], can vibrate in phase or in anti-phase, generating two peaks in the frequency response plot (Figure 5.12.b). The lower frequency peak corresponds to the symmetric vibration mode, and the higher frequency one to the anti-symmetric mode. The filter center frequency is determined mainly by the individual resonators, while the separation between peaks, which sets the bandwidth is given by a ratio of the stiffness of the coupling beam and that of the resonator, at the beam attachment locations.

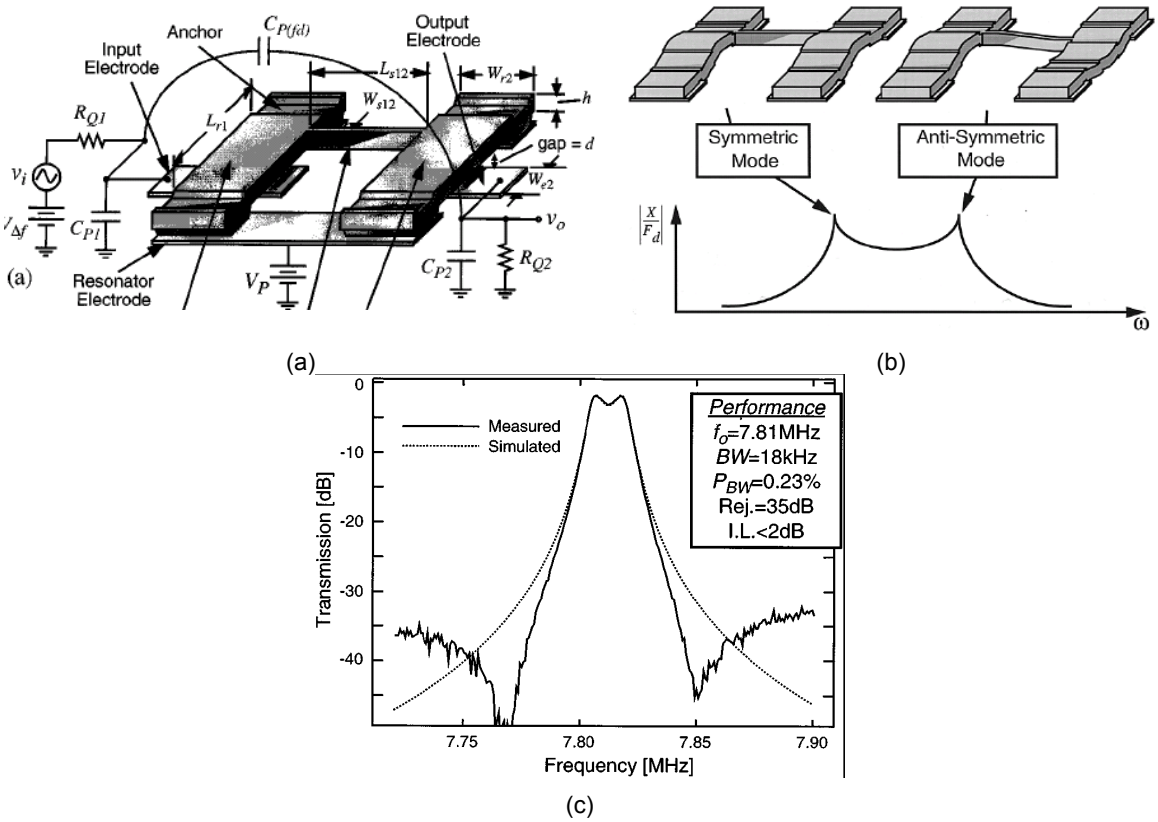

Figure 5.12. (a) Schematic of a two-resonator micromechanical filter, (b) Filter mode shapes and their correspondence to specific peaks in the unterminated frequency characteristic and (c) Measured spectrum for a terminated 7.81-MHz micromechanical filter with excessive input/output shunt capacitance [5.13]

The device in Figure 5.12.a is operated by applying a DC bias on the coupled beams, and an AC signal to the input electrode, which creates a vibration in the first resonator. This vibration is transmitted to the second one through the coupling beam. The output resonator motion creates a dc-biased, time-varying capacitor between the structure and the output electrode, which then sources a variable output current directed to resistor R_{Q2}, which converts the current to an output voltage v_o and, along with R_{Q1}, provides the proper termination impedance required to flatten the jagged passband characteristic of Figure 5.12.b. The measured spectrum from Figure 5.12.c belongs to a 7.81MHz bandpass filter based on two coupled CC-beam resonators. The bandwidth of this filter is 18kHz, the insertion loss is 1.8dB, for a percent bandwidth of 0.23%.

Other successful MEM-based filter implementations have used flexural-mode [5.14] and, more recently, bulk-mode MEM resonators [5.15-16] which resulted in 163MHz filters with insertion losses as low as 2.5dB, for extremely small percent bandwidths of 0.06% and passband ripples less than 0.5dB.

In the future, MEM-based filters could provide excellent reconfigurability, frequency processing capability and power consumption to channel-selector filter banks used for RF front-end architectures. Figure 5.13 presents the schematic block diagram of a MEMS-based receiver using a channel selector composed of self-switching RF filters in its RF front-end [5.12].

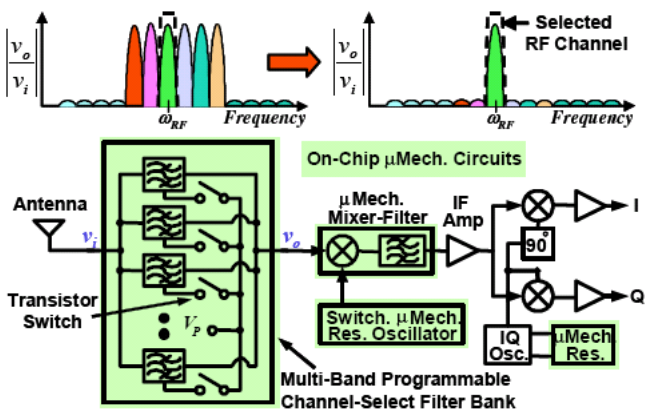

Figure 5.13. Schematic block-diagram of MEMS-based receiver using a channel selector composed of self-switching RF filters in its RF front-end [5.12]

A key filter parameter for RF front-end architecture applications is the termination impedance required for passband flattening, which should be as small as possible, to allow matching to 50Ω. Until recently, the high values obtained for the termination impedance with order of tens of kΩ's have represented a major impediment for MEM-based filters. As an example, the bandpass filter from Figure 5.12 requires an impedance of 19.6 kΩ [5.13].

An approach to minimizing the MEM-filter termination impedance is by using parallel-type filter architecture, as shown in Figure 5.14. Each subfilter structure uses two disk array composites, formed by 15 identical disk resonators linked by half wavelength coupling beams in order to accentuate the single frequency response selected by input excitation electrode configuration (Figure 5.14.a). The two subfilters are connected in parallel, as shown in Figure 5.14.b, where the inverter from the second subfilter's path alters its relative phase from the one of the first subfilter. In this configuration, frequency components between the resonant peaks add in phase, while the ones outside this range subtract, resulting in flatter passband between the peaks, increased rejection outside the range and sharper passband to stopband roll-off. Figure 5.14.c presents the measured unterminated and terminated frequency characteristics of such a parallel-class filter centered on 163.3MHz, which demonstrates an insertion loss of 2.73dB for a percent bandwidth of 0.16%, an impressive shape factor at 20dB of 1.78 and ripples smaller than 2dB, using termination impedance of only 4kΩ.

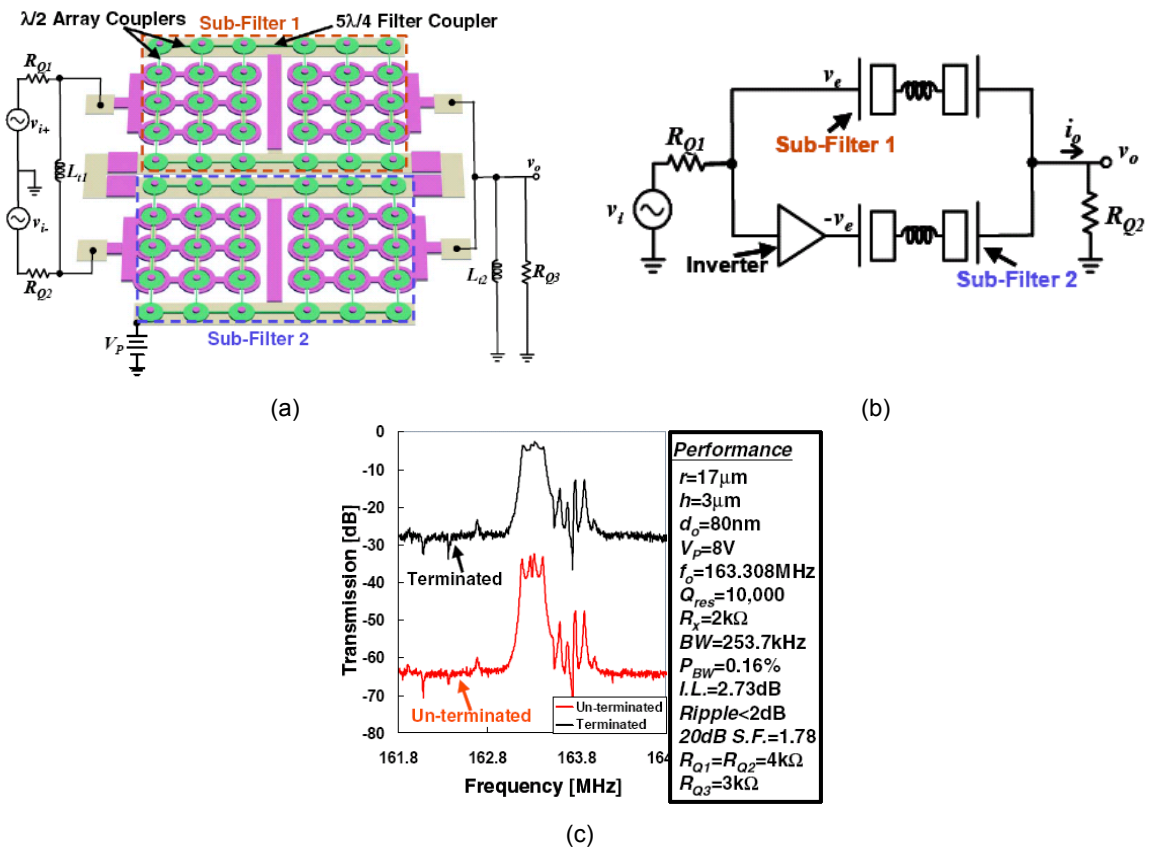

Figure 5.14. (a) Schematic of the eight-order MEM parallel-class disk array, (b) circuit schematic of a parallel-class filter using two subfilters and (c) measured unterminated and terminated frequency characteristics for a fabricated 8th order parallel-class disk filter array [5.12]

We have also designed and fabricated several filter configurations based on coupled bulk mode resonators. Figure 5.15 presents the layout images of fragmented membrane–based resonator array (Figure 5.15.a) and of an array based on disk

resonators (Figure 5.15.b). In Figure 5.15.c is shown an SEM close-up view on two of the devices composing a fabricated disk resonator array. By actuating all structures in phase, such a design could also be used as resonator with improved power handling: the current handling ability of the array will be equal to the sum of the currents from all constituent resonators [5.17].

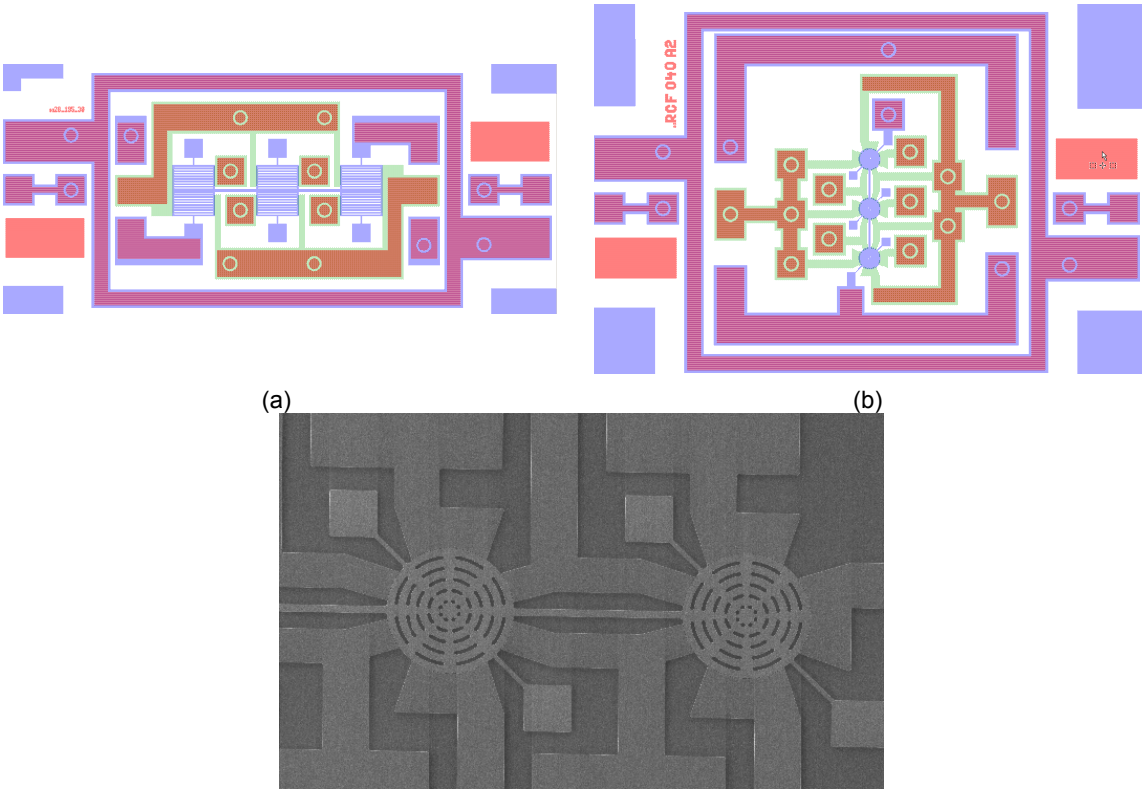

Figure 5.15. Design layouts of coupled architectures based on (a) fragmented membrane resonators, (b) disk resonators and (c) SEM close-up image of a fabricated disk resonator array

The electrical contacts between electrodes have been designed through the cap, which was supposed to be fabricated by our EU project partner, IMEC, but which finally was not implemented due to technological challenges. Thus, the structures haven't been characterized.

5.3. Mass Sensing

Mechanical resonators are also very attractive mass sensing transducers for a variety of physical, chemical and biological applications such as explosive detection, fast drug screening, or gene and antibody detection [5.18-19]. Such sensors, especially when integrating nanometre-sized vibrating structures (NEM), may achieve very high sensitivities, with minimum detectable masses as small as yoctograms (10^{-24} g) [5.20-

21]. This value clearly surpasses the classical quartz crystal microbalance (QCM) performance which is in the order of 10^{-18}g.

The MEM-based mass sensor functioning principle relies on mass change detection by measuring the shift in resonance frequency (f_{res}), as shown in Equations (5.12-13):

$$f_{res} = \frac{1}{2\pi}\sqrt{\frac{k_{eff}}{m_{eff}}} \quad (5.12)$$

For an added mass which is small in comparison with the effective mass (m_{eff}) of the resonator, the effective spring coefficient (k_{eff}) remains constant, and thus the resonance frequency only depends on the square root of the mass:

$$f_{res} \sim \frac{1}{\sqrt{m_{eff}}} \quad (5.13)$$

The minimum detectable mass, also called the mass sensitivity (δm), can be calculated considering the fundamental limit imposed upon mass measurements by thermomechanical noise, as [5.22]:

$$\delta m \cong 2m_{eff}\sqrt{\frac{\Delta f}{Q \cdot 2\pi f_{res}}} \cdot 10^{-\frac{DR}{20}} \quad (5.14)$$

$$DR(dB) = 10 \cdot log\left(\frac{E_c}{k_B T}\right) \quad (5.15)$$

$$E_c = m_{eff} \cdot (2\pi f_{res})^2 \cdot \langle x_c^2 \rangle \quad (5.16)$$

where Δf is the measurement bandwidth, Q is the quality factor of the resonator, DR is the dynamic range and E_c is the kinematic energy of the resonator when driven at a constant mean square amplitude $<x^2_c>$.

Also, the mass responsivity of the device can be calculated as:

$$R \cong \frac{2\pi f_{res}}{2m_{eff}} \quad (5.17)$$

As shown by Equations (5.14-16), the main resonator parameter which determines its sensitivity is the effective mass of the vibrating structure. The smaller the mass, the better is the sensitivity (i.e. smaller masses can be detected). Additionally, the structure's resonance frequency and quality factor are also influencing its mass sensitivity. Thus, resonators with small masses, vibrating with high quality factors at high frequencies are needed in order to achieve high sensitivities.

Recent microfabrication advancements have allowed the manufacturing of NEM resonators which can detect extremely small masses. Such a device, based on doubly clamped beam resonator is shown in Figure 5.16 [5.21].

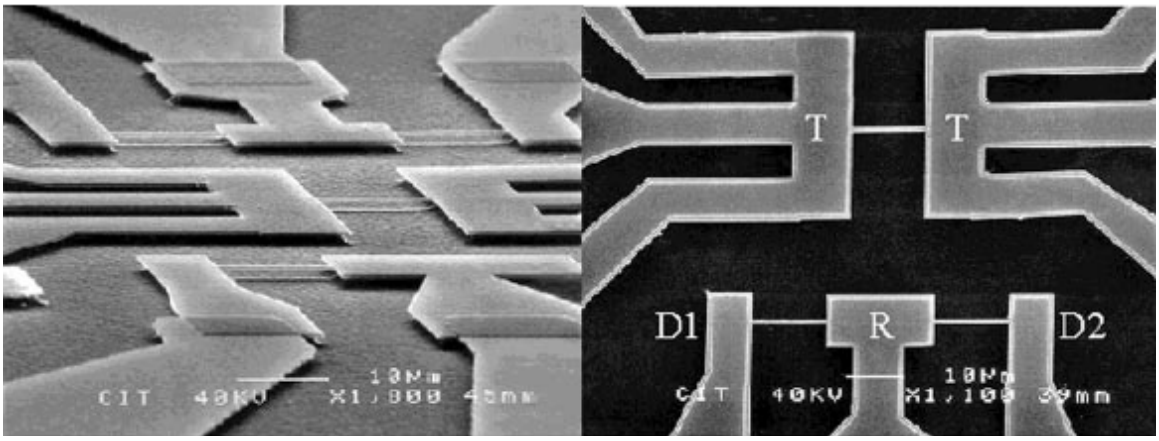

(a)

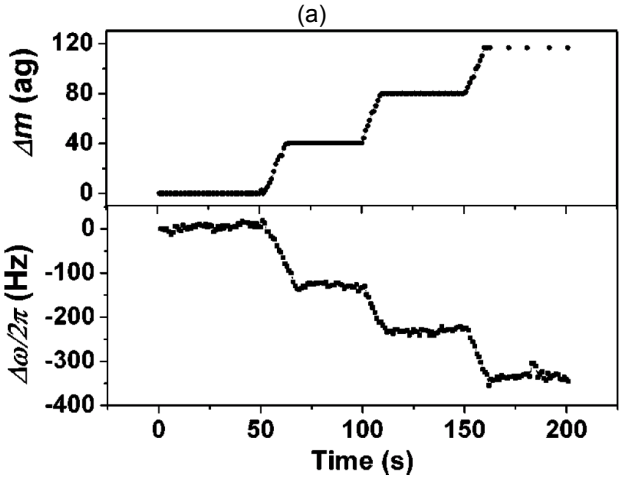

(b)

Figure 5.16. (a) SEM images of nanomechanical CC beam sensor elements configured in a RF bridge; *D1* and *D2* are the actuation ports and *R* is used for detection. The central suspended structure attached to three contact pads on each side, labelled T, is for monitoring the local temperature. (b) Measured frequency shifts, Δf (bottom) induced by sequential gold atom adsorption upon the CC beam resonator; the accreted mass of gold atoms, Δm, in the upper plot is measured by a separate quartz crystal detector [5.21]

The beams in Figure 5.16.a are made out of SiC with top surface metallization layers of 80nm of Al and have the following dimensions: length, L=14.2μm, width w=620nm and

thickness t=259nm. The fundamental in-plane flexural mode vibration has a frequency f_{res}=32.8MHz and quality factor, Q=3000. The beams are embedded in a RF bridge configuration with corresponding actuation *(D1* and *D2*) and detection (*R*) ports. The single suspended structure labelled *T* enables four-wire resistance measurements which provide extremely sensitive monitoring of the local temperature, set at T=17K. Special precautions have been taken to reduce thermal fluctuations and drifts, in order to minimize any unwanted frequency fluctuations.

Figure 5.16.b presents the CC beam resonator frequency shift measurement induced by sequential 40ag gold atom adsorption. The observed frequency fluctuations correspond to a 2.5ag mass sensitivity (for the 2ms averaging time employed). The upper Δm measurement is done with a separate calibrated QCM. By employing a measurement bandwidth Δf=3kHz, an experimental mass sensitivity of 2.53ag is obtained.

By scaling the resonating structures to even smaller dimensions, zeptogram (10^{-21}g) mass detection has been demonstrated [5.23]. Figure 5.17 presents the measured frequency shift for a SiC CC beam resonator with L=2.3μm, w=150nm and t=100nm, vibrating at 190MHz with a quality factor Q~5000. Measurements were done at a temperature T=37K, with pulsed deliveries of 100zg N_2 molecules accreted by the resonator. The measured data demonstrates that minimum masses of ~20zg can be detected employing a 1s averaging time.

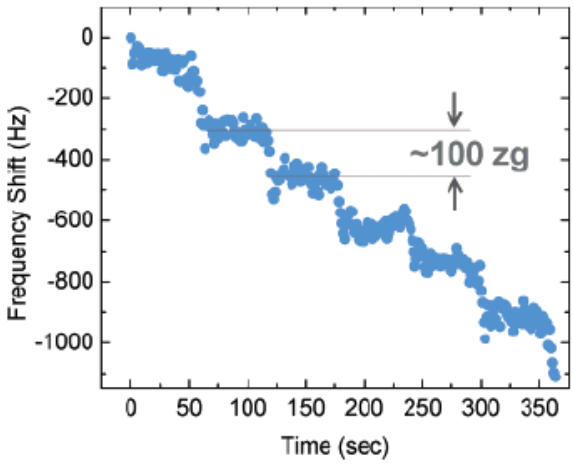

Figure 5.17. Real time zeptogram-scale mass sensing experiment using a 190MHz resonator within a cryogenic ultrahigh vacuum apparatus (each step in the data corresponds to a ~100zg mass accretion) [5.23]

However, larger scale devices can be also used for more relaxed mass detection applications. Considering the MEM simple longitudinal beam resonator studied throughout this thesis (Figure 5.18), which has the parameters given in Table 5.3, the minimum mass that can be sensed in vacuum with this device is $\delta m \approx 0.5pg$. This figure

is sufficiently small for applications such as cell detection (a wet E. Coli bacteria weights around 1pg).

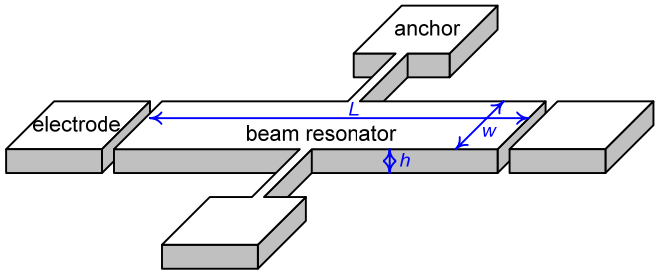

Figure 5.18. Schematic of the simple longitudinal beam resonator

Table 5.3. Parameters of the simple longitudinal beam resonator

L, resonator length	161	[μm]
w, resonator width	10	[μm]
h, silicon layer thickness	6.25	[μm]
ρ, Si density	2330	[kg/m^3]
$<x_c>$, mean square amplitude	5	[nm]
f_{res}, resonance frequency	26	[MHz]
Q, quality factor	95'000	-
P , operating pressure	$<10^{-5}$	mbar
df, measurement bandwidth	10	[kHz]
T, temperature	300	[K]
δm, mass sensitivity	**0.5**	**pg**
***R*, mass responsivity**	**3.5**	**kHz/pg**

Preliminary tests have been started for evaluating the possible use as mass detection sensors of the MEM resonators developed during this thesis work. Many cell-detection applications require the resonator sensors to operate in saline water environment (or at least to sustain liquid submersion for cell attachment) [5.24-25]. Prior to submersion, the sensors could also be selectively functionalized with specific antigens in order to bind targeted cells at wanted sites on the device [5.25].

We have performed initial liquid dispensing tests using an experimental setup which employed a capillary for water dispensing which was fixed on a DC probe inside the PMC prober[1]. Water drops with diameters as small as few 10's of microns were delivered through the capillary directly to the resonator surface. So far, the tests have been unsuccessful due to structures collapsing when soaked. Further enhancements of the dispensing setup and of the resonator design and technology (e.g. by including fill

[1] A description of the PMC measurement setup is given in Chapter 4

patterns [5.26] or by employing solid gaps for stiffer structures [5.27]) can be done in the future in order to successfully operate the structures in liquid environment.

However, applications such as gas sensing, which only require the resonators to operate in air, may be easier attained given the promising fragmented membrane resonator performance obtained at atmospheric pressure: the structure still has a quality factor in the order of 3'500, which is much higher than similar results obtained for flexural beam resonators. Figure 5.19 shows the S_{21} peaks measured at different ambient pressures, starting from vacuum (p<10^{-5}mbar) up to atmospheric pressure, for the fragmented membrane resonator summarized in Table 5.4. All measurements were done with a DC bias voltage of 8V. Measurements in vacuum used -20dBm AC power; above 500mbar, the power was increased to 0dBm. This resonator has a theoretical mass sensitivity in air, $\delta m \approx 8.7pg$.

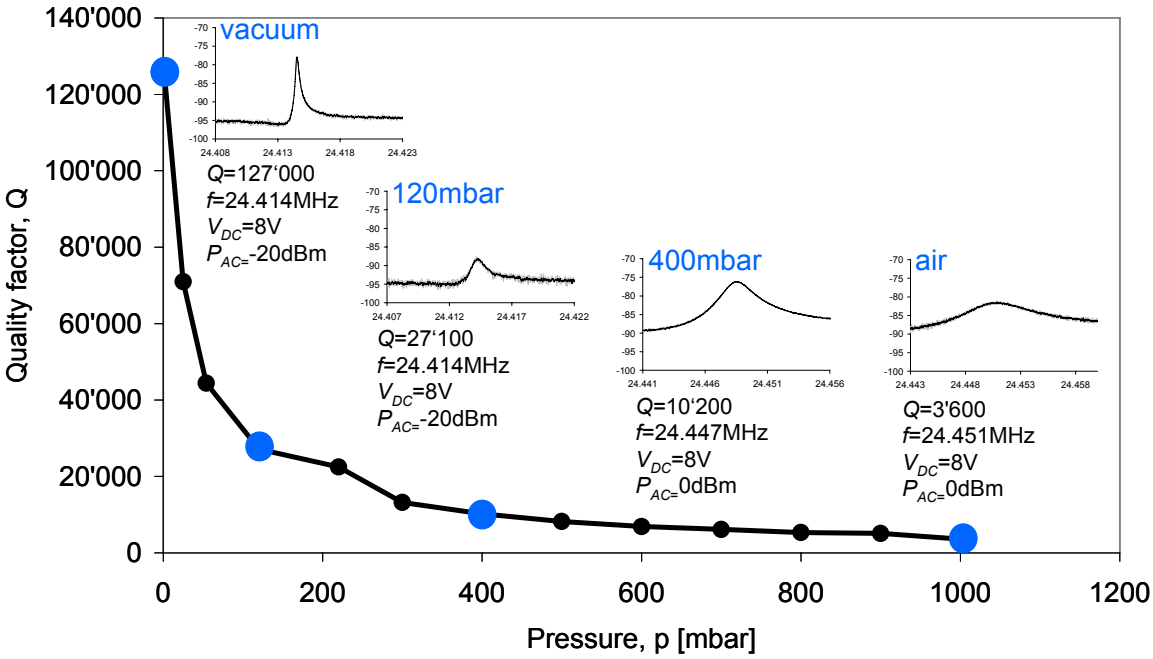

Figure 5.19. Quality factor plot versus ambient pressure, and S_{21} peaks of a fragmented-membrane resonator, measured from high vacuum up to atmospheric pressure

Table 5.4. Parameters of the fragmented membrane resonator measured in air

L_b, beam length	151	[μm]	ρ, Si density	2330	[kg/m^3]
w_b, beam width	5	[μm]	f_{res}, resonance frequency	24.45	[MHz]
N, number of parallel beams	20	-	Q, quality factor	3'600	-
L_c, lateral connection length	195	[μm]	$\langle x_c \rangle$, mean square amplitude	5	[nm]
w_c, lateral connection width	5	[μm]	df, measurement bandwidth	10	[kHz]
h, silicon layer thickness	6.25	[μm]	T, temperature	300	[K]
R, mass responsivity	**0.3**	**kHz/pg**	**δm, mass sensitivity**	**8.7**	**pg**

5.4. Summary

This final chapter has presented the three main MEM resonator applications, in the field of electronic oscillators, filters, and mass sensing devices. Potential size reductions as well as MEMS-IC cointegration, which promises cost savings, parasitics and power consumption decrease, and opens the possibility of novel architectures, are key drivers behind the research conducted for MEM-based circuits. Sensors could also benefit from the extremely high mass sensitivity of resonant devices, which can detect small molecules with masses in the order of tens of zeptograms (10^{-21}g).

The bulk mode resonators developed and discussed throughout this thesis can successfully be integrated in oscillator circuits, as we have demonstrated by simulating a Pierce topology based on 24.48MHz fragmented membrane BLR. Our oscillator has very good phase-noise performance, which nearly meets the GSM specifications.

Preliminary tests for evaluating the use of our resonators as mass sensors have also been started, and more study is required for demonstrating their use in liquid environments, as required for biological applications. However, very promising results have been obtained by operating the devices in air. The fragmented-membrane MEM resonator has a high quality factor of 3’600, comparable to state of the art results, which could enable gas sensing applications with detection done without a special package, just by direct exposure of the resonator to the environment.

5.5. Bibliography

[5.1] E.A. Vittoz, M.G.R. Degrauwe, and S. Bitz, “High-Performance Crystal Oscillator Circuits: Theory and Application”, IEEE Journal of Solid-State Circuits, volume 23, no. 3, 1988, pp. 774-783

[5.2] T.H. Lee, and A. Hajimiri, “Oscillator Phase Noise: A Tutorial” IEEE Journal of Solid-State Circuits, volume 35, no. 3, 2000, pp. 326-336

[5.3] S. Lee, and C. T.-C. Nguyen, “Influence of Automatic Level Control on Micromechanical Resonator Oscillator Phase Noise”, IEEE International Frequency Control Symposium, 2003, pp. 341–349

[5.4] Deliverable D2.1, IST-2003-507914 NanoTIMER, January 2006

[5.5] Y.-W. Lin, S. Lee, S.-S. Li, Y. Xie, Z. Ren, and C.T.-C. Nguyen “Series-Resonant VHF Micromechanical Resonator Reference Oscillators”, IEEE Journal of Solid- State Circuits, volume 39, no.12, 2004, pp. 2477-2491

[5.6] T.S.A. Wong and M. Palaniapan, “Micromechanical Oscillator Circuits: Theory and Analysis”, Journal of Analog Integrated Circuits and Signal Processing, volume 59, no. 1, 2009, pp. 21-30

[5.7] J. Verd, A. Uranga, G. Abadal, J.L. Teva, F. Torres, J. Lopez, F. Perez-Murano, J. Esteve, and N. Barniol, “Monolithic CMOS MEMS Oscillator Circuit for Sensing in the Attogram Range”, IEEE Electron Device Letters, volume 29, no. 2, 2008, pp. 146-148

[5.8] S. Lee, M.U. Demirci, and C.T.-C. Nguyen, “A 10-MHz micromechanical resonator Pierce reference oscillator for communications”, The 11th International Conference on Solid-State Sensors & Actuators (Transducers ’01), 2001, pp. 1094-1097

[5.9] Data sheet, Model CVHD-950, Ultra-Low Phase Noise Voltage Controlled Crystal Oscillator, Crystek Crystals Corporation

[5.10] V. Kaajakari, T. Mattila, A. Oja, J. Kiihamäki, and H. Seppä, “Square-Extensional Mode Single-Crystal Silicon Micromechanical Resonator for Low-Phase-Noise Oscillator Applications”, IEEE Electron Device Letters, volume 25, no. 4, 2004, pp. 173-175

[5.11] K. Wang and C. T.-C. Nguyen, “High-order medium frequency micromechanical electronic filters,” IEEE Journal of Microelectromechanical Systems, volume 8, no. 4, 1999, pp. 534-557

[5.12] S.-S. Li, Y.-W. Lin, Z. Ren, and C.T.-C. Nguyen, “A Micromechanical Parallel-Class Disk-Array Filter”, IEEE International Frequency Control Symposium, 2007, pp. 1356-1361

[5.13] F.D. Bannon, J.R. Clark, and C.T.-C. Nguyen, “High-Q HF Microelectromechanical Filters”, IEEE Journal of Solid-State Circuits, volume 35, no. 4, 2000, pp. 512-526

[5.14] M.U. Demirci and C.T.C. Nguyen, “A low impedance VHF micromechanical filter using coupled-array composite resonators”, The 13th International Conference on Solid-State Sensors, Actuators and Microsystems (Transducers‘05), 2005, volume 2, pp. 2131- 2134

[5.15] S.-S. Li, Y.-W. Lin, Z. Ren, and C.T.-C. Nguyen, “Disk-array design for suppression of unwanted modes in micromechanical composite-array filters,” The 19th IEEE International Conference on Micro Electro Mechanical Systems (MEMS’06), 2006, pp. 866-869

[5.16] S.-S. Li, Y.-W. Lin, Z. Ren, and C.T.-C. Nguyen “An MSI micromechanical differential disk-array filter,” The 14th International Conference on Solid-State Sensors & Actuators (Transducers’07), 2007, pp. 307-311

[5.17] Y.-W. Lin, S.-S. Li, Z. Ren, and C.T.-C. Nguyen, “Low Phase Noise Array-Composite Micromechanical Wine-Glass Disk Oscillator”, IEEE International Electron Devices Meeting (IEDM), 2005, pp. 287-290

[5.18] G. Muralidharan, A. Wig, L.A. Pinnaduwage, D. Hedden, T. Thundat, and R.T. Lareau, “Adsorption–desorption characteristics of explosive vapors investigated with microcantilevers”, Journal of Ultramicroscopy, volume 97, 2003, pp. 433-439

[5.19] T. Y. Kwon, K. Eom, J. H. Park, D. S. Yoon, T. S. Kim and H. L. Lee "In situ real-time monitoring of biomolecular interactions based on resonating microcantilevers immersed in a viscous fluid", Applied Physics Letters, volume 90, issue 22, 2007, 223903

[5.20] N. V. Lavrik and P. G. Datskos, “Femtogram mass detection using photothermally actuated nanomechanical resonators”, Applied Physics Letters, volume 82, no. 16, 2003, pp. 2697-2699

[5.21] K. L. Ekinci, X. M. H. Huang, and M. L. Roukes, “Ultrasensitive nanoelectromechanical mass detection”, Applied Physics Letters, volume 84, no. 22, 2004, pp. 4469-4471

[5.22] K. L. Ekinci, Y. T. Yang and M. L. Roukes, “Ultimate limits to inertial mass sensing based upon nanoelectromechanical systems”, Journal of Applied Physics, volume 95, no. 5, 2004, pp. 2682-2689

[5.23] Y.T. Yang, C. Callegari, X. L. Feng, K. L. Ekinci, and M. L. Roukes, “Zeptogram-scale nanomechanical mass sensing”, Nano Letters, volume 6, no. 4, 2006, pp. 583–586

[5.24] K.D. Bhalerao, S.C. Mwenifumbo, A.B. Soboyejo, and W.O. Soboyejo, “Bounds in the sensitivity of BioMEMS devices for cell detection”, Biomedical Microdevices, volume 6, issue 1, 2004, pp. 23-31

[5.25] B. Ilic, D. Czaplewski, H. G. Craigheada, and P. Neuzil, “Mechanical resonant immunospecific biological detector”, Applied Physics Letters, volume 77, no. 3, 2000, pp. 450-452

[5.26] H. Chandrahalim, S.A. Bhave, E.P. Quevy, and R.T. Howe, “Aqueous Transduction of Poly-SiGe Disk Resonators”, International Conference on Solid-State Sensors, Actuators and Microsystems (Transducers’07), 2007, pp. 313-316

[5.27] Y. Lin, S. Li, Z. Ren, and C. Nguyen, “Vibrating Micromechanical Resonators with Solid Dielectric Capacitive Transducer Gaps”, IEEE Internalional Frequency Control Symposium and Exposition (IFCS '05), 2005, pp. 128-134

Chapter 6

Conclusions and perspectives

6.1. Major Achievements in this Work

The work presented in this manuscript was dedicated to the development and fabrication of first nano-gap silicon-on-insulator MEM resonators fabricated in the clean room of EPFL. Overall, this was an effort of more than four years, supported by an FP6 European project (NanoTIMER) and, in the final year, by a grant of the Faculty of Engineering (STI) of EPFL.

The main technical and scientific achievements of this thesis can be summarized as follows:

- Two main MEM bulk lateral resonator designs have been investigated by simulations and experiments: a longitudinal beam resonator and an original fragmented-membrane resonator, both functioning in the tens of MHz frequency range. Design optimizations have been proposed and validated, enabling the decrease of motional resistance (R_m) coupled with quality factor (Q) enhancement through energy loss minimization. More concretely, in the best designs we have achieved values of R_m lower than 100KΩ and values of Q higher than 100'000.

- An original fabrication process has been developed based on a lateral spacer technique. This process employs only four masks for manufacturing SOI-based, fully monocrystalline MEM resonators with extremely narrow transduction gaps (100nm), without the need of advanced lithography techniques. The process was validated on two silicon film thicknesses (1.5μm and 6.25μm), corresponding to partially depleted SOI, which can be considered a substrate of choice for the fabrication of future integrated hybrid MEMS-CMOS integrated circuits.

- Successful characterization of the resonators demonstrates excellent performance at room temperature: quality factors as high as 235'000 and motional resistances as low as 59kΩ have been measured in vacuum. Atmospheric pressure frequency response measurements of the fragmented membrane resonators show a quality factor of 3'600, which is amongst the best values reported to date.

- The DC bias influence on resonator performance was discussed, confirming theoretical bias dependence of the motional resistance and the frequency shift due to spring softening effect. In addition, the nonlinear resonator response was observed at high AC signal powers, and experimental nonlinearity limits were established for both types of resonators, setting power guidelines for circuit applications such as oscillators.

- A novel experimental study on temperature dependence (between 80K and 320K) of fragmented membrane resonator operation emphasizes two key aspects: (1) the resonance frequency trend follows Wachtman's law for the whole temperature range and (2) the quality factor dependence on temperature, probably due to internal losses, follows Debye's relaxation equation. Inline with this trend, significant Q increase and R_m reduction are reported at cryogenic temperatures.

- Several applications have been investigated for the MEM resonators realized throughout this work, including the possible use in oscillator circuits.
    - A simulated Pierce oscillator topology based on 24.48MHz fragmented membrane BLR has shown not only clear functionality but very good phase-noise performance of -142dBc/Hz at 1kHz offset from the carrier and -144dBc/Hz far from carrier, values which are very close to the actual GSM specifications.
    - Furthermore, mass-detection applications of MEM and NEM resonators have been explored, rather from a feasibility and achievable performance point of view and as a review of existing literature. The experimentally confirmed good performances of fragmented-membrane resonators in atmospheric pressure could enable gas sensing applications with the detection done by direct exposure of the resonator to the environment, without the need of a special package. However, it is obvious that further increase of the sensitivity of the MEM resonator to mass loading needs size scaling (nano-scale resonators) combined with appropriated functionalization of their surfaces.

6.2. Perspectives

The field of MEM resonators has recently seen great advancement, as devices with high quality factors and low motional resistances are successfully manufactured with high yields. However, before the technology can be considered completely established, there are still some challenges which need to be addressed:

- *Integration*: Currently, most MEMS-based products use hybrid "system in package" approaches, in which the MEMS devices and the electronics fabricated separately are coupled into a final compete device. In order to fully benefit from promised MEMS improvements, such as reduced parasitics, smaller size and lower cost, IC-MEM integration should be proven.

- *Temperature stability*: From a time reference application point of view, the frequency stability with temperature of MEM resonators is a key requirement. While quartz crystals provide excellent stability (below 1ppm/°C depending on

the crystal cut), typical MEM resonators only offer temperature drifts in the order of -30ppm/°C. Several temperature compensation methods have been investigated so far. However, they are complicated, not very efficient and may adversely affect the long-term stability of the device. Thus, this subject still needs further research and implementation of novel solutions.

- *Packaging*: Last but not least, the MEM resonator packaging technology is currently a major limitation in using the devices for commercial applications. MEM resonators are fragile structures, which need to be protected by very clean, enclosed environments from any contaminant which would degrade their short- or long-term performance. Most resonators would greatly benefit from a vacuum packaging which ensures low damping, thus high quality factors. The package should not degrade the MEMS performance through addition of parasitic capacitances or stress-induced stiffness changes. Finally, the packaging should meet all above requirements while maintaining a low cost.

- *Challenges for applications in sensing*: MEM resonator applications in sensing can enable sensitivities and resolutions very difficult (and sometimes quasi-impossible) to attend with other technologies. However, the success of sensing applications depends on: (1) the control of processes and process variations to fabricate nano-electro-mechanical structures, (2) the functionalization of the nanostructures at small scale to make them selective only to certain gas and liquid species, (3) the fabrication and operation of NEM resonators in arrays and the development of detection and specific signal processing in order to exploit their poor signal-to-noise ratios, (4) their co-integration with CMOS to have the sensor and the interface circuitry on the same chip in order to achieve the needed miniaturization for portable sensor systems. In biological applications other challenges concern the engineering of fluidic channels and their wetting of the resonator in a practical way; the resonator operation in fluids, where the damping could be very high, is a difficult problem to solve for the future.

APPENDIX A. Run-Card for a Typical "Thin"-Film SOI Wafer (1.5μm)

Step	Process	Details
1	SOI start wafer	Device layer: 1.5μm, n^+; BOX: 1μm
2	RCA	
3	First Oxide	500nm WetOx
4	Resist coating	Rite track 1, AZ92xx, 2μm
5	First mask	MA150, 10.5sec
6	Development	Rite track 2
7	Optical microscope	Inspection
8	Descum	Oxford Z2, 5min
9	SEM	Inspection
10	Oxide etch	AMS200, SiO2_PR_1:1, 1min45sec
11	Remove resist	Remover Z2, standard
12	Plasma O2	Oxford Z2, 20min
13	SEM	Inspection
14	RCA	
15	PolySi Spacer	100nm, LPCVD PolySi
16	Second Oxide	1.5μm LPCVD TEOS
17	CMP	Slurry 30N50, head:30rpm, platen:35rpm, back press: 0.02psi, working press:1.04psi, time:1min45sec
18	2nd oxide back-etch	BHF, 50sec
19	SEM	Inspection
20	Resist coating	Rite track 1, AZ92xx, 2μm
21	Second mask	MA150, 10sec
22	Development	Rite track 2
23	Optical microscope	Inspection
24	Oxide etch	AMS200, SiO2_PR_5:1, 2min
25	Remove resist	Remover Z2, standard
26	Plasma O2	Oxford Z2, 20min
27	SEM	Inspection
28	PolySi and Si etch	AMS200, SOI_SHARP, 3min40sec
29	FIB	Inspection
30	Polymer residue removal	Piranha-etch, standard
31	Native oxide removal	BHF, 30sec
32	Remove hard mask	BHF, 2min
33	SEM	Inspection
34	Resist coating	Rite track 1, AZ92xx, 2μm
35	Third mask	MA150, 10sec

36	Development	Rite track 2
37	Optical microscope	Inspection
38	PolySi etch	STS, Sub_Si, 30sec
39	Plasma O2	Oxford Z2, 20min
40	Remove resist	Remover Z2, standard
41	Plasma O2	Oxford Z2, 20min
42	SEM	Inspection
43	TSM metallization (at IMEC)	50nm TaN sputtered, 150nm Cu sputtered, 3μm Cu plated, 300nm Au plated
44	Structure release	BHF, 40min
45	Drying	Critical point drying
46	SEM	Inspection

APPENDIX B. Run-Card for a Typical "Thick"-Film SOI Wafer (6.25μm)

Step	Process	Details
1	SOI start wafer	Device layer: 6.25μm, p^+, {100}; BOX: 3μm
2	RCA	
3	First Oxide	1μm WetOx
4	Resist coating	Rite track 1, AZ92xx, 2μm
5	First mask	MA150, 11sec
6	Development	Rite track 2
7	Optical microscope	Inspection
8	Descum	Oxford Z2, 5min
9	SEM	Inspection
10	Oxide etch	AMS200, SiO2_PR_5:1, 4min20sec
11	Remove resist	Remover Z2, standard
12	Plasma O2	Oxford Z2, 20min
13	SEM	Inspection
14	RCA	
15	PolySi Spacer	100nm, LPCVD PolySi
16	Second Oxide	1.5μm LPCVD TEOS
17	CMP	Slurry 30N50, head:30rpm, platen:35rpm, back press: 0.02psi, working press:1.04psi, time:2min+1min
18	2nd oxide back-etch	BHF, 1min
19	SEM	Inspection
20	Resist coating	Rite track 1, AZ92xx, 2μm
21	Second mask	MA150, 10.5sec
22	Development	Rite track 2
23	Optical microscope	Inspection
24	Oxide etch	AMS200, SiO2_PR_5:1, 4min30sec
25	Remove resist	Remover Z2, standard
26	Plasma O2	Oxford Z2, 20min
27	SEM	Inspection
28	PolySi and Si etch	AMS200, SOI_SHARP, 18min
29	FIB	Inspection
30	Polymer residue removal	Piranha-etch, standard
31	Native oxide removal	BHF, 30sec
32	Skirting opening	Alcatel601E, Si_ISOSlow, 15sec
33	Remove hard mask	BHF, 8min
34	SEM	Inspection

35	Resist coating	EVG, AZ9260, 8μm
36	Third mask	MA6, 45sec
37	Development	EVG
38	Optical microscope	Inspection
39	PolySi etch	STS, Sub_Si, 30sec
40	Plasma O2	Oxford Z2, 20min
41	Remove resist	Remover Z2, standard
42	Plasma O2	Oxford Z2, 20min
43	SEM	Inspection
44	Aluminum deposition	1μm evaporated Al, EVA600
45	Resist coating	EVG, AZ9260, 8μm
46	Fourth mask	MA6, 60sec
47	Development	EVG
48	Optical microscope	Inspection
49	Al wet etch	ANP, 26min
50	Remove resist	Remover Z2, standard
51	SEM	Inspection
52	Structure release	Silox-etch, 150min
53	Drying	Critical point drying or air drying, by replacing water with IPA and then with acetone
54	SEM	Inspection

APPENDIX C. Curriculum Vitae

PERSONAL DETAILS

Name	Nicoleta-Diana Ciressan
Date and place of birth	August the 13th, Bucharest, Romania
E-mail address	diana.ciressan@a3.epfl.ch

EDUCATION

May 2004 at present	PhD student Thesis: *Nanogap MEM Resonators on SOI* Advisors: Prof. Adrian M. Ionescu and Dr. Marco Mazza Ecole Polytechnique Fédérale de Lausanne (EPFL) Lausanne, Switzerland
Sept. 1998 – Jun. 2003	Bachelor and Masters Degree in Microelectronics University "Politehnica" of Bucharest Bucharest, Romania
Jun. 1998	Baccalaureate, Romania

RESEARCH EXPERIENCE

May 2004 at present	Research assistant at the Nanoelectronic Devices Laboratory (NANOLAB), Ecole Polytechnique Fédérale de Lausanne. The research focused mainly on development of silicon RF microelectromechanical (MEM) resonators for time-keeping and frequency reference applications. Involvement in scientific and administrative activities in the European project NanoTIMER (IST- 2003-507914): Nano-technology in mechanical-electrical resonators. Partners: NXP Semiconductors, EADS, IMEC, University of Cambridge

TEACHING EXPERIENCE

May 2004 at present	Teaching assistant at the Nanoelectronic Devices Laboratory (NANOLAB), Ecole Polytechnique Fédérale de Lausanne. Teaching activities include the supervision of labs, exercises and projects for undergraduate students in electronics and diploma projects for master students.

Publications

JOURNAL PAPERS

[1] N.-D. Badila-Ciressan, C. Hibert, M. Mazza, and A.M. Ionescu, “Fabrication of Silicon-On-Insulator MEM Resonators with Deep Sub-Micron Transduction Gaps”, Journal of Microsystem Technologies, volume 13, issue 11, 2007, pp. 1489 - 1493

[2] D. Grogg, N.D. Badila-Ciressan, A.M. Ionescu, "Focused ion beam based fabrication of micro-electro-mechanical resonators", Journal of Microsystem Technologies, volume 14, no. 7, 2008, pp. 1049-1053

[3] N.-D. Badila-Ciressan, M. Mazza, D. Grogg and A.M. Ionescu, “Nano-gap micro-electro-mechanical bulk lateral resonators with high quality factors and low motional resistances on thin silicon-on-insulator”, Solid-State Electronics, volume 52, issue 9, 2008, pp. 1394-1400

[4] D. Grogg, H.C. Tekin, N.D. Badila-Ciressan, D. Tsamados, M. Mazza, A.M. Ionescu, "Bulk Lateral MEM Resonator on Thin SOI With High-Q Factor", Journal of Microelectromechanical Systems, Accepted for future publication, 2009

CONFERENCE PAPERS

[5] N.-D. Badila, S. Ecoffey, D. Bouvet, and A.M. Ionescu, "A Study of Fabrication Techniques for Sub-10nm Thin Undulated Polysilicon Films", International Semiconductor Conference (CAS ‘03), volume 1, 2003, pp. 95-98

[6] M. Mazza, N.-D. Badila, and A.M. Ionescu, “25.5 Mhz Silicon-on-insulator Bulk-mode Resonators: Design, Fabrication and Electrical Characterization”, MEMSWAVE Symposium 2005, 2005

[7] N.-D. Badila, C. Hibert, M. Mazza, and A.M. Ionescu, “Fabrication of Silicon-On-Insulator MEM Resonators with Deep Sub-Micron Transduction Gaps”, Symposium on Design, Test, Integration and Packaging of MEMS/MOEMS (DTIP ’06), 2006, pp. 185-188

[8] D. Grogg, D. Tsamados, N.-D. Badila, and A. M. Ionescu, “Integration of MOSFET Transistors in MEMS Resonators for Improved Output Detection”, International Solid-State Sensors, Actuators and Microsystems Conference (Transducers ‘07), 2007, pp. 1709-1712

[9] N.D. Badila-Ciressan, M. Mazza, D. Grogg, and A.M. Ionescu, "Fragmented membrane MEM bulk lateral resonators with nano-gaps on 1.5um SOI", The 37th European Solid-State Devices Research Conference (ESSDERC ’07), 2007, pp. 430-433

[10] D. Grogg, N.D. Badila-Ciressan, D. Tsamados, N. Abelé, and A.M. Ionescu, “Fabrication of MEM resonators in thin SOI”, Symposium on Design, Test, Integration and Packaging of MEMS/MOEMS (DTIP ‘07), 2007, pp. 310-313

[11] D. Grogg, H.C. Tekin, N.D. Badila-Ciressan, M. Mazza, D. Tsamados, and A.M. Ionescu, "Laterally vibrating-body double gate MOSFET with improved signal detection", Device Research Conference (DRC ’08), 2008, pp. 155-156

[12] D. Grogg, H.C. Tekin, N.D. Badila-Ciressan, D. Tsamados, M. Mazza, and A.M. Ionescu, "Nano-Gap High Quality Factor Thin Film SOI MEM Resonators", NANOTEC 2008, volume 3, 2008, pp. 940-943

WORKSHOP PRESENTATIONS

[13] M. Mazza, N.-D. Badila, J. Perruisseau, A.M. Ionescu and A. Skrivervik, "Nano-gap MEMS resonators and adapted oscillator design", NanoTIMER Workshop on Micro-Electro-Mechanical Resonators: From Technology to Applications, Feb. 2nd 2006, Lausanne, Switzerland